Politecnico di Torino

Politecnico di Torino

Mechanical and Aerospace Engineering Department

Master's Degree Thesis in Mechanical Engineering

A.Y. 2022/2023

Dynamic Modelling of a Compact EHSA for the Stabilization and Command Augmentation System of Rotary Wing Aircraft

Supervisors:

Prof. Massimo Sorli

Asst. Prof. Andrea De Martin

Ext. Supervisors:

Prof. Giovanni Jacazio

Candidate:

Luciano Alberto Lo Presti

Riservo questo spazio del mio elaborato per un pensiero a tutti coloro che mi hanno supportato in questo impegnativo percorso di studi e di vita.

In primis, un ringraziamento speciale al prof. De Martin, per la sua immensa pazienza e disponibilità con cui mi ha seguito durante tutte le fasi di sviluppo della tesi.

Ringrazio infinitamente mia Mamma e mio Papà per avermi sostenuto e permesso di ottenere questo risultato.

Grazie a mio Fratello ed a tutti i miei Familiari.

Grazie di cuore alla mia Fidanzata per avermi supportato e sopportato in questi anni nel mio cammino.

Un ringraziamento va anche a tutti i Colleghi e gli Amici per i loro piccoli e grandi contributi.

Ci tengo a dedicare questo lavoro ai miei Nonni che hanno sempre creduto in me facendomi sentire all'altezza delle più alte aspettative, sono certo che sarebbero tutti molto orgogliosi ed emozionati nel vedere il loro nipote raggiungere questo traguardo e diventare "Ingegnere".

ABSTRACT

Rotary-wing aircrafts, under critical operating conditions, generally use the ***Stability Control Augmentation Systems*** (*SCAS*) to improve stability and manoeuvrability. While fixed-wing aircraft commonly use fly-by-wire systems as the basis for primary flight control, rotary-wing aircraft still primarily rely on hydraulic servosystems to control collective and cyclic pitch of the main rotor and the collective of the tail rotor. As technology has improved, the use of fly-by-wire systems in rotary-wing aircraft has spread to provide more efficient and safer aircraft that require less effort from the pilot to complete their missions. Briefly, the *SCAS* system is a circuit parallel to the hydraulic-mechanical system that provides the pilot assistance in manoeuvring the machine through electrical signals. This system acts via a limited authority actuator on the aircraft's main control linkage, imitating the pilot-induced command into the movement of the helicopter's main flight actuator. *SCAS* are systems that, in the majority of applications, use an electro-hydraulic servo actuator position controlled *EHSA*. The main component of this system is the servo-valve, that functions as an interface between an electrical (or mechanical) input signal and the hydraulic power represented by the flow and pressure output. In this thesis, a dynamic model is developed to simulate, in a *MATLAB - Simulink* environment, the behaviour of the electro-hydraulic servomechanism used in *SCAS*. Hence, the system will test only the use of the first stage for servo valve for reasons of compactness, weight, and reduced wear. The purpose of this discussion is to produce an accurate model of the first stage of a jet-pipe servo-valve, and after the aims is to dimensioning and model a compact actuator. Finally, all the tests that were performed necessary to demonstrate the validity, and therefore the usefulness, of the model created will be shown and properly commented on.

Keywords: SCAS, Jet-pipe, First stage, Servo-valve, EHSA, Simulink

INDEX

LIST OF ACRONYMS AND SYMBOLS

Acronyms:

AFCS	*Automatic Flight Control Systems*
EHSA	*Electro-Hydraulic Servo Actuator*
EHSV	*Electro-Hydraulic Servo Valve*
LVDTs	*Linear Variable Differential Transformers*
MRA	*Main Rotor Actuator*
NOE	*Nap-of-the-earth (very low-altitude flight)*
PID	*Proportional–Integral–Derivative Controller*
SAR	*Search and Rescue*
SAS	*Stability Augmentations Systems*
SCAS	*Stabilization and Command Augmentation System*
VTOL	*Vertical Take-Off and Landing*

Common symbols:

$P_s\ [Pa]$	Supply Pressure
$P_r\ [Pa]$	Return Pressure
$\rho\ [\frac{Kg}{m^3}]$	Density of fluid
$\mu\ [Pa \cdot s]$	Dynamic viscosity
Re	Reynolds number

1. INTRODUCTION

This thesis work will focus on Dynamic modelling of a compact EHSA for the Stabilisation and Command Augmentation System of rotary wing aircraft. Therefore, this chapter will present some fundamental concepts in order to provide the reader to understand the work properly. Some fundamental aspects of the helicopter are highlighted, such as its architecture, the main hydraulic system, and the main flight controls, and how they allow the variation of flight to control surfaces. In this context, the Stabilization and Command Augmentation System (*SCAS*), which is the main object of this study, is introduced. Subsequently, overview of the servosystem and servo valve are provided, with a focus on those components that are the main arguments of this work like EHSA and jet-pipe valve. Finally, objectives and aims will be presented, which will be deeply explored in the following chapters.

1.1 Introduction to the Flight Control System for Rotary-Wing Aircraft

With the term 'rotary-wing aircraft' generally refer to helicopters, since helicopters derive their thrust force from the rotation of the rotor blades around the shaft [1]. The conventional helicopter rotor consists of a central hub with two or more identical, equally spaced blades attached. By rotating around a vertical axis, the rotor blades create relative motion between the wings and air, resulting in aerodynamic forces that provide lift and thrust to the aircraft (fig. 1).

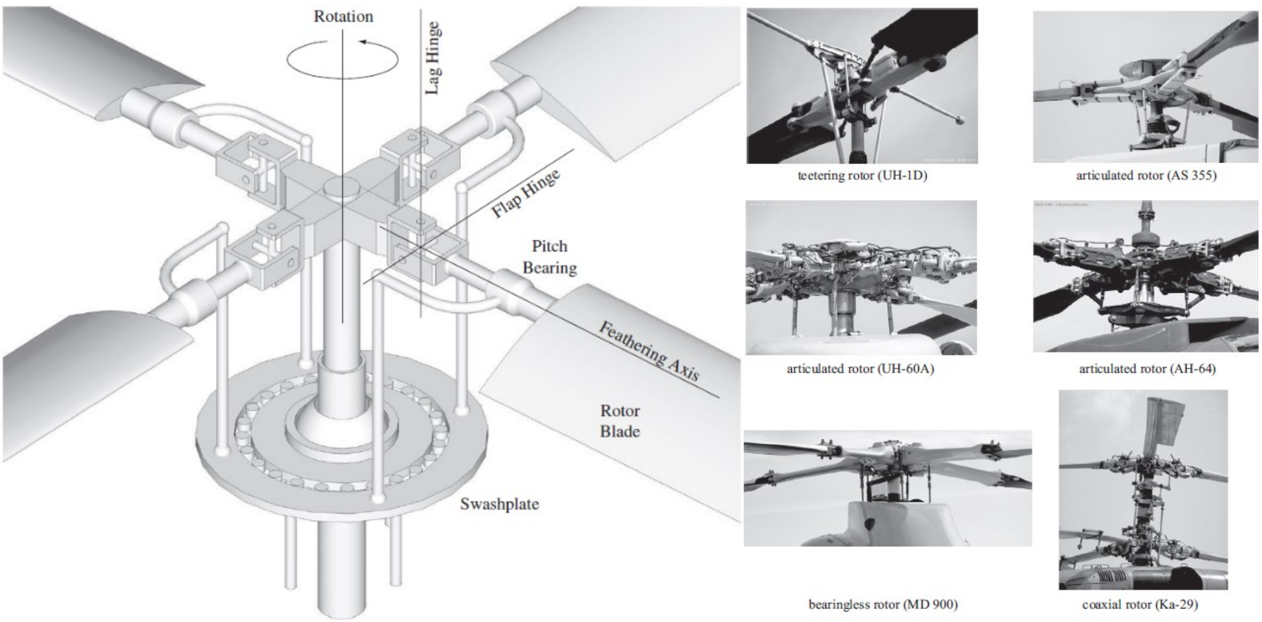

Figure 1:On the left side schematic of an articulated rotor hub and root, on the right example of rotor hub configurations [2]

To balance the torque reaction generated by the main rotor, different rotor configurations are used. The most common configuration is a single main rotor and tail rotor, where the main rotor provides lift, propulsion, and roll/pitch control, while the smaller tail rotor provides torque balance and yaw control. It is possible to have a variety of other configurations (fig. 2), included equal-sized contra-rotating rotors that cancel out their respective reaction torques, such as in tandem-rotor or coaxial rotor configurations.

Figure 2:Different types of rotorcraft configurations [2]

The flight control system for rotary-wing aircraft is an essential component that enables pilots to control and maneuver the aircraft. Helicopter control involves producing moments and forces to achieve equilibrium and change the speed of the aircraft, its position and orientation. Control is primarily achieved by producing moments around the pitch, roll, and yaw axes, with the helicopter having additional control over vertical force corresponding to its VTOL capability. Trajectory control in forward flight is achieved through direct control over moments, but in hover and low speed, direct control over forces is recommended. Rotor speed governor helps to manage power, and compensating control inputs on other axes are necessary when producing a particular moment. Controlling lateral and longitudinal velocities in hover requires pitch and roll moments, which is a difficult task due to the coupling of forces and moments produced by helicopter controls. [2] In practice, these described movements are achieved by acting on the primary flight controls [1]:

- **Collective Pitch Control:** it is used to change the pitch angle of all main rotor blades simultaneously. The amount of movement in the collective lever affects the amount of change in blade pitch, and this is done by mechanical linkages. If the pitch angle on the blades change also results in a change of the angle of incidence on each blade, it affects the speed or revolutions per minute (rpm) of the main rotor. The *throttle control* or *governor/correlator* automatically adjusts engine power to compensate for changes in aerodynamic resistance and maintain a constant rotor speed, which is essential in helicopter operations. Finally, an adjustable friction lever control helps to prevent inadvertent collective pitch movement.
- **Cyclic Pitch Control:** It is often raised from the cockpit floor, giving the pilot complete control to steer the helicopter in any direction. The cyclic pitch control is designed to adjust the tilt of the tip-path plane towards the intended horizontal direction, which in turn directs the rotor disk thrust and allows the pilot to manage the direction of the helicopter of travel. The mechanical

linkages for the cyclic control rods are rigged to decrease and then increase the pitch angle of the rotor blade. This causes the rotor disk to tilt in the desired flight direction.

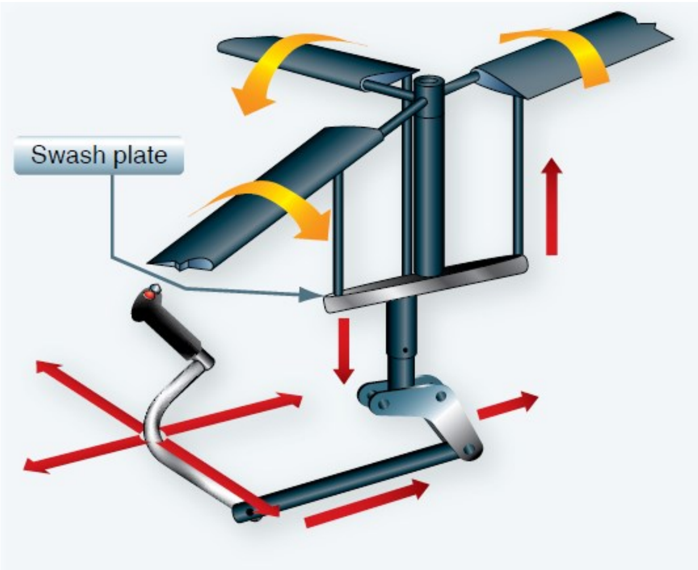

Figure 3: Cyclic controls changing the pitch of the rotor blades [1]

- **Antitorque Pedals:** The antitorque pedals, situated on the cabin floor, control the pitch of the tail rotor blades or other antitorque systems to counteract the rotation of the helicopter fuselage in the opposite direction of the main rotor blades, as per Newton's Third Law. Most helicopter designs include an antitorque rotor or tail rotor to account for this torque. The pitch angle of the tail rotor blades is adjusted using the antitorque pedals, which allows the helicopter to be placed in longitudinal trim during forward flight and enables the pilot to turn the helicopter 360° while hovering. To modify the pitch angle of the tail rotor blades, the antitorque pedals are coupled to the tail rotor gearbox's pitch adjustment mechanism.

Generally, each flight control is connected to a hydraulic system that consists of electro-hydraulic actuators, also called servos or MRA (*Main Actuator System*). In addition to the actuators there is a pump which is usually driven by the main rotor transmission and a reservoir to store the hydraulic fluid (fig. 4).

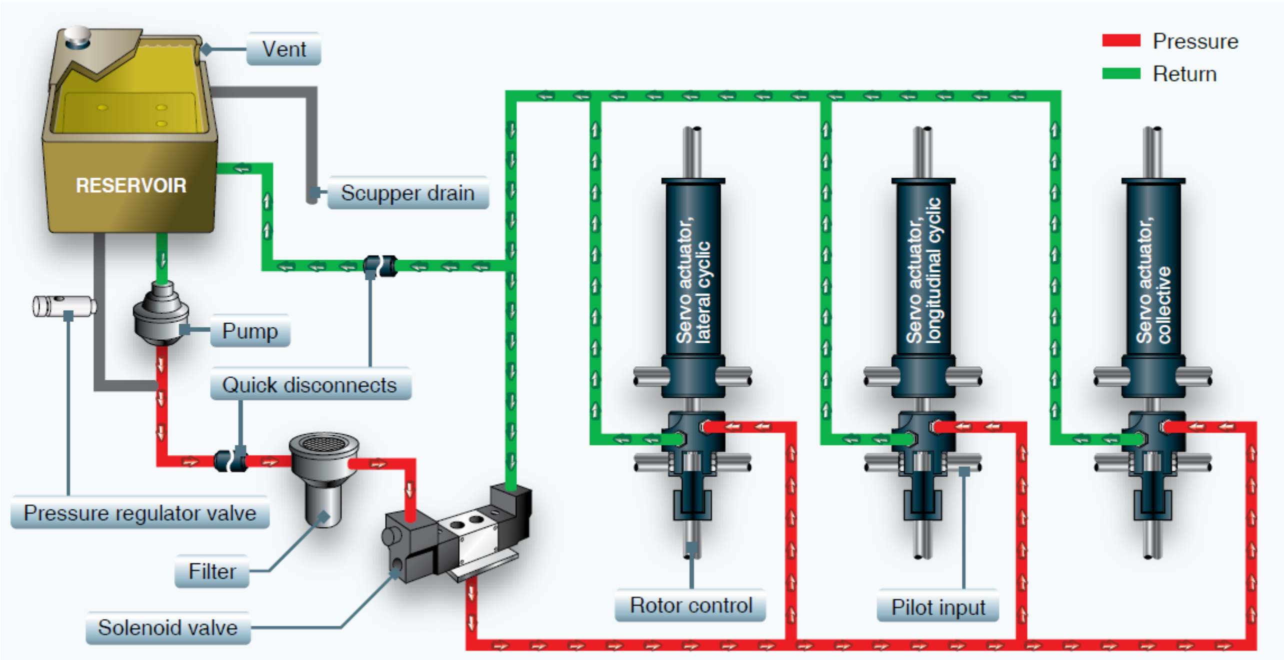

Figure 4: A typical hydraulic system for helicopters in the light to medium range [1]

The servos provide an assisting force to move the respective flight control, making it easier for the pilot to control the helicopter. The pilot can still operate the helicopter if the hydraulic system fails, but the control forces will be very strong. Some helicopters have two or more independent hydraulic systems, while others use hydraulic accumulators to store hydraulic pressure for emergency situations, allowing to an uninterrupted control for a short period adequate for an emergency landing. Other applications include a failsafe system ensuring that the pilot can still control the helicopter with the hydraulic fluid in the actuators, even if electrical power is lost in flight. [1][2]

The actuator system of the main rotor is composed by a control rod connected to a pair of hydraulic actuators arranged in tandem. This configuration allows a larger effective area of the actuators, which increases the generated force, while keeping small the overall size of the system. Both the left and right sides of the system function in the same manner contain identical components. The tandem design of the configuration also improves the safety and cost-effectiveness of overall system by ensuring the redundancy of its components. The two hydraulic cylinders of the control system are operated by servo valves, which are steering in position by the control road allowing the pilot to input commands. The position of the valves and actuators depends on several forces, including the pilot's input, output force acting as feedback, and two smaller actuators called SCAS (*Stabilization and Command Augmentation System*) actuators. Additionally, each SCAS actuator is controlled by an EHSA (*Electro-Hydraulic Servo Actuators*) that mimics the pilot's input signal. In the case of a SCAS system failure, the pilot can manually shut down the system's actuators by closing a normally closed shut-off valve, which cuts off the fluid supply to the cylinders. This eventuality results in reduced overall flight stability, which can be critical in certain operations. Typically, four LVDTs (*Linear Variable Differential Transformers*), two each for the main actuator and SCAS actuators, are installed, and their signals are primarily used for the control system [4]. A system architecture scheme is provided in the figure below (fig. 5).

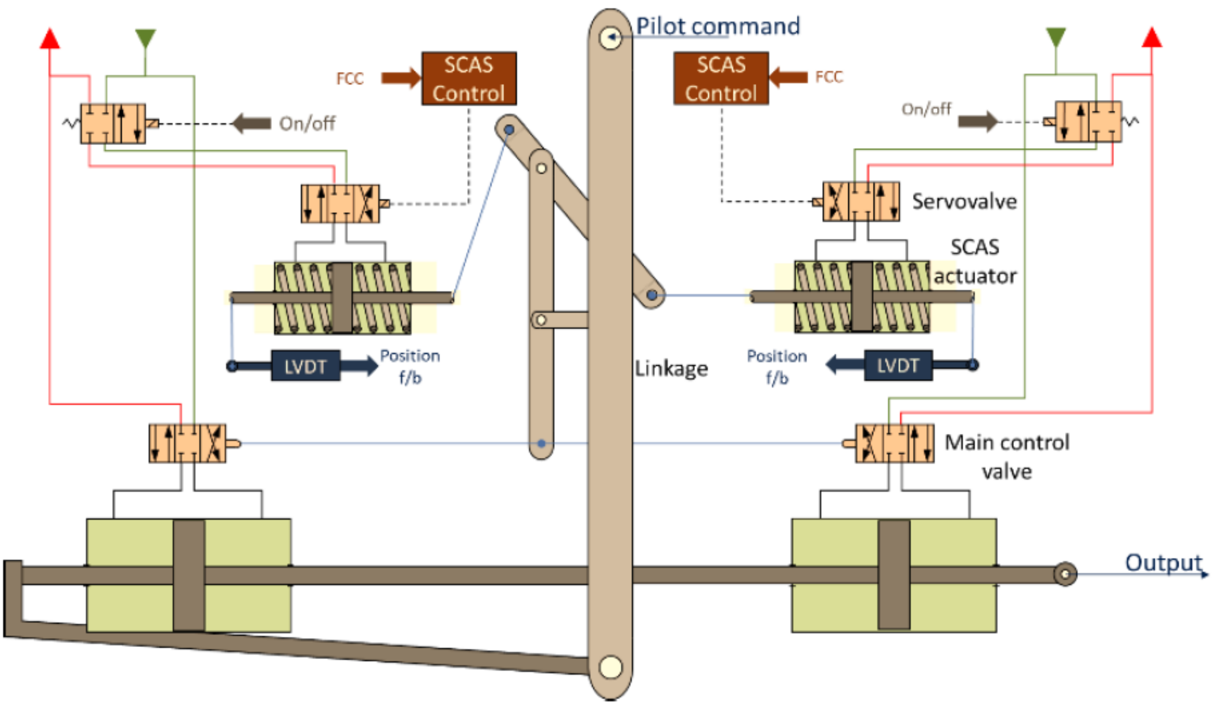

Figure 5: MRA hydraulic control scheme [3]

1.2 Stabilization and Command Augmentation System – SCAS

Helicopter controls produce considerable coupling of the forces and moments, thus every control application that seeks to achieve a specific moment also needs to make some compensatory control inputs on the other axes. A Stabilization Augmentation System (*SAS*) is incorporated into several helicopters to aid flight, in addition, without an SAS system, the helicopter is neither dynamically nor statically stable, especially when hovering. Originally designed to reduce pilot fatigue and workload, SAS systems, have been increasingly technologically advanced. Nowadays, these systems have become indispensable when the pilot has to perform complex manoeuvres especially in military operations, such as sling loading and search and rescue (*SAR*) or *NOE* tasks that are very low-altitude flight course used by military aircraft to avoid enemy detection and attack in a high-threat environment. Generally, Stabilization Augmentation System use EHSAs, where control signals for these servos are provided by a computer that monitors external environmental inputs like wind and turbulence. The SAS system can be so complex that it provides three-axis stability. In other words, computer-based inputs modify attitude, power, and trim of the aircraft for more stable flight. Once activated by the pilot, these systems use a variety of sensors, including stabilized gyroscopes and electromechanical actuators, to instantaneously input all flight controls without the need for a pilot intervention. In addition, the pilot can override or disconnect the control system at any time. [2][1]

SCAS acronym for *Stabilization and Command Augmentation System* can be considered among the most widely used Automatic Flight Control Systems (*AFCS*), it acts on the cyclic command by improving hovering and aircraft stability and reducing external disturbances [5]. Reduced schematic image of SCAS system architecture can be seen in fig.6.

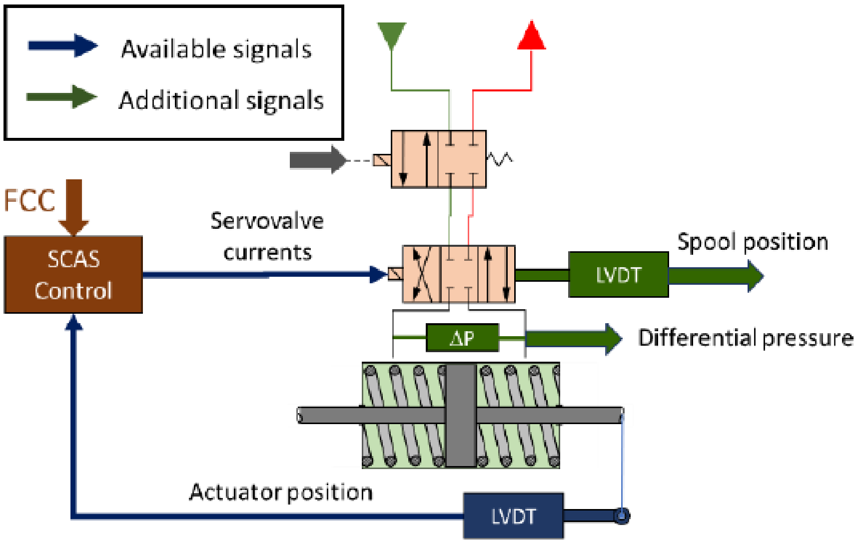

Figure 6: Architecture of a single SCAS system [3]

SCAS actuators have small size and a short stroke; moreover, they have stringent safety constraints, which is why they have limited control over MRA movements [7]. Usually, SCAS actuators are equipped with two re-centering springs: this component is critical to the safety of the system, as it allows the actuator to maintain a neutral position in case of failure and deactivation. Usually, a functionality scheme like the one presented in fig. 7 is adopted for SCAS vehicle integration. The internal state of the aircraft is accurately evaluated with the use of a Kalman filter that receives input information from the INS-Inertial Navigation System's velocity sensors, a gyroscope, and an accelerometer [6]. In principle, this sensor fusion approach provides a robust and an accurate estimate of the state of the helicopter; the resulting filtered signal is then added to the signals provided by the other gyroscopes and the decoupling signal from the other axis to generate the input to the system servos that can manage the speed of helicopter to the system servo that will control the position of the SCAS actuators. [5][4]

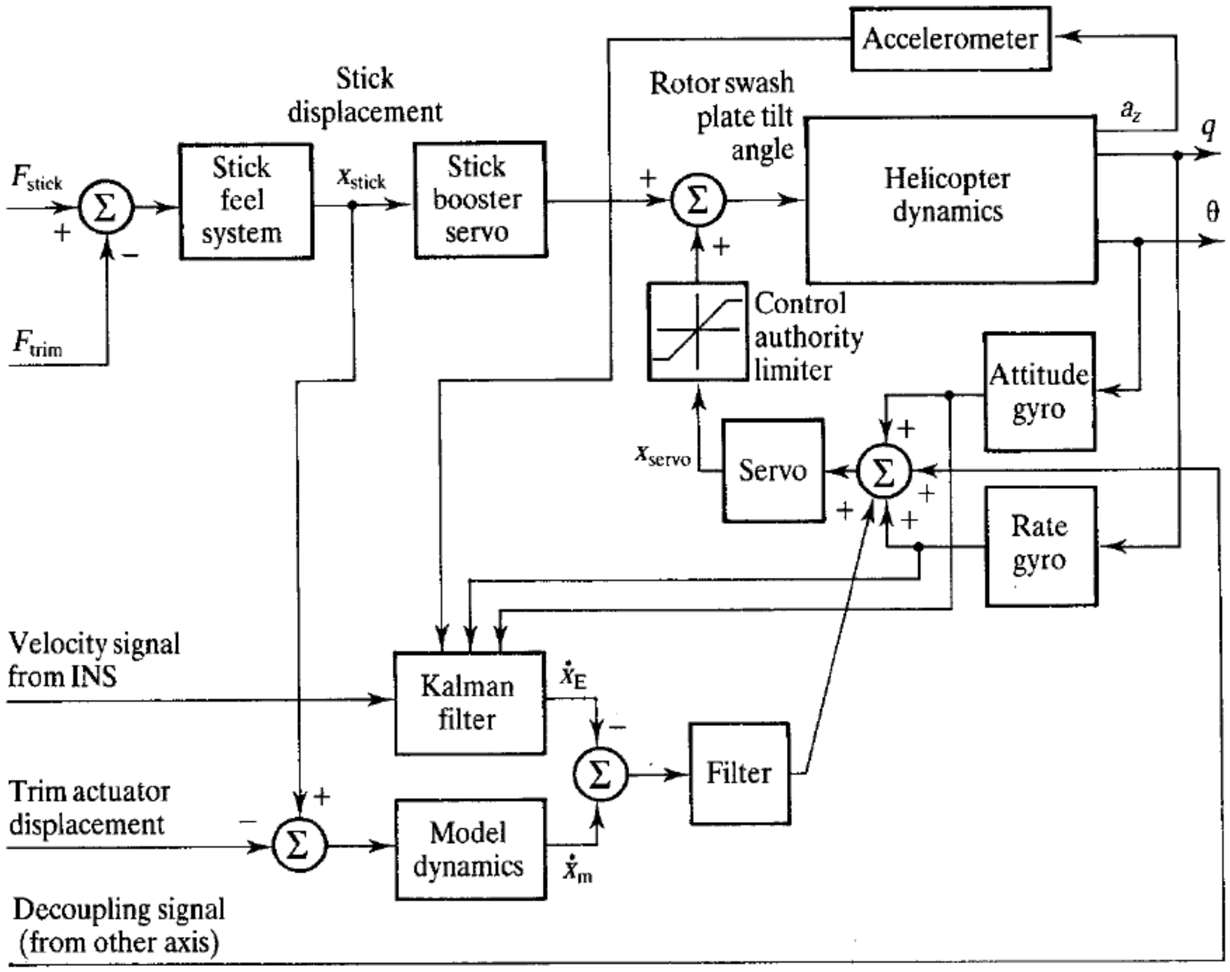

Figure 7: SCAS system vehicle integrated layout [5]

In conclusion, the use of these systems, such as the SCAS that has just been described, naturally increases the cost and the complexity of the helicopter but from the other side increase considerably the manoeuvrability and control of the aircraft.

1.3 Overview of Servosystems

Servosystems are systems that have the ability to regulate a flow of power, coming from a source that can be hydraulic, electrical, or pneumatic, obtaining as output a specific result that can be translated in a time law for a physical quantity. Servosystems can be of various types, many examples can be given, the most common ones are those that regulate position, speed, torque, pressure among others. Choosing the correct mechanism for a specific application is based on a variety of parameters such as: customer performance, cost, size and weight, duty cycle, environment (vibration, shock, temperature, etc.).

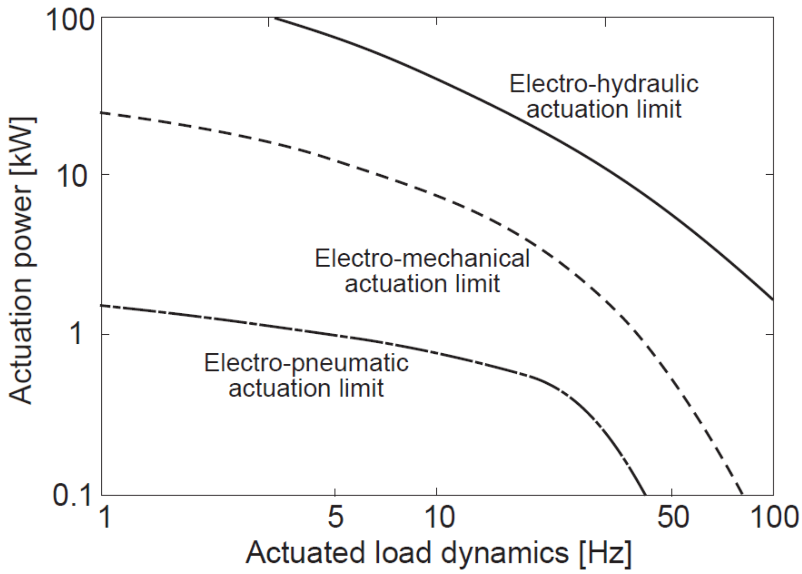

Figure 8: Typical performance characteristics for different types of servo actuators [9]

A servosystem is defined as a mechatronic system, which is composed by an actuating part, a regulating part, and sensors [8]. Generally, the purpose of such systems is to copy a set signal received as input and make the output as close as possible to the desired target by taking into account, and compensating for, an error that is generated between set and feedback signals. Servosystems can be structured as open-loop or closed-loop. In open-loop configuration there is no regulation and disturbances go to change the output without the possibility for it to act on process regulation:

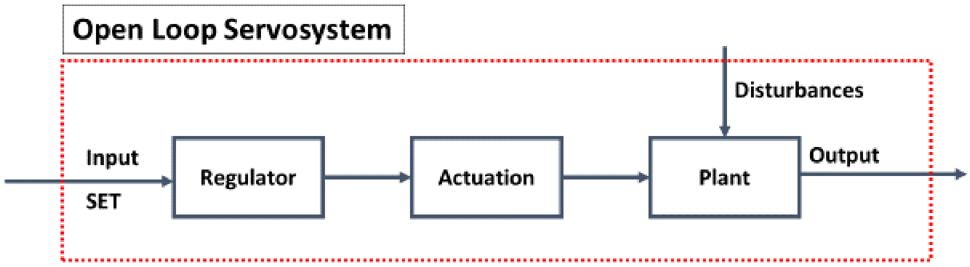

Otherwise, in the closed-loop configuration the output variable is adjusted, there is a SET - FEEDBACK = ERROR relationship that compensates for the error by a control law (generally, a PID controller is used). This configuration, compared with the open-loop case, leads to a faster time response. It is more precise, especially steady-state response, with a reduced sensitivity to disturbances.

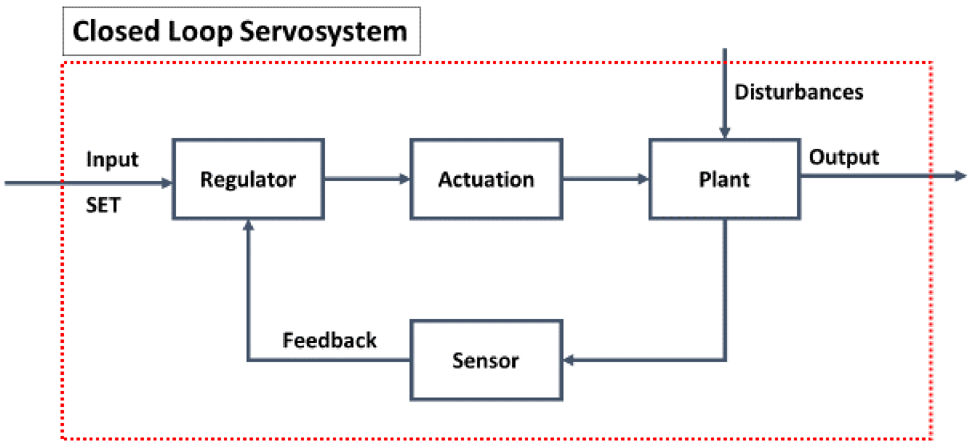

Below, as already seen in the section "Flight Control System for Rotary-Wing Aircraft," the description will focus on the position-controlled electro-hydraulic servo actuators, which will be the subject of this thesis since the SCAS system bases its logic on such a system.

1.3.1 Electro-Hydraulic Servo Actuator – EHSA

Flight controls in rotary-wing aircraft need dynamic requirements for readiness and accuracy in the presence of even high loads to which they are subjected, along with servo reliability. These factors have led to the almost exclusive use of hydraulic systems because it provides fast response, high force, and short stroke characteristics. Specifically, when SCAS is described, it refers to a system that uses an electro-hydraulic servo actuator position controlled. This type of application uses a *fly-by-wire* architecture. The actuator is hydraulically powered while the control signal is processed by Flight Control Computer as the difference between SET (sent by the pilot or auxiliary systems) and feedback (obtained from LVDT transducer applied on the cylinder). The signal thus obtained is sent to the servo valve, which appropriately feeds the chambers of the hydraulic cylinder fig (9).[8]

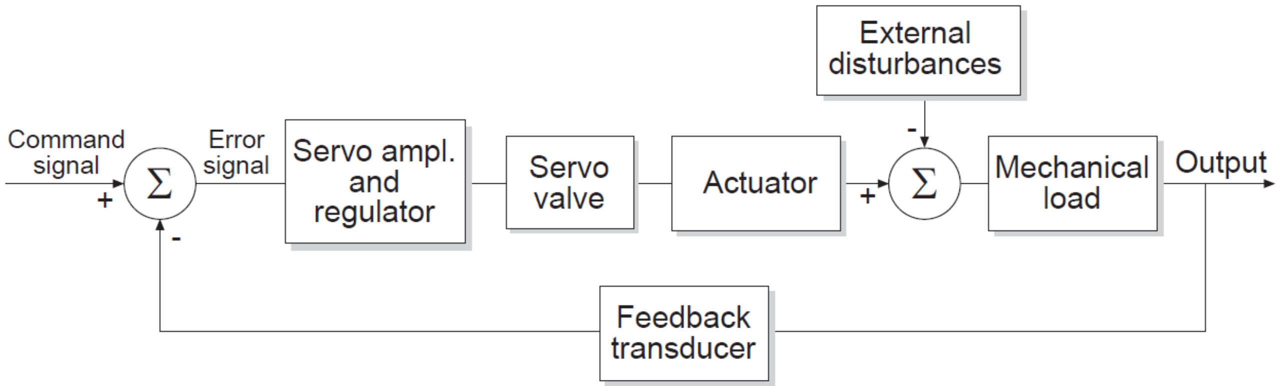

Figure 9: Components in an electro-hydraulic servomechanism [9]

The operation of a position-controlled electro-hydraulic system will now be described in detail, as the subject of this thesis. In such system, the output position is transformed into a voltage signal by the LVDT transducer present in the feedback loop so that the comparison can be made with the SET voltage signal representing the imposed position command. The error signal is processed by the controller and then by the amplifier so as to determine the reference voltage at the end of the servo valve windings. The servo valve provides a flow rate to the actuator proportional to the imposed command, thus the signal sent to the external load is born with the objective of reducing the error between system input and output in the shortest possible time. The probable presence of an external disturbance, which consists of a force signal for a position control, results in the birth of a non-zero error even in the face of an unchanged (or null) command signal, and it is the task of the servo system: to react in such a way as to return the system to position in the shortest possible time. [9]

1.4 Overview of Servo Valves

The main element of the hydraulic servo system is the servo valve, and it is important to understand its characteristics. A servo valve is a component that works as an interface between an electrical (or mechanical) input signal and the hydraulic power represented by the flow and pressure output. Developed by military applications, the earliest applications include Lockheed P-80, they have successively spread to various fields [8]. Unlike other types of control valves, servo valves are distinguished by their small size and low weight, lower power consumption because the current consumed serves only as a control signal and not as a power signal. Depending on the application, different types of servo valves can be used. Generally, each servo valve can be divided into two sections called *stages.* The *pilot stage* or *first stage,* is the part of the valve that converts the electrical control signal into a pressure signal that is manifested at the end of the next stage spool, this operation is performed by two components, a hydraulic amplifier, and a torque motor. Besides the first stage, a *second stage* or *main stage* is defined as the part of the valve that determines the flow rate of hydraulic fluid flow rates exchanged between the actuating device and the supply (supply pressure) or return (return pressure) lines. In addition, there is a feedback spring that connects the spool of the main stage and the moving element of the hydraulic amplifier, this spring allows the static equilibrium condition between the main and pilot stages to be achieved. A schematic of a two-stage servo valve is provided in the figure 10 visible below.

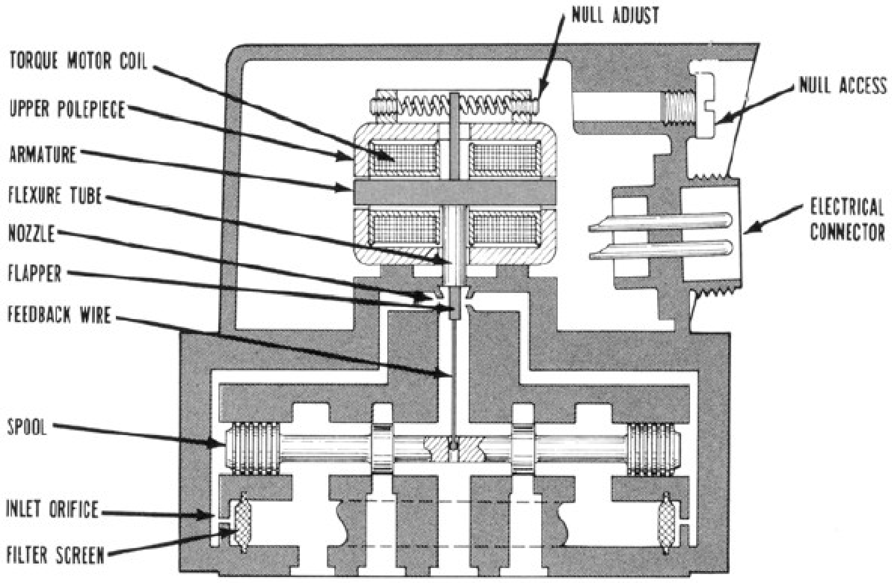

Figure 10: Two-stage servo valve

As already stated, there are various types of servo valves, the main ones being *flapper-nozzle* and *jet-pipe* devices, the latter which will be treated extensively later as it is a topic of this thesis. In the flapper-nozzle device the hydraulic part of the pilot stage consists of two nozzles symmetrical to a shutter which is integral with the axis of the torque motor. Electrical current in the torque motor coils causes either clockwise or counterclockwise torque on the armature. This torque displaces the flapper between the two nozzles. The differential nozzle flow moves the spool either the right or the left. The spool continues to move until the spring feedback torque counteracts the electromagnetic torque of the motor. At this point the armature/flapper is returned to centre, so the spool stops and remains displaced until the electric input changes to a new level (fig 11).

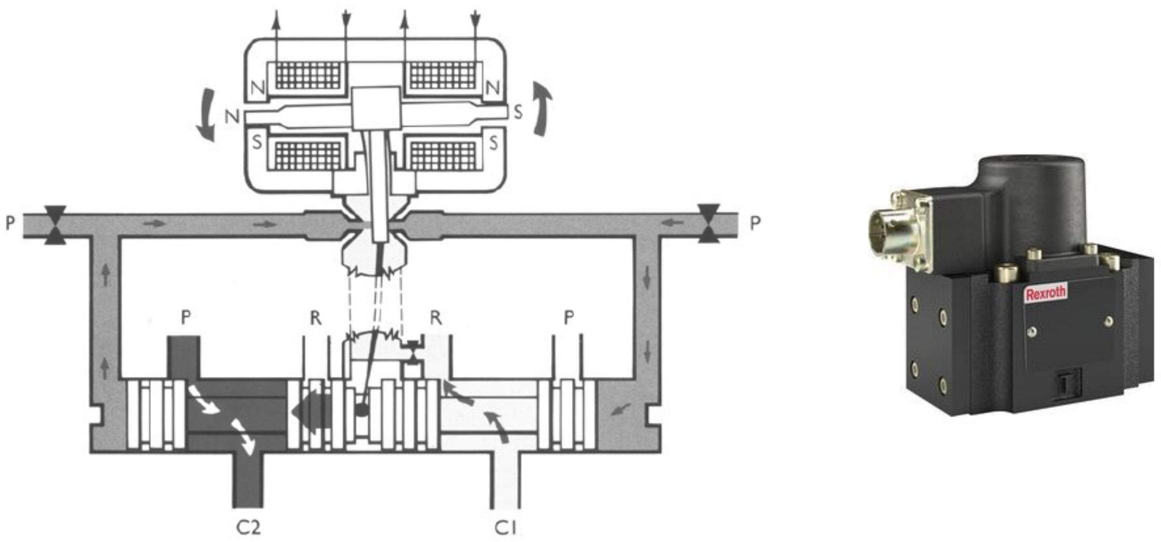

Figure 11: On the left flapper-nozzle valve responding to change in electrical input [9], on the right Bosch Rexroth Directional servo-valve 4WS2EM6 [10]

Moreover, the fluid from the supply is sent to the nozzle through calibrated resistances useful for decoupling the pressure of the nozzle's internal environment from the pressure of the supply line. It is exactly the presence of the calibrated resistances just described that is one of the major problems of flapper-nozzle servo valves, as they are sensitive to the presence of impurities and particulates in the hydraulic fluid. Therefore, they require the use of high-performance filters and clean fluid.

1.4.1 Jet Pipe Servo Valve

In jet-pipe servo valves, the moving element is a small pipe directly connected to the hydraulic supply, the device consists mainly of a torque motor, jet pipe and a receiver. In the zero condition, the jet leaving the pipe is equally distributed over the two receiver conduits connected to the spool of the second stage. A current through the coil of the torque motor displaces the jet pipe from neutral position. This shift, combined with the particular shape of the nozzle, directs the fluid jet towards one receiver rather than the other. The jet now produces a pressure difference at the ends of the spool, which in turn results in a displacement of the spool. The position control loop for the main stage spool is closed by the integrated electronics. A position transducer measures the position of the spool of the main stage. This signal is then sent back to the controller where it is compared with the SET command signal. The controller drives the pilot stage, and the displacement of the jet-pipe, until the error between the command and feedback signal is zero. Thus, the position of the main spool is proportional to the electrical command signal. The main limitation of this system is due to the presence of continuous leakage at the first stage, hence penalising its performance. [9][8]

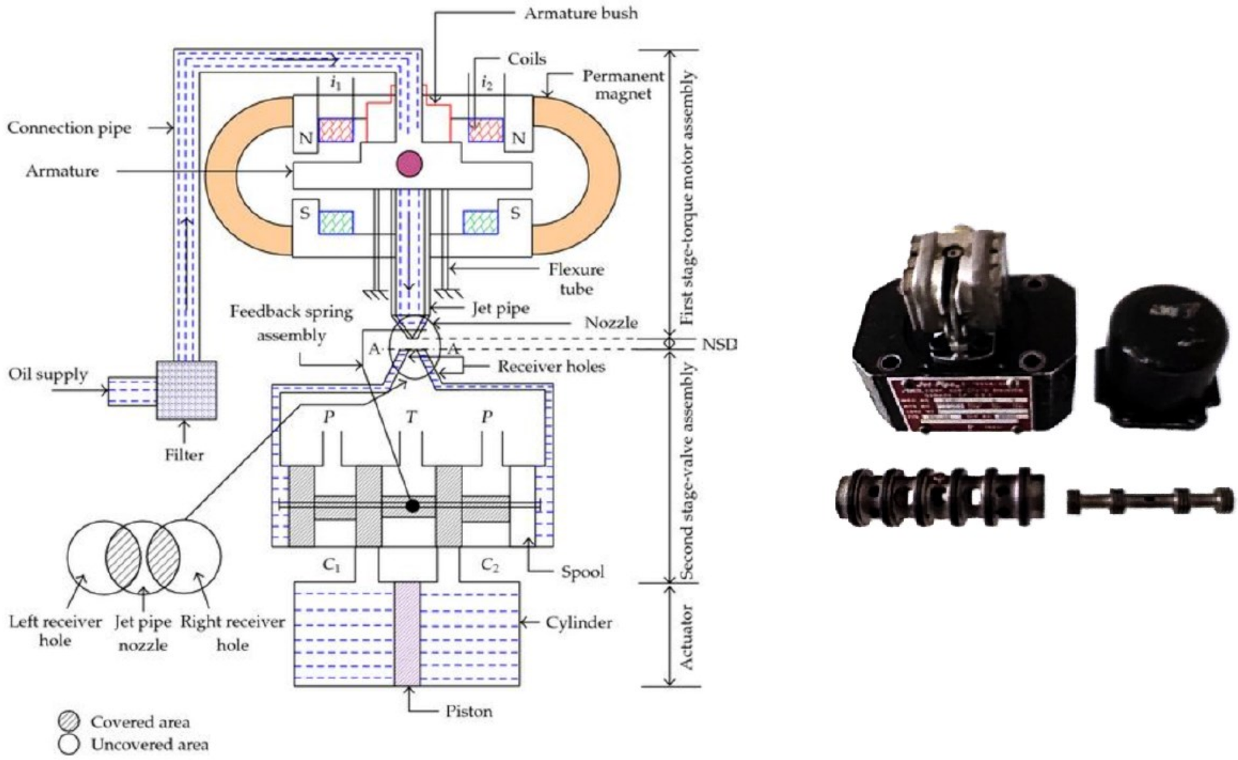

Figure 12: On the left schematic representation of the two stages jet pipe servo-valve [11], on the right jet-pipe components [8]

1.5 Study Motivation and Objectives

Field surveys on rotary-wing aircraft indicate that among servos, particularly servo valves, landed due to failures, almost all failures occurred in the second stage, or in connection components such as the feedback spring. In the helicopter field, as mentioned in the previous paragraphs, there is a need for SCAS systems. Due to their characteristics, helicopters are subject to very demanding vibration ranges for mechanical components, and this statement is especially true if we refer to SCAS systems introduced precisely to facilitate those operations such as combat *SAR* and *NOE* where the controls are put to the hardest test and mechanical stresses are significant. Therefore, it would make sense to have fewer mechanical components in relative contact with each other to reduce wear. Hence, an elimination of the second stage could bring benefits not only in terms of the aforementioned but also in terms of having more compact systems and thus a reduction in weight, a topic of relevant importance in the aeronautical industry. This thesis work therefore aims to model a compact EHSA for the SCAS of rotary wing aircraft. It will start with the accurate modelling of the first stage of a jet-pipe servo valve, and then go on to model and dimension a SCAS actuator. Once this has been done, it is intended to verify its performance. In addition, it must be said that there are limitations to using only the first stage for servo valves: the first is due to the fact that the pilot stage only uses very low flow rates to give the control signal to the main stage; this problem could be avoided in the system under consideration as SCAS actuators require very small flow rates. Secondly, in some applications, the single-stage concept can also lead to stability problems, this happens if the flow forces acting on the spool are close to the force produced by the torque motor. The flow forces are proportional to the flow rate and the square root of the valve pressure drop, which results in a limitation of hydraulic power. These problems should be investigated during the modelling work, and if possible, avoided by appropriate dimensioning.

2. MODEL DESCRIPTION

In this chapter, the model developed during the thesis work will be explained in detail. The work was carried out using *MATLAB* software and its integrated software *Simulink*. As described in the previous chapter, the work will focus on a compact SCAS system, whose components in brief are: Jet-pipe valve, SCAS actuator, LVDT, Controller. Figure 13 shows a functional diagram of the system under analysis.

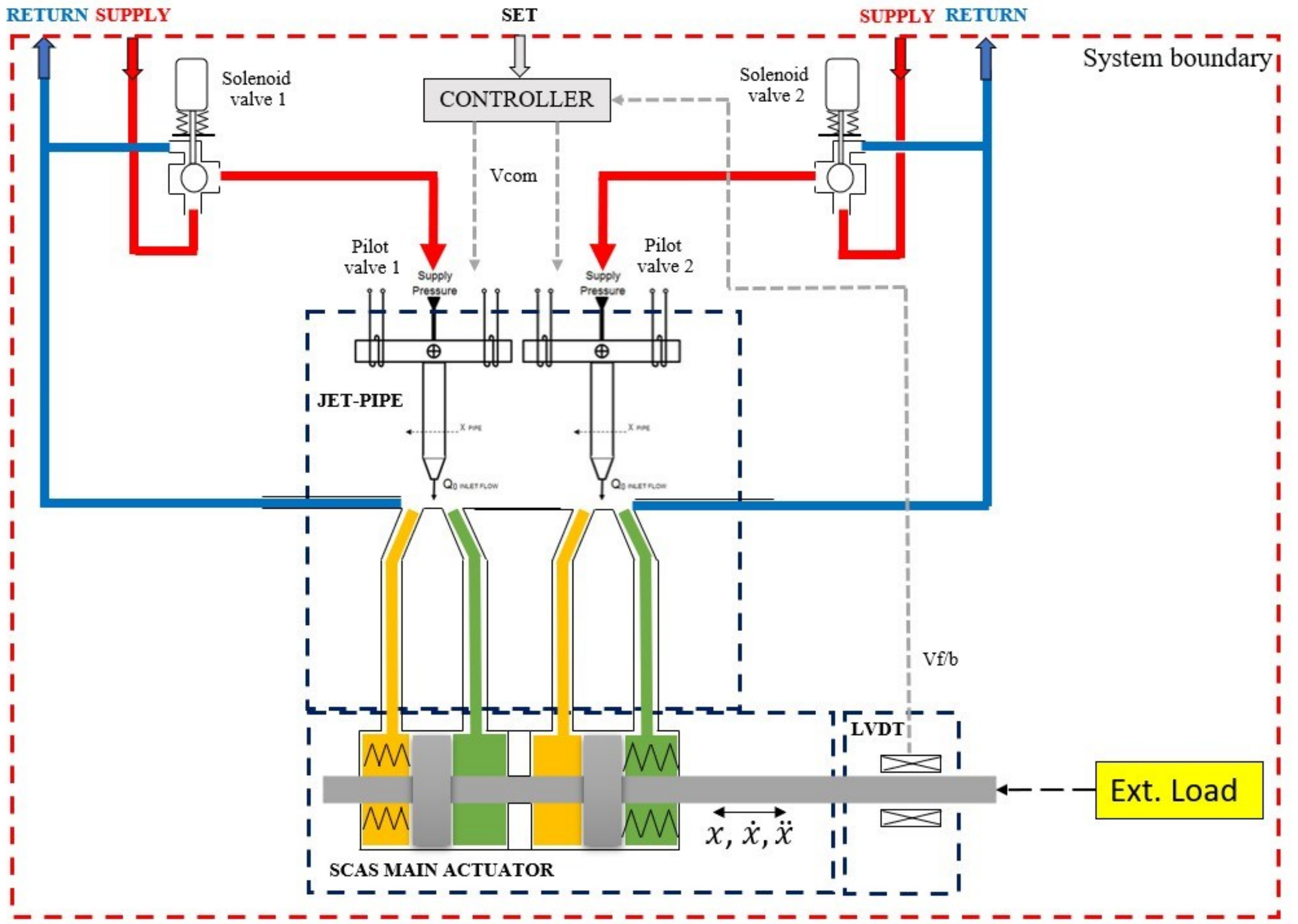

Figure 13: Integrated SCAS actuator diagram

As can be seen, the system consists of two jet-pipe valves that hydraulically feed a double acting hydraulic piston with two separate chambers. Then there is an LVDT transducer connected to the piston rod that measures its position and sends the feedback signal to the controller. External loads reacting to the actuator's motion are also considered with approximations. Finally, there are two solenoid valves that function as hydraulic On/Off switch of the SCAS system in case it is integrated into a more complex system such as the MRA. Due to the symmetry of the system involving the two jet-pipes, the modelling was initially carried out by considering only one and then adding the second jet-pipe and duplicating what was done for the first. The modelling work was performed starting with a definition of an electrical and magnetic circuit, followed by the torque motor model and then the dynamic model of the jet-pipe. Consequently, an accurate model of the hydraulic circuit was developed, which also required significant effort due to the intrinsic instability of the single-stage system. The SCAS actuator was then dimensioned and modelled. Finally, an LVDT transducer and a type *PID* controller were implemented. The architecture of the SCAS model, suitably revised and deepened for the needs of the study in this thesis, was developed from what is stated in reference no. [12], for more details on MRA command modelling, please refer to that thesis reference.

The desired cardinal requirements from which it was possible to proceed with the modelling were:

Parameter	**Symbol**	**Value**	**Unit of measurement**
Supply Pressure	P_s	17 – 20	MPa
Return Pressure	P_r	0,3 – 0,7	MPa
Operating fluid		MIL-PRF-5606 MIL-PRF-83282 MIL-PRF-87257	
Temperature of hydraulic fluid	T	-40 to 135	°C

Inlet flow at rated pressure (at 20 °C)	Q	0,45	$\frac{l}{min}$
Coils configuration		Two independent coils	
Rated current	i_{sv}	8	mA
Maximum Voltage	V_{rif}	10	V
Frequency response (Jet-pipe travel versus input current)		Amplitude ratio greater than $-3\ dB$ and phase lag lower than 90° for frequencies lower than 400 Hz	

Further key data, as well as complementary data, will be adequately outlined in the course of the paper. In addition, there is a measured flow pressure characteristic for supply pressure Ps 17 MPa for fluid temperature > -10 °C (fig. 14).

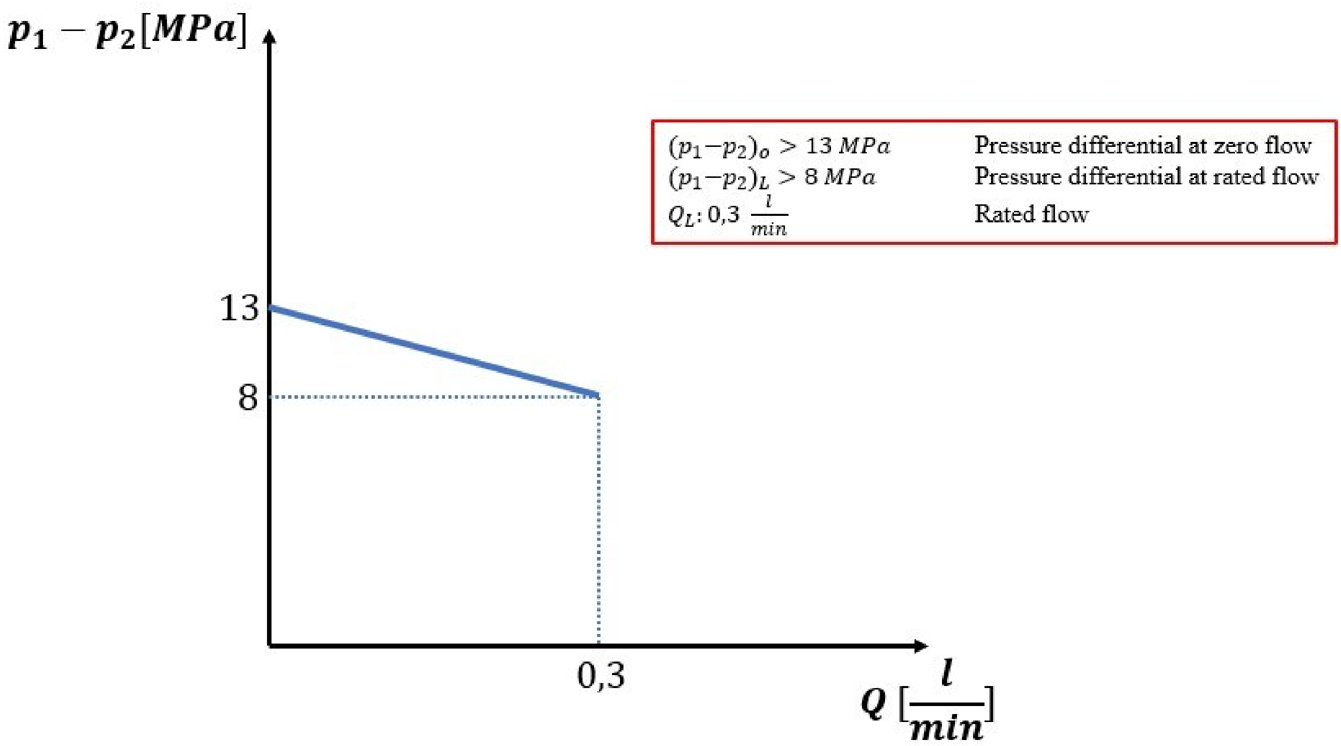

Figure 14: Pressure/Flow characteristic for Ps 17 MPa and T ≥ -10 °C

This characteristic will be one of the targets of the modelling and the results obtained will be presented in the following chapter.

The Simulink model of the compact SCAS system is now illustrated, starting with the first level visible in figure 15.

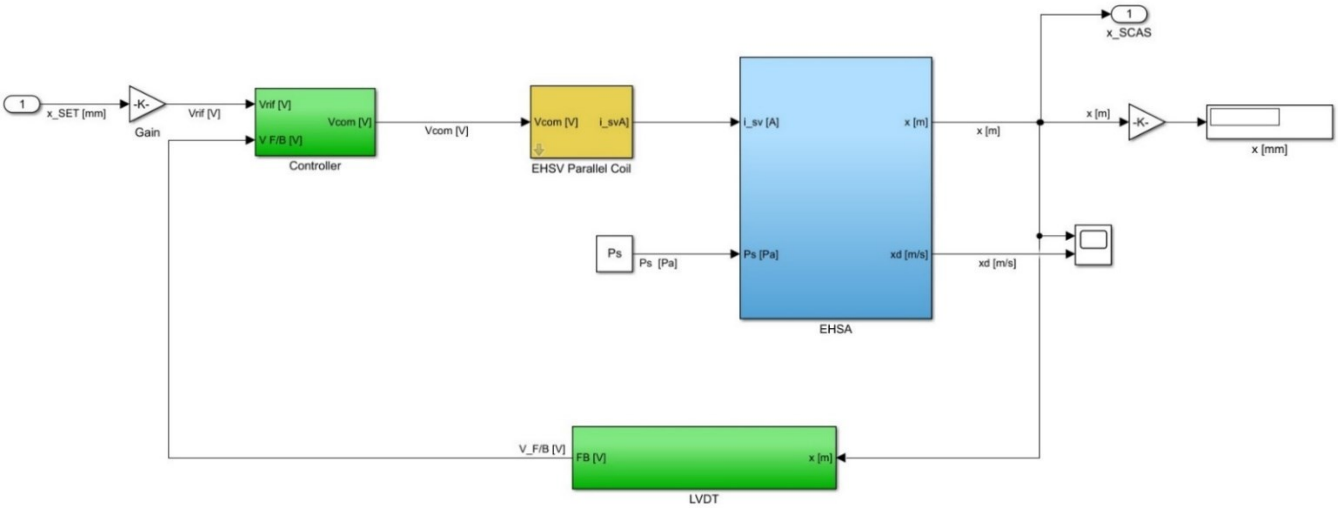

Figure 15: First level of Simulink SCAS model

As can be seen, the model has an input *x_SET,* which establishes the position to be taken by the SCAS actuator, followed by a *Gain* to transform the SET information expressed in millimetres into a voltage signal expressed in volts via the relation: $\frac{V_{rif}}{L_{la}*1000}$, where L_{la} is SCAS actuator half cylinder stroke. Then we find the *Controller* to compensate for the error between SET and feedback sent by the *LVDT* transducer block which can read the current rod position. The armature circuit of the torque motor consists of two coils connected in parallel, that are represented by the *'EHSV Parallel Coil'* block. Moreover, there is *EHSA* block were SCAS Actuator, SCAS dynamic (which include hydraulic circuit model), external load dynamic and solenoid valves are described. The elements just outlined can be seen in figure 16, which represents the system into the EHSA block. Finally, there is *x_SCAS* output representing the position assumed by the SCAS actuator rod as response to the input signal.

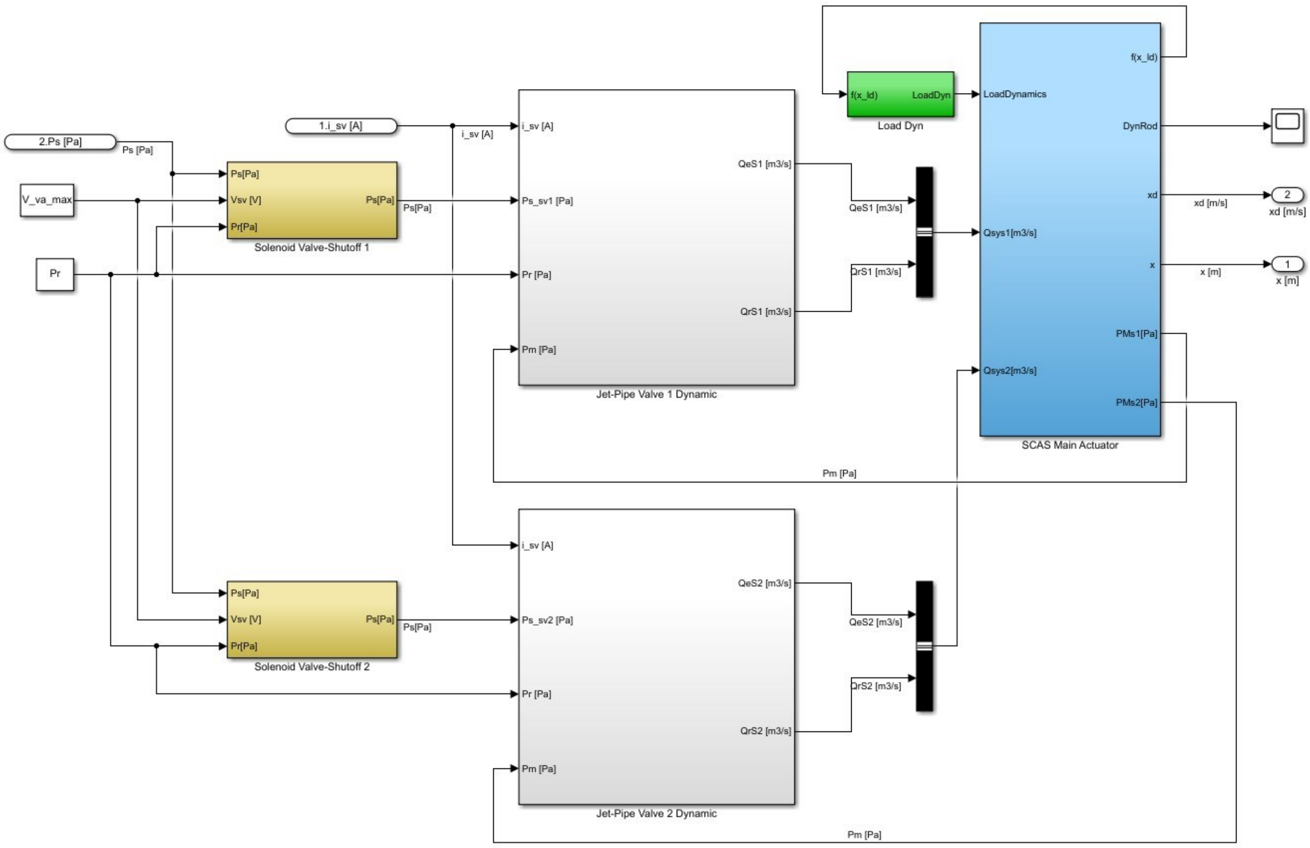

Figure 16: View inside the Simulink EHSA block

Entering the *'Jet-Pipe Valve Dynamic'* block, the magnetic model of the *torque motor* can be found, which, given a current input, returns a torque, the *dynamics of the jet-pipe* and the *hydraulic circuit* that allows the flow rate delivered by the valve to be derived (fig. 17).

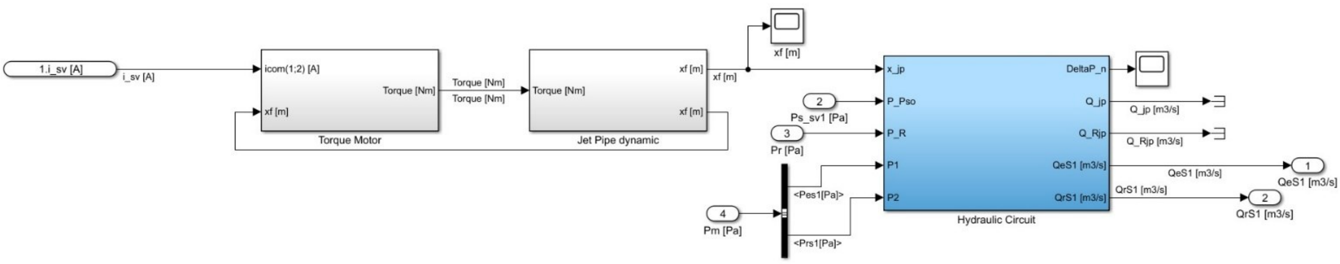

Figure 17: View inside the Simulink Jet-Pipe Valve Dynamic block

2.1 Torque Motor

The analysis begins with the description of the *torque motor* model. As already stated in the previous chapter, the torque motor circuit consists of two coils in parallel. In the model, the electrical circuit which is within the "*EHSV Parallel Coil*" block and the magnetic circuit located in the "*Torque Motor*" block will be considered separately. This analysis will have as input the voltage on the coils *Vcom* and as output the torque supplied by the motor. The application of a control signal results in a voltage *Vcom,* through the relations described below, makes it possible to derive a circulating current *i_sv:*

$$V_{com} = R_{c_{sv}} i_1 + L_s \frac{di_1}{dt} \quad \text{and} \quad V_{com} = R_{c_{sv}} i_2 + L_s \frac{di_2}{dt}$$

Where:

i_1 and i_2 are the command current in the coils.

$R_{c_{sv}}$ is the rated coils resistance.

L_s is the inductance of the coils.

By inducing a k_{amp} gain, considering the number of windings *N* and chained magnetic field ϕ_a, can be determined:

$$i_{sv} = \frac{i_1 - i_2}{2} = k_{amp} \frac{V_{com}}{R_{c_{sv}}} - \frac{N}{R_{c_{sv}}} \frac{d\phi_a}{dt}$$

Considering Hopkinson's law:

$$i_c = Ni = \oint_{\partial S} H \, dl = \oint_{\partial S} \frac{\phi_c}{\mu_f S} dl = \phi_c \oint_{\partial S} \frac{dl}{\mu_f S} = \phi_c \mathcal{R}$$

Where:

i_c is the current concatenated to the circuit.

H is magnetic field.

S is the surface considerate.

$\mathcal{R}$ is the magnetic reluctance of the circuit.

Hopkinson's law shows that also:

$$Ni = \mathcal{R}\phi_c$$

$$\mathcal{R} = \frac{Ni}{\phi_c}\frac{N}{N}, \text{ whereas } L = N\frac{\phi_c}{i}, \text{ thus } \mathcal{R} = \frac{N^2}{L}$$

Making the appropriate adjustments to the equations described, it was possible to determine the current using the Simulink block presented in section 2.1.1. Pursuing the analysis, concerning the magnetic circuit, it must be specified that in this application the two permanent magnets are positioned internally in the magnetic circuit as shown in figure 18.

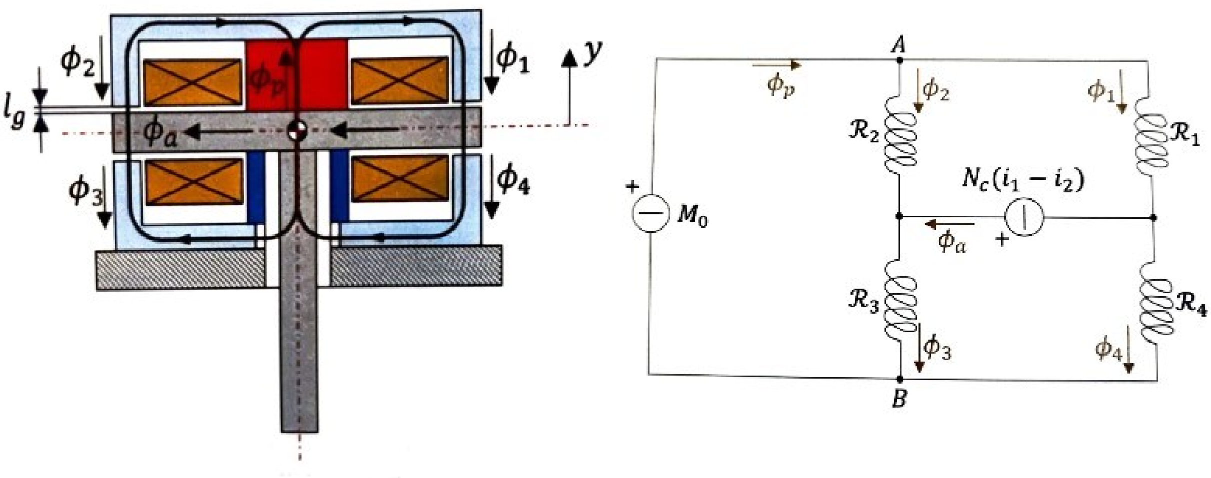

Figure 18: Diagram of torque motor with central permanent magnet and electrical equivalent of the magnetic circuit [8]

The objective now is to determine the *torque* generated by the motor *Tm*. As can be seen in figure 18, the pole size is much larger than the gap size and thus the magnetic flux density can be considered constant. This simplification leads to writing the resulting momentum *M1* equation considering only one pole:

$$M_1 = \frac{B_1 H_1}{2}\frac{L_A A_g}{2} = \frac{B_1^2}{4\mu_0} L_A A_g$$

Where:

B_1 is the magnetic flux density in air gap 1.

H_1 is the magnetic field of pole in the air gap 1.

L_A is the distance between poles, the same for all the gaps.

A_g is the cross-sectional area of the gap, the same for all the gaps.

μ_0 is magnetic permeability.

The other three poles generate similar moments, it is possible to write the equation of *Tm:*

$$T_m = \frac{L_A A_g}{4\mu_0}(B_1^2 - B_2^2 + B_3^2 - B_4^2) = \frac{L_A}{4\mu_0 A_g}(\Phi_1^2 - \Phi_2^2 + \Phi_3^2 - \Phi_4^2)$$

Where:

$\Phi_{1,2,3,4}$ are the magnetic flux through air gaps 1,2,3,4.

It is possible to define these magnetic fluxes through applying *Ampere's theorem* and *Gauss's rule* and with the consideration of all gaps symmetrical:

$$\begin{cases} \Phi_1 = \Phi_3 = \dfrac{A_g \mu_0 (1+\xi) V_p + (k+1+\xi) V_a}{2 l_0 (k+1-\xi^2)} \\ \Phi_2 = \Phi_4 = \dfrac{A_g \mu_0 (1-\xi) V_p - (k+1-\xi) V_a}{2 l_0 (k+1-\xi^2)} \end{cases}$$

Where:

$l_1 = l_3 = l_0 - x$ and $l_2 = l_4 = l_0 + x$, with l_0 is the average of the four air gaps.

$\frac{R_p}{r R_g} = \frac{k_1 \mu_0 A_g l_p}{r \mu_p A_p l_0}$ and $\xi = \frac{x}{l_0}$ and $V_a = ni$

Where:

R_p is the magnetic reluctance of the permanent magnet.

R_g is the magnetic reluctance of the gap.

r is magnetic flux through air gaps/magnetic flux though magnet.

k_1 is adimensional value depending on the B distribution.

μ_p is permeability of the permanent magnet.

A_p is cross-sectional area of permanent magnet.

l_p is the length of permanent magnet.

V_a is magnetomotive force generated by the coils.

V_p is magnetomotive force generated by the permanent magnet.

n coil turns.

Finally, the below equation can be written:

$$T_m = \frac{L_A A_g \mu_0 \left(V_p + \xi V_a\right)[\xi V_p + (1+k)V_a]}{2l_0^2(k+1-\xi^2)^2}$$

It is possible to make some simplification:

k value is usually between 9 and 16.

The value $V_p \gg V_a$

ξ in the denominator can be ignored due to the small value change respect to k

Lastly, the output torque *Tm* generated by motor is:

$$T_m = \frac{L_A A_g \mu_0 V_p^2[\xi V_p + (1+k)V_a]}{2l_0^2(k+1)^2}$$

The information given represents the logical and mathematical steps that led to the definition of the model and is not intended to be an exhaustive analysis as it does not concern this thesis work. For further details, please refer to the references used for this paragraph: the book [8] and the papers [13][14][15]. Numerical values, variable names used in the Simulink model and mathematical data operations will be explained in the MATLAB data file chapter.

2.1.1 Simulink Model of Torque Motor

The Simulink model realised is now presented (fig. 19).

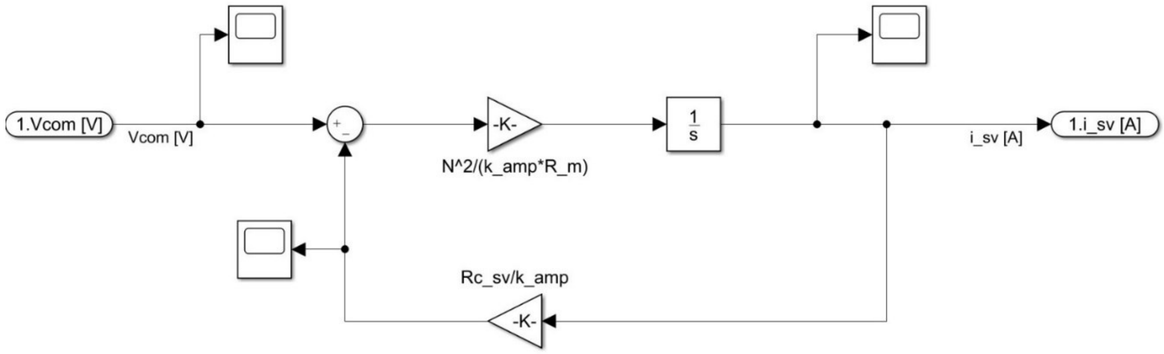

Figure 19: View inside the Simulink EHSV Parallel Coil block

The coil current *i_sv* thus obtained is given as an input to the model of the Torque Motor's magnetic circuit (fig. 17), a detail of which can be seen in the figure 20. Furthermore, the block receives as input the linear displacement of the jet-pipe *xf*.

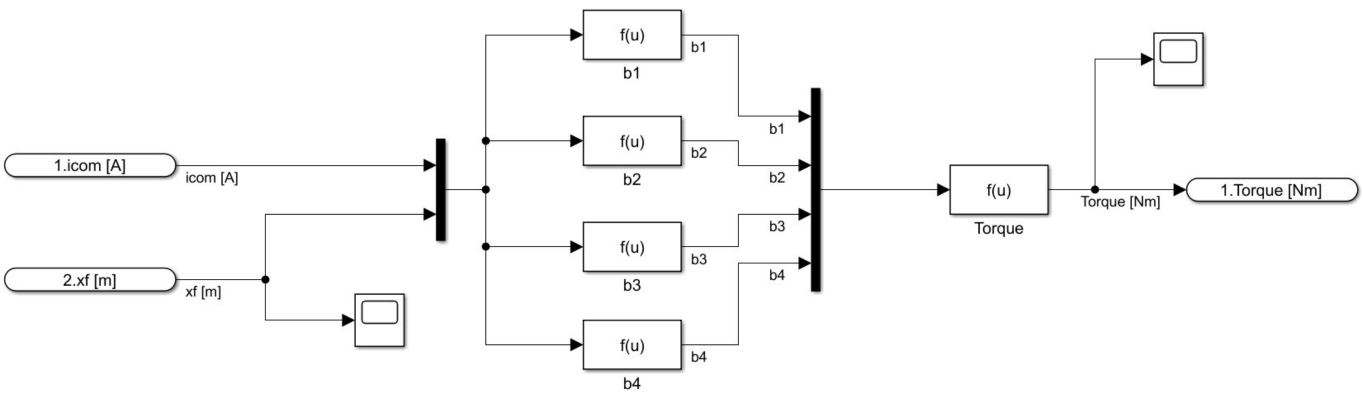

Figure 20: View inside the Simulink Torque Motor block

2.2 Jet-Pipe Dynamic

In this section is analyzed the model of the dynamic behavior of the jet-pipe, which results in the Simulink block visible in figure 17 *'Jet Pipe Dynamic'*. The objective is to determine the linear displacement of the jet-pipe, which will be the output, as input there is the torque provided by the torque motor which allows the system to rotate. For this purpose, it is necessary to analyze the free-body diagram in figure 21.

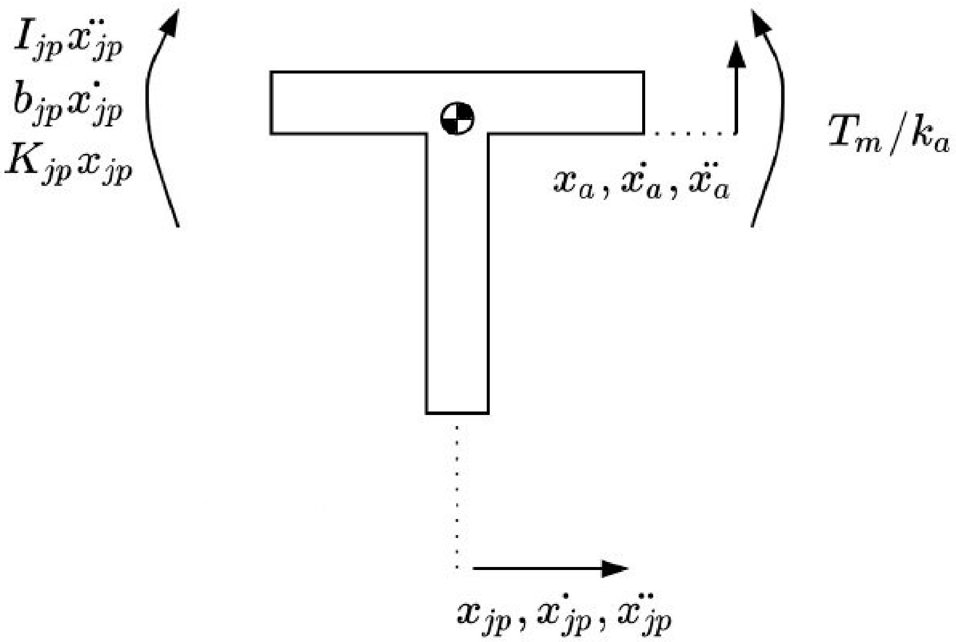

Figure 21: Jet-pipe free-body diagram

As can be seen, unlike classical jet-pipe systems, the one under investigation does not have a feedback spring but is only governed by the controller, which led to some instability problems when testing the model, which were successfully overcome by setting the values appropriately. For a discussion of classical jet-pipe dynamics, please consult the reference used for this section [8]. It is now possible to define a dynamic equation:

$$I_{jp}\ddot{x}_{jp} = \frac{T_m}{k_a} - b_{jp}\dot{x}_{jp} - K_{jp}x_{jp}$$

Where:

x_a is armature displacement.

x_{jp} is jet-pipe displacement.

$k_a = \frac{x_{jp}}{x_a}$ is adimensional value that correlates two displacements.

I_{jp} is rotational mass of armature.

b_{jp} is jet-pipe damping.

K_{jp} is jet-pipe stiffness.

With the equation thus defined, it is possible to determine the linear displacement x_{jp}, which will subsequently determine the amount of fluid sent to the chambers of the SCAS actuator. Note, that it has been worked under the assumption that small angular rotations are assimilated to linear displacements.

2.2.1 Simulink Model of Jet-Pipe Dynamic

The Simulink model realised is described below (fig. 22).

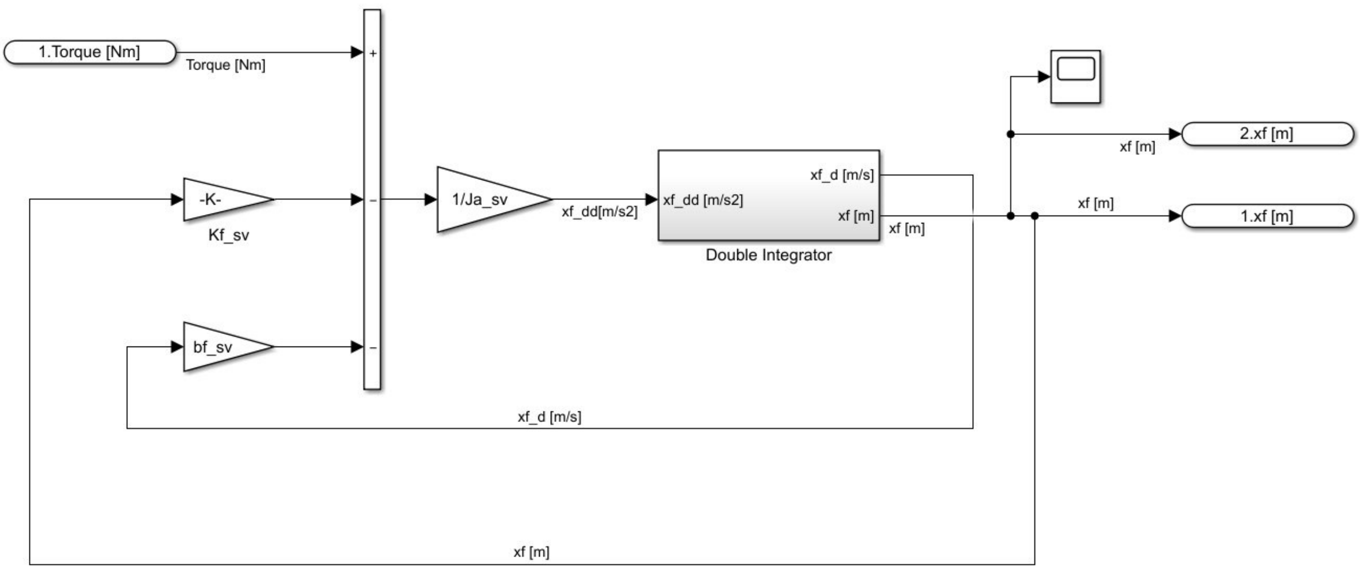

Figure 22: View inside the Simulink Jet Pipe dynamic block

As can be seen on the output of the block there is x_{jp}, renamed *xf* in the Simulink model. The value of damping and stiffness, *Kf_sv and bf_sv*, were properly calibrated during the test phase, the results will be presented in the next chapter. Subsequently, there is a gain with the inverse of the rotational mass of armature, *Ja_sv,* thus obtains the acceleration value. Finally, in the double integrator block there are integrators necessary to obtain the velocity of the jet pipe and its position (fig. 23). These values will also go into retraction, in damping and stiffness gains.

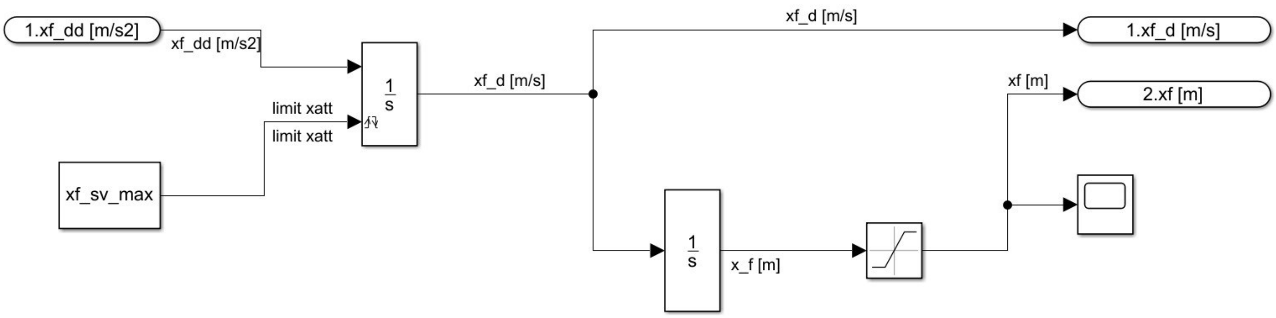

Figure 23: View inside the Simulink Double Integrator block

Note that the first integral has a reset condition equal to the maximum displacement *xf_sv_max*, while in output to the second integral there is a saturation equal to the maximum displacement plus 15%. This is intended to represent the real physical limits of the mechanism.

2.3 Hydraulic Circuit

It is now important to illustrate the model realized for the simulation of the hydraulic circuit (fig 24). The aim was to create a block which as input has the pressure and position information of the jet-pipe, and as output the flow rates supplied; in the case of the system under examination, these flow rates will be directly those who supplied the actuator because there isn't a second stage. Briefly, the work can be divided into three parts: the first is to determine pressure at the exit of jet-pipe, the second is to determine the flow areas of the hydraulic fluid and the third is to calculate the flow rate into or out of the actuator.

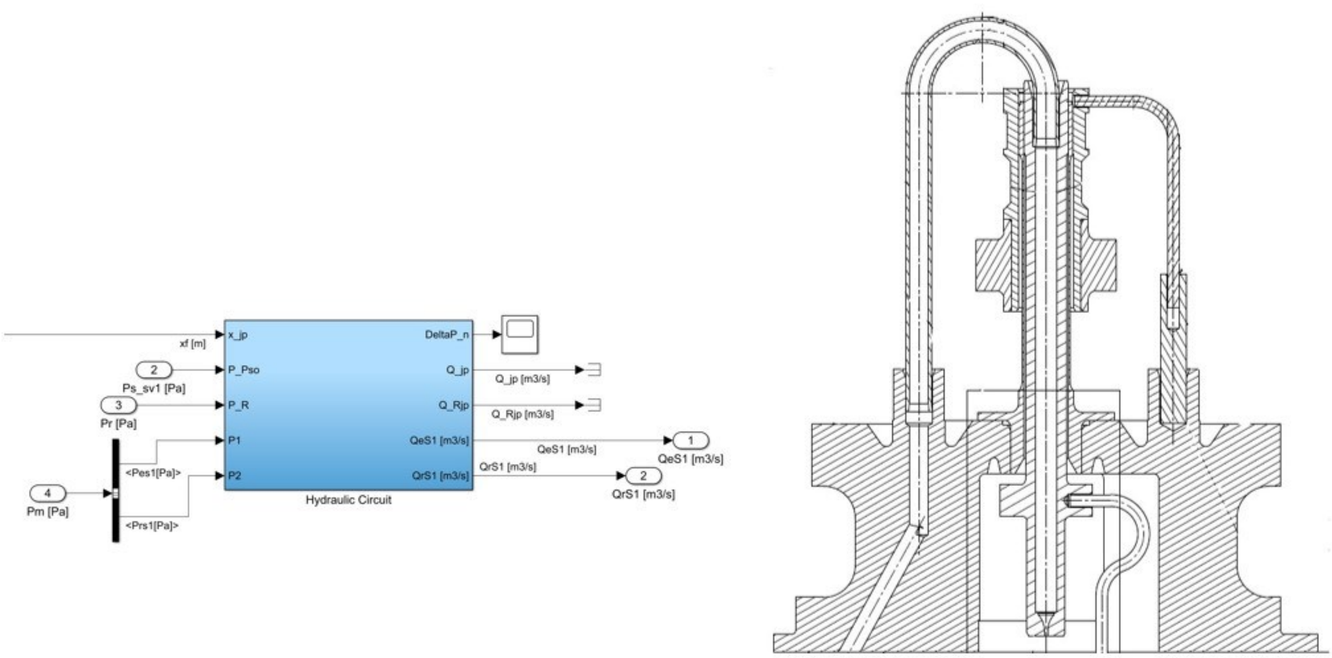

Figure 24: Simulink Hydraulic Circuit block and section view of jet-pipe

It should be specified that the references for this analysis were: [16] for the calculation of the hydraulic resistance, and papers [17][18][19][20] for the modelling. Please refer to these sources for a more detailed analysis. Furthermore, detailed data will be provided in the related chapter. The analysis then begins by determining the pressure at the exit of jet-pipe P_{jp}:

$$P_{P,SO} - P_{jp} - \Delta P_{pipe} - \Delta P_{orefice} = C_{idr}\dot{Q}_{jp}$$

Where:

$P_{P,SO}$ is the supply pressure.

P_{jp} is the pressure at the exit of pipe.

ΔP_{pipe} is piping pressure drop.

$\Delta P_{orefice}$ orifice pressure drops.

C_{idr} is hydraulic capacity.

$\dot{Q}_{jp}$ is jet-pipe flow rate.

Firstly, to determine the pressure drop in the pipe ΔP_{pipe} the number of Reynolds *Re,* function of flow rate, is calculated to determine if the flow is laminar or turbulent. Subsequently, depending on the type of flow, *Darcy's friction coefficient* λ is calculated via the *Colebrook-White equation* if the flow is turbulent:

$$\frac{1}{\sqrt{\lambda}} = -2{,}03 \log\left(\frac{2{,}51}{Re\sqrt{\lambda}} + \frac{\varepsilon/D}{3{,}71}\right)$$

Or if laminar flow (*Re < 2000)*:

$$\lambda = \frac{64}{Re}$$

Thus, it can be proved that:

$$\Delta P_{pipe} \approx p_1 - p_2 = 8\frac{wL\mu}{R^2} = \lambda\frac{L_{pipe}}{D_{pipe}}\frac{8Q_{jp}^2 D_{pipe}^4}{\pi^2}\rho$$

The next step is to determine the concentrated hydraulic losses $\Delta P_{orefice}$, considering the conformation of the circuit shown in figure 24:

$$\Delta P_{orefice} = Q_{jp}\left(\frac{12\mu}{2{,}5}\frac{w_{bv}}{h_{bv}}\right) + Q_{jp}^2\left(\frac{\rho}{2}\frac{C_{eff}^2}{(w_{bv}^2 + (w_{bv} + h_{bv})^2)}\right)$$

Where:

w_{bv} is pipe entrance width.

h_{bv} is pipe radial clearance.

C_{eff} is efflux coefficient.

Thus, pressure at the exit of jet-pipe P_{jp} is determined.

The model now proceeds to determine the passage areas of the fluid sent by the jet-pipe. Figure 25 shows the construction characteristics of the jet-pipe and receiver, the jet-pipe as it moves sends fluid to the left or right channel.

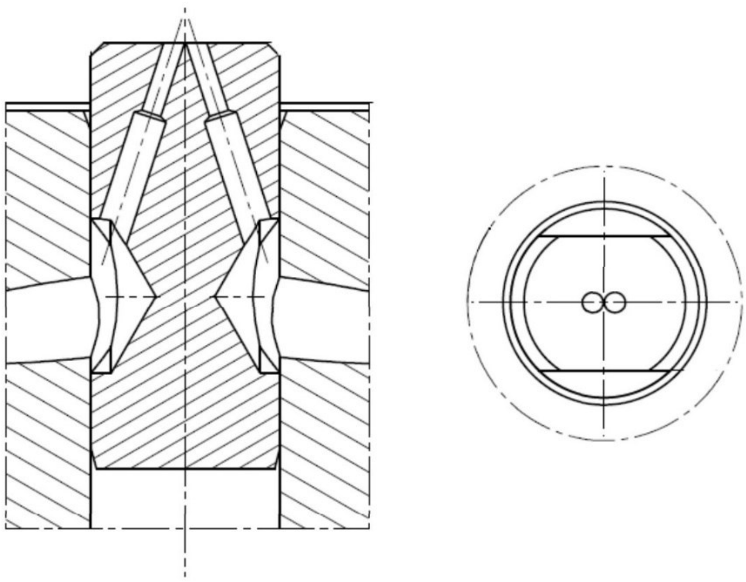

Figure 25: Section view of the receiver (left), top view of the receiver (right)

From a schematic point of view, this behaviour can be described as in figure 26. This mechanism results in different areas of fluid passage.

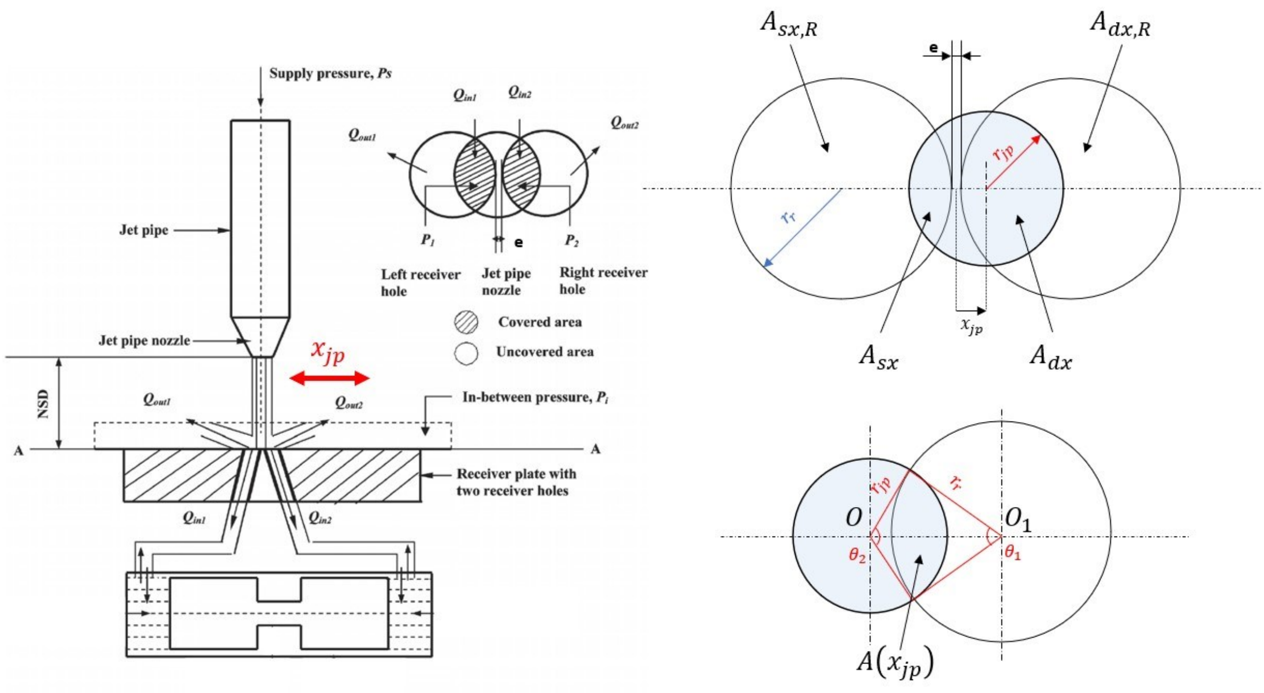

Figure 26: Jet-pipe functional diagram and flow passage areas

From the diagrams provided in figure 26, it is possible to define the mathematical equations:

$$A(x_{jp}) = \frac{r_r^2\theta_1 + r_{jp}^2\theta_2 - \left[r_r^2 \sin\theta_1 + r_{jp}^2 \sin\theta_2\right]}{2}$$

Where, r_{jp} is the radius of jet-pipe flow defined as:

$$r_{jp}^2 = r_r^2 + (\overline{OO_1})^2 - 2r_r(\overline{OO_1})\cos\frac{\theta_1}{2}$$

And r_r is the radius of receiver hole:

$$r_r^2 = r_{jp}^2 + (\overline{OO_1})^2 - 2r_{jp}(\overline{OO_1})\cos\frac{\theta_2}{2}$$

Where the centre distance $\overline{OO_1}$ is given by:

$$\overline{OO_1} = \frac{e + D_r}{2} = 0{,}5e + r_r - x_{jp}$$

Where e is the distance between the two receiving holes. Thus:

$$\theta_1 = 2\cos^{-1}\left(\frac{r_r^2 + (r_r + 0{,}5e - x_{jp})^2 - r_{jp}^2}{2r_r(r_r + 0{,}5e - x_{jp})}\right)$$

$$\theta_2 = 2\cos^{-1}\left(\frac{r_{jp}^2 + (r_r + 0{,}5e - x_{jp})^2 - r_r^2}{2r_{jp}(r_r + 0{,}5e - x_{jp})}\right)$$

Hence, in the case under consideration:

$$A_{dx} = \frac{r_r^2\theta_{dx} + r_{jp}^2\theta_{dx\prime} - \left[r_r^2\sin\theta_{dx} + r_{jp}^2\sin\theta_{dx\prime}\right]}{2}$$

$$A_{dx,R} = \pi r_r^2 - A_{dx}$$

$$A_{sx} = \frac{r_r^2\theta_{sx} + r_{jp}^2\theta_{sx\prime} - \left[r_r^2\sin\theta_{sx} + r_{jp}^2\sin\theta_{sx\prime}\right]}{2}$$

$$A_{sx,R} = \pi r_r^2 - A_{sx}$$

Afterwards, the volume flow rate through an orifice is given by:

$$Q = C_d A\sqrt{\frac{2}{\rho}\Delta p}$$

Thus:

$$Q_{SX} = \sqrt{\frac{P_{jp} - P_{SX}}{\frac{\rho}{2}}}A_{sx}C_d$$

$$Q_{DX} = \sqrt{\frac{P_{jp} - P_{DX}}{\frac{\rho}{2}}}A_{dx}C_d$$

$$Q_R = Q_{R,DX} + Q_{R,SX} = \sqrt{\frac{P_{DX} - P_r}{\frac{\rho}{2}}}A_{dx,R}C_d + \sqrt{\frac{P_{SX} - P_r}{\frac{\rho}{2}}}A_{sx,R}C_d$$

And because e is very small it is possible to approximate:

$$Q_{jp} \approx Q_{DX} + Q_{SX}$$

Finally, it is possible to determine the flow rate at actuator chambers:

$$Q_{eS1} = Q_{DX} + Q_{R,DX}$$

$$Q_{rS1} = Q_{SX} + Q_{R,SX}$$

Where:

P_{DX} is the pressure right actuator chamber.

P_{SX} is the pressure left actuator chamber.

Q_R is the discharge flow rate.

Q_{eS1} is the summary flow rate in the right chamber, that produce a pull-out movement of the actuator.

Q_{rS1} is the summary flow rate in the right chamber, that produce a pull-back movement of the actuator. The hydraulics of the first stage of the servo valve are thus determined.

2.3.1 Simulink Model of Hydraulic Circuit

The realised Simulink model is now presented.

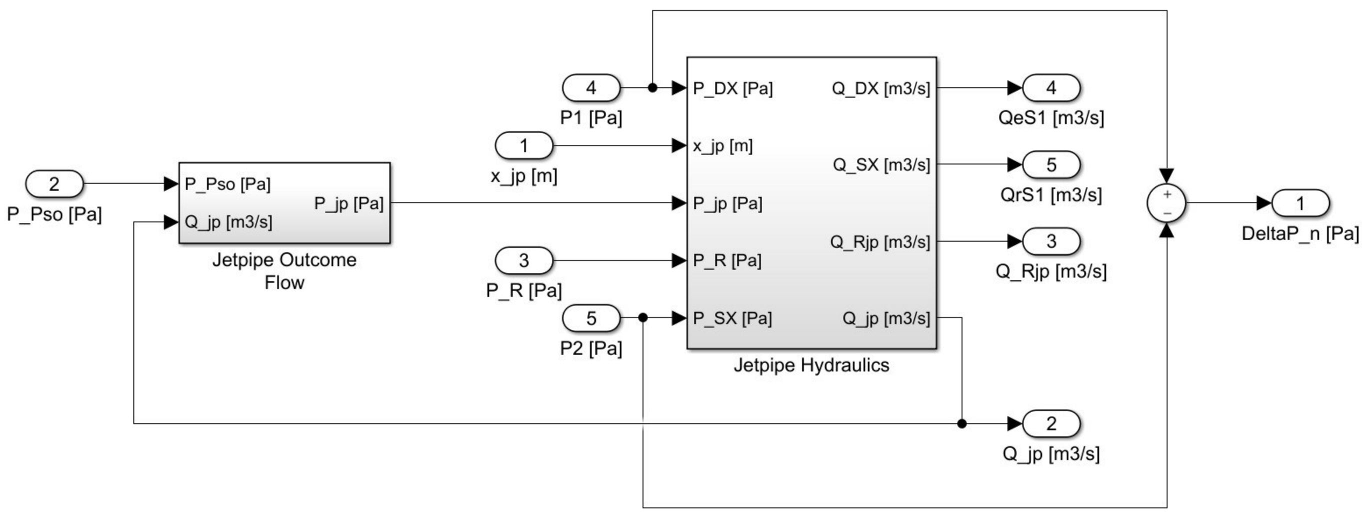

Figure 27:View inside the Simulink Hydraulic Circuit block

In input there are the pressure *P_pso, P_R, P1, P2* and jet-pipe displacement *x_jp*, while in output there are fluid flow rates *QeS1, QrS1, Q_Rjp, Q_jp*, the first two are sent to the actuator and the last two discharged.

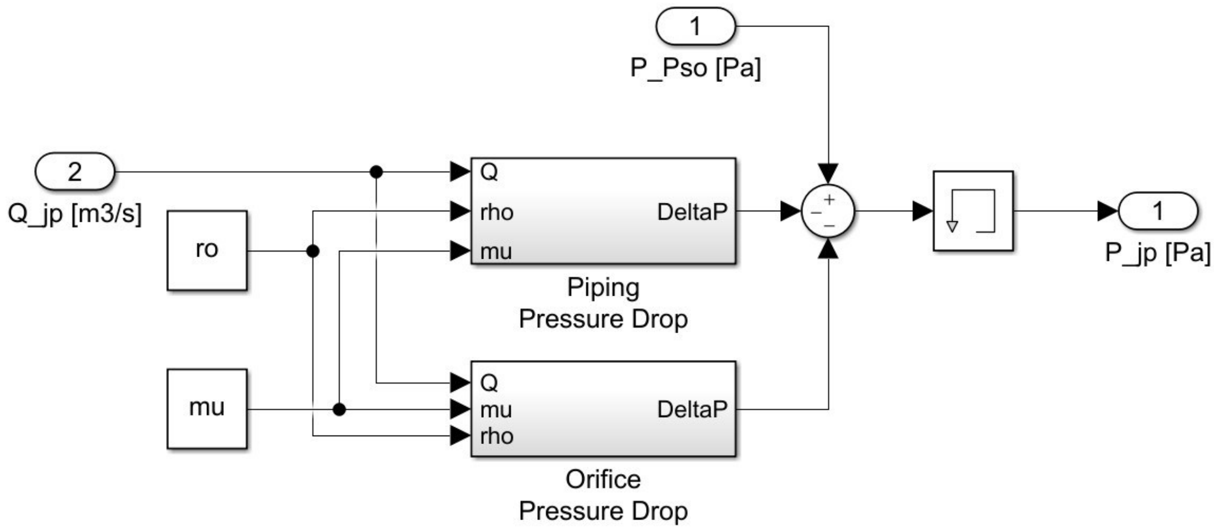

Figure 28: View inside Jetpipe Outcome Flow block

Inside *Jet-pipe Outcome Flow* block (fig. 28) pressure drop in the pipe (fig. 29) and concentrated hydraulic losses (fig. 30) are both calculated, in output there is the pressure downstream of the jet-pipe.

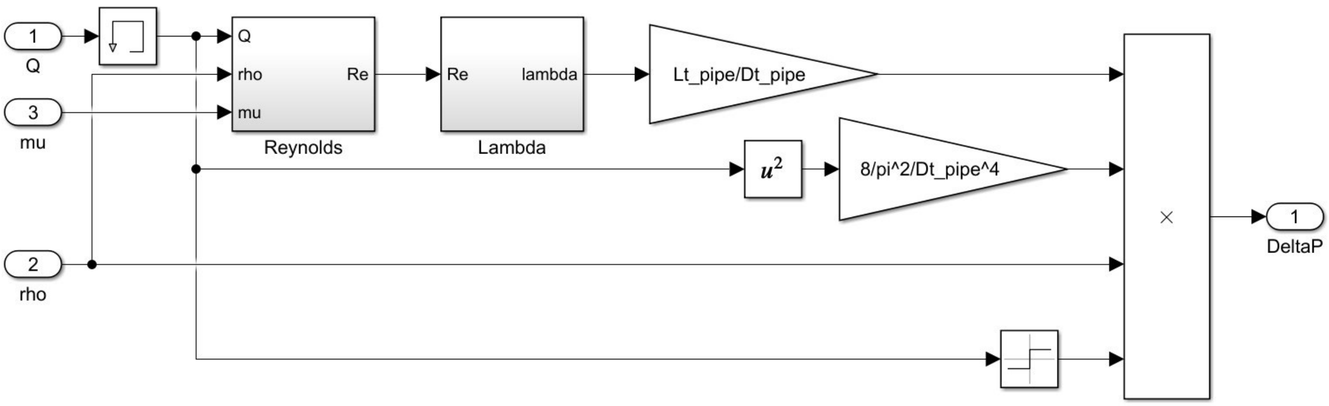

Figure 29: View inside Piping Pressure Drop block

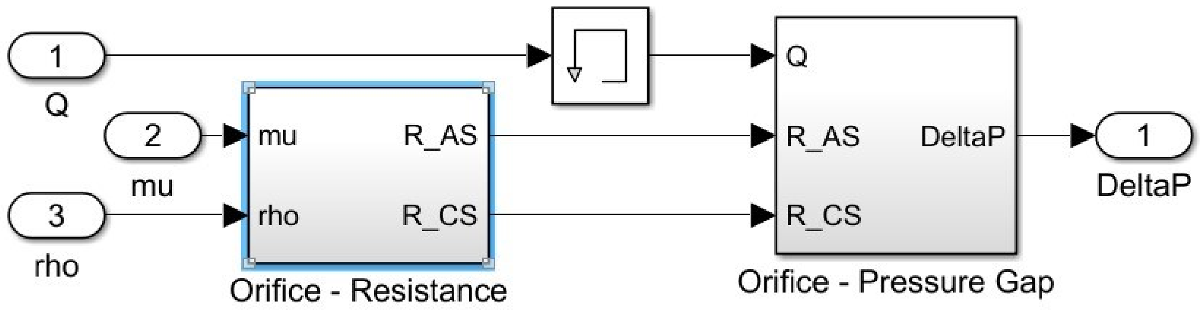

Figure 30: View inside Orifice Pressure Drop block

The analysis proceeds to examine what the *Jetpipe Hydraulics* block contains (fig. 31). As can be seen, *Nozzle Areas* is a block dedicated to calculating the fluid passage areas and the jet-pipe receiver/nozzle interaction.

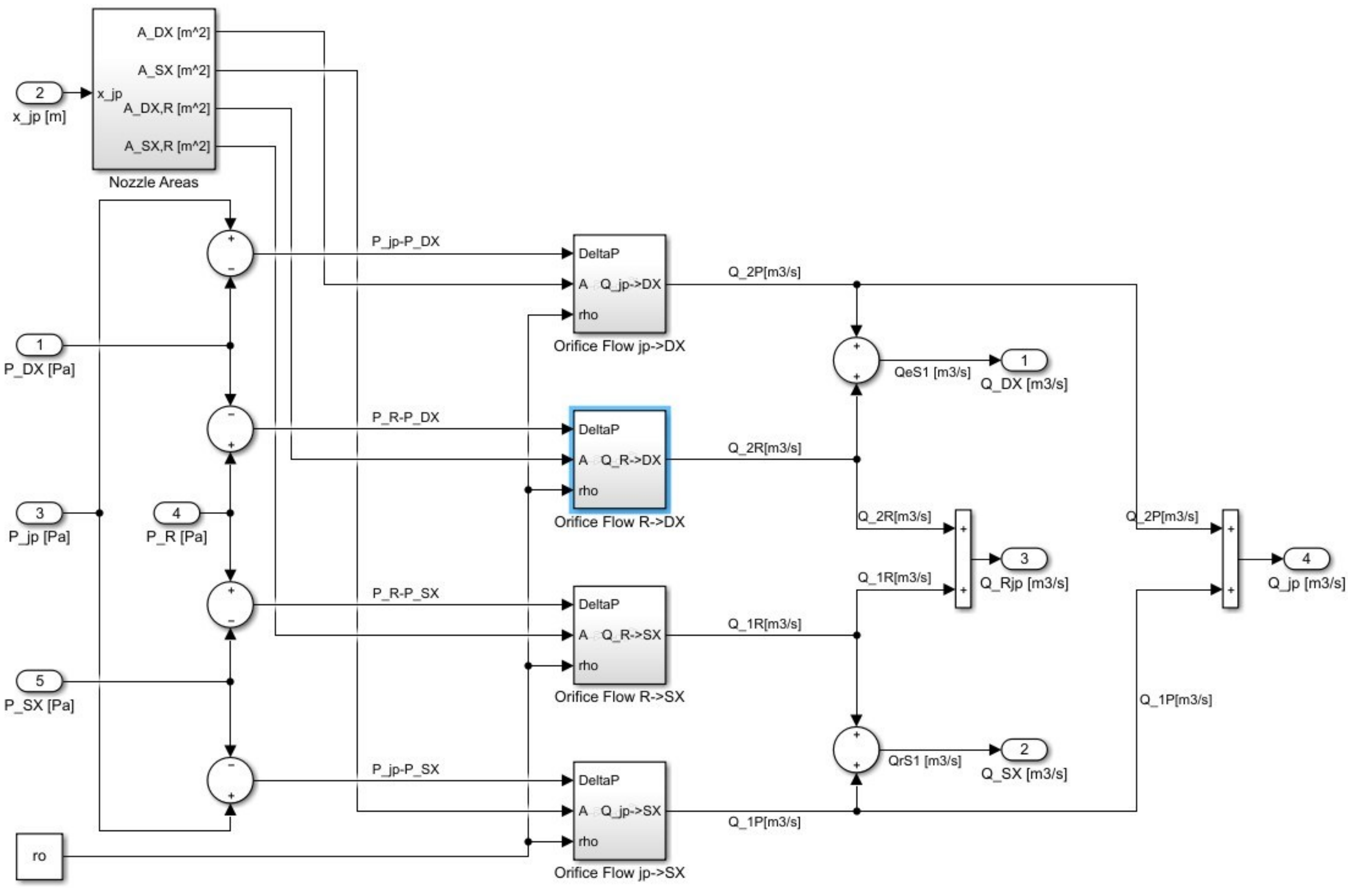

Figure 31: View inside the Jetpipe Hydraulics block

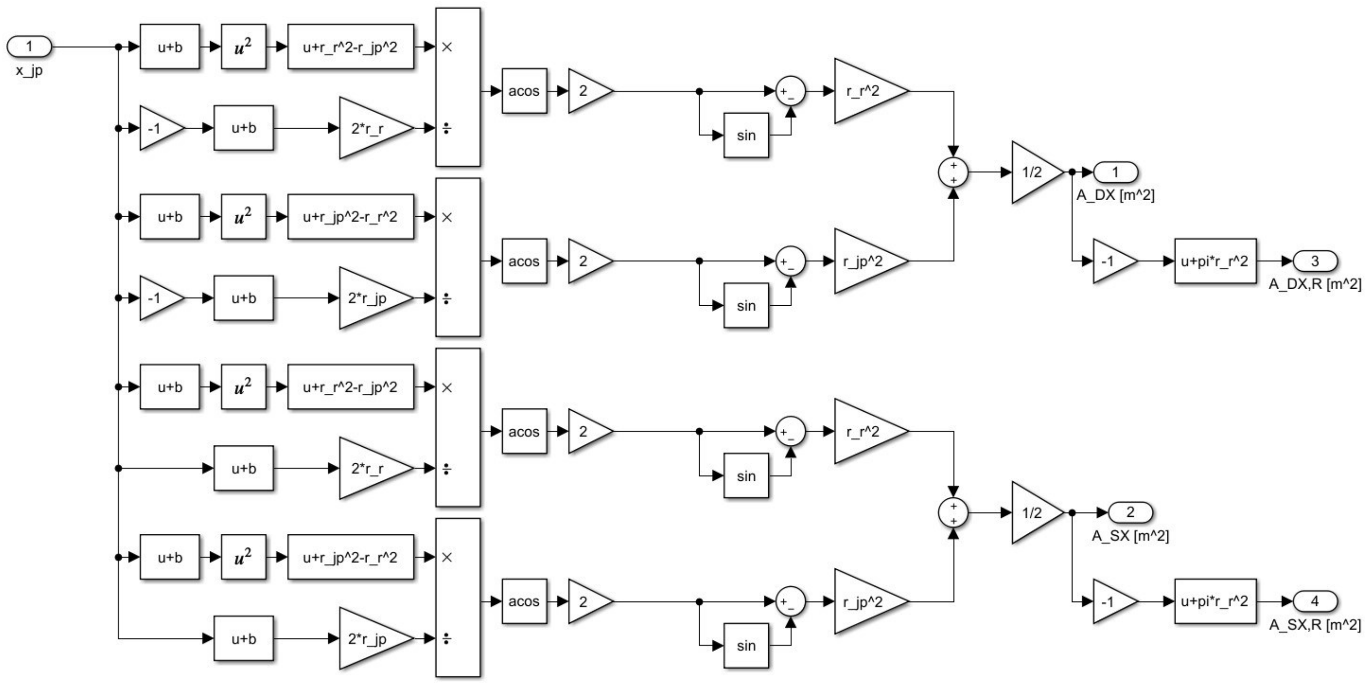

Figure 32: View inside Nozzle Areas block

Once the areas have been determined, and also the pressure deltas between the pressures coming from the actuator *P1* and *P2* and the output pressure of the jet-pipe and the return pressure *P_R*, the flow rates can be calculated as shown in figure 33.

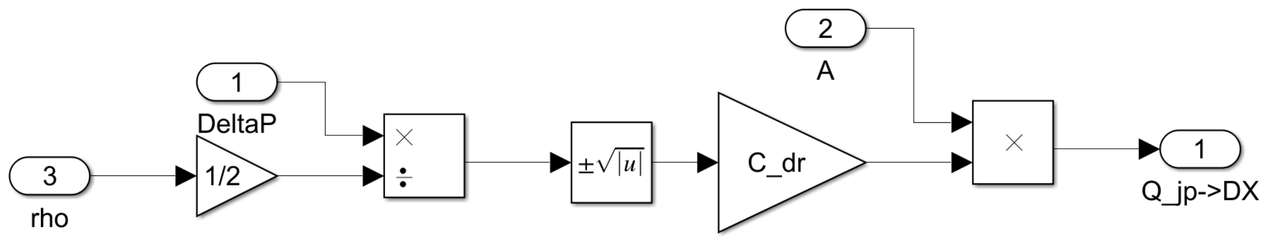

Figure 33: Flow rate calculation block

2.4 SCAS Actuator

The model study continues with the analysis of the *SCAS actuator with centering spring* model. The modelling and dimensioning of this actuator is one of the main purpose of this thesis. From the *continuity equation* in the two chambers of the actuator, it is possible to derive the two pressures P1 and P2 from the flow rates provided by the first stage of the jet-pipe calculated as seen in the previous paragraph.

$$\begin{cases} \rho(Q_1 - Q_l) = \dfrac{dm_1}{dt} = \dfrac{d(\rho V_1)}{dt} = \dfrac{d\rho}{dt}V_1 + \dfrac{dV_1}{dx}\rho \\ \rho(-Q_2 + Q_l) = \dfrac{dm_2}{dt} = \dfrac{d(\rho V_2)}{dt} = \dfrac{d\rho}{dt}V_2 + \dfrac{dV_2}{dx}\rho \end{cases}$$

Where:

m_1 and m_2 are the fluid masses in the chambers.

V_1 and V_2 are the volumes of the chambers.

Q_l is the leakage flow through the chambers of the actuator, derived from equations and considerations from references [7] and [12].

It is now considered the *Bulk modulus* β:

$$\frac{d\rho}{dt} = \frac{\rho}{\beta}\frac{dP}{dt}$$

As can be seen, the Bulk modulus changes depending on the operating conditions. Hence, a change in pressure and temperature in the chambers leads to a change in β and consequently affects the dynamics of the piston. The volume in the chambers varies with the piston position and can be defined as follows:

$$V = V_0 \pm A_e x$$

Where:

x is the rod displacement.

V_0 is the volume in the chamber when the piston is perfectly centered between the two chamber as for $x = 0$, is the same for both chambers

A_e is the effective thrust area.

Also considering the displacement speed of the piston $\dot{x}$, it is now possible to calculate, using an appropriate sign convention, the two pressures through the formulas:

$$\begin{cases} \frac{dP_1}{dt} = \frac{\beta}{V_1}(Q_1 - Q_l - A_e\dot{x}) \\ \frac{dP_2}{dt} = \frac{\beta}{V_2}(-Q_2 + Q_l + A_e\dot{x}) \end{cases}$$

The final result of this modelling is to determine the linear displacement of the rod. At this point, it is useful to introduce the scheme in figure 34. The model predicts the dynamic equilibrium of the cylinder because it is assumed that the cylinder is not connected to the structure by a perfect interlocking, but via a yielding bond modelled through the parallelism of a spring and damper. As will be seen later in the dimensioning phase, this assumption will not be applied and a dimensioning that conversely considers the cylinder connected to a rigid constraint will be considered as a good first approximation.

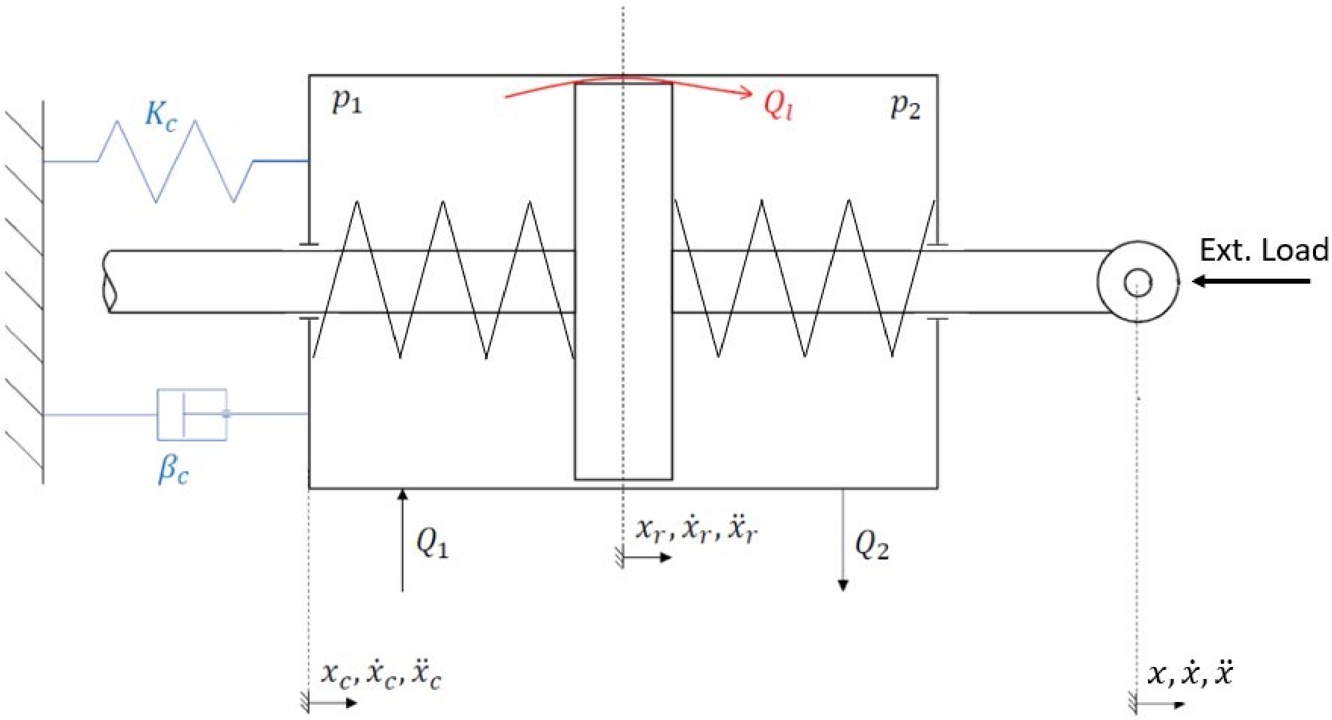

Figure 34: SCAS actuator diagram

Free body diagrams can be plotted consequently (fig. 35).

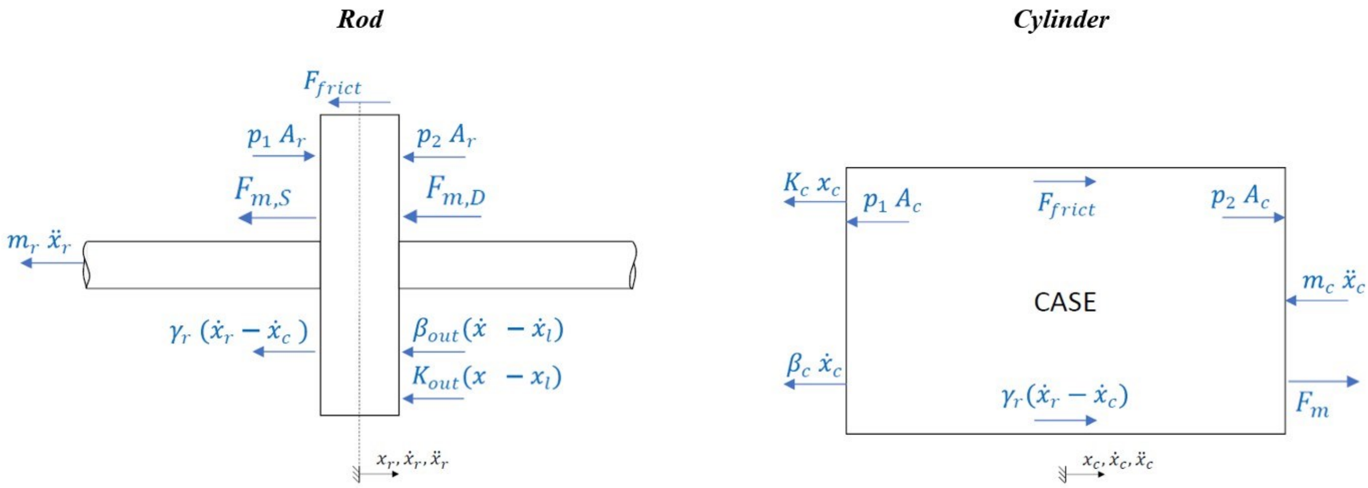

Figure 35: Free body diagrams of Rod on the left and Cylinder on the right side

It is possible to write the *equilibrium equation* of the rod:

$$(P_1 - P_2)A_e = m_r\ddot{x_r} + \beta_{out}(\dot{x} - \dot{x_l}) + \gamma_r(\dot{x_r} - \dot{x_c}) + K_{out}(x - x_l) + F_{frict} + F_m + F_{endstop}$$

And the equilibrium equation for the cylinder:

$$(P_1 - P_2)A_e + m_c\ddot{x_c} + \beta_c\dot{x_c} + K_c x_c = F_{frict} + F_m + \gamma_r(\dot{x_r} - \dot{x_c}) + F_{endstop}$$

Where:

$A_r = A_c = A_e$ is the effective thrust area, equal in both chambers.

m_r is the rod mass.

m_c is the cylinder mass.

$\dot{x_l}, x_l$ are the velocity end the position of external load.

β_{out} is the damping of the rod.

K_{out} is the rod stiffness.

β_c is the damping of the cylinder.

K_c is the cylinder stiffness.

γ_r is viscous friction coefficient for the relative displacement between fluid inside the cylinder and the piston.

$\dot{x_r}, \dot{x_c}$ are the relative velocity of the rod and the cylinder.

$\ddot{x_r}, \ddot{x_c}$ are the relative acceleration of the rod and the cylinder.

$F_m = F_{m,0} + K_c x$ is force of centering springs defined by *Hooke's law*, both left and right with an equal preload $F_{m,0}$.

$F_{endstop}$ is a force used to simulate the stroke limit for both the rod and cylinder, it intervenes when a certain value of x limit is reached. It compensates and opposes the force that would tend to further increase displacement.

A brief explanation must be made regarding friction force F_{frict}. The friction model used to describe the in-cylinder friction of SCAS considers the fact that this is a highly non-linear process, for example at low temperatures the frictional forces in the SCAS actuator will be greatly increased and even more than doubled for particularly low temperatures [23]. *Stribeck curves* can explain friction process with a lubricant layer [21]. The following equation was used to model friction:

$$F_{frict} = F_{st}\left(1 + ae^{-b|\dot{x}_r|}\right) + \gamma|\dot{x}_r|$$

Where:

a, b are empirical constants.

γ is viscous friction coefficient.

$\dot{x}_r$ is the relative velocity between the surfaces.

F_{st} is a friction force dived from the catalogue of the renowned manufacturer Parker [22]. This value takes into account two effects occurring on the actuator seals: The compression effect on the seal caused by the hydraulic pressure F_H and the compression effect on preload of the seals induced during installation F_c, both of them depending on seal type. Thus, the friction force is $F_{st} = F_H + F_c$. This expression produces different effects depending on whether the actuator (the valve) is pressurized or not [12].

From the mathematical relations given, the position and speed of the SCAS actuator can be determined. However, the generation of the external load remains to be further investigated.

2.4.1 External Load

Generally, the SCAS system can be approximated as not being subject to externally applied loads due to the particular kinematic mechanism that constitutes MRA. Furthermore, the linkage geometry is such that it provides only limited control to the SCAS and not full control of the main actuator stroke. This together with the many mechanical linkages in the MRA means that the external load applied to the SCAS is not high. However, an external load was considered in the developed model. It should be noted that is a simplification of the lever controls and external forces applied to the SCAS system. This topic could be further extended when integrating the SCAS model developed in this thesis work into an overall MRA model. Concerning the work developed in this thesis, the external load was considered as a system, with its own weight, moving in reaction to the movement of the actuator. It was considered a friction, a stiffness of the system k_{ld} thus a damping c_{ld}. The output is the position x_l and velocity $\dot{x}_l$ of the system in opposition to the movement of the actuator rod x, that also is the input (fig. 36).

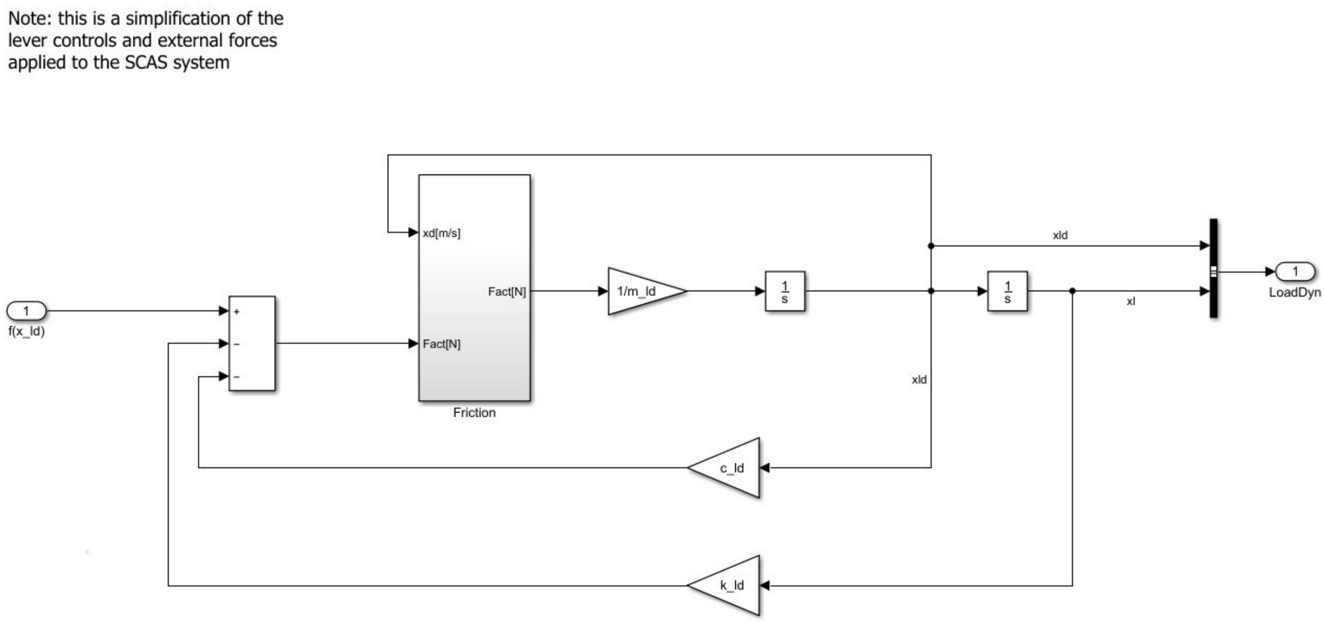

Figure 36: Load Dyn Simulink block

2.4.2 Simulink Model of SCAS Actuator

The SCAS actuator model is now shown.

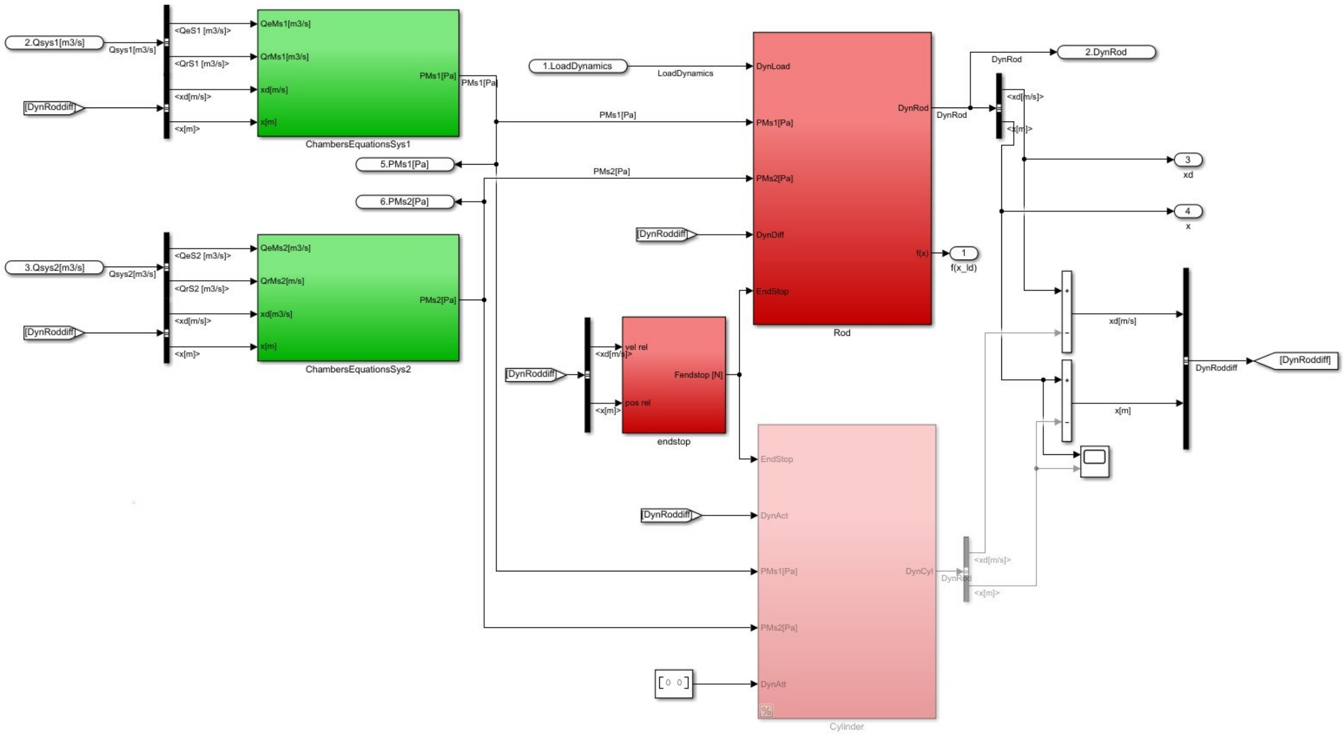

Figure 37: View inside the Simulink SCAS Main Actuator block

As mentioned before, the block representing the cylinder dynamics is deactivated because for a first approximation dimensioning, such as that inherent in the thesis work under consideration, the cylinder supports are considered with an infinite stiffness. However, a proposed modelling of cylinder dynamics is given (fig. 40).

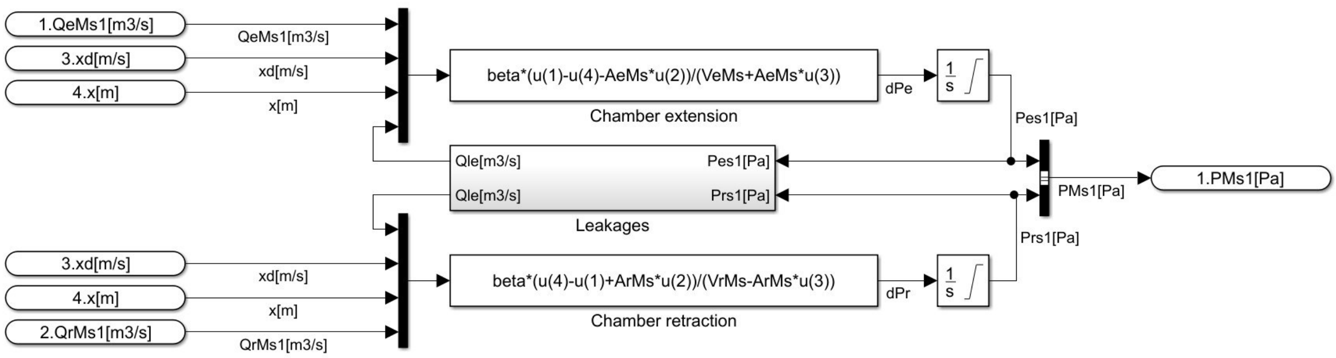

Figure 38: View inside ChambersEquationsSys block

The blocks in green are those related to solving the continuity equations and are feed with the flow rates of the jet-pipe and as retraction inputs the position and velocity of the actuator (fig. 38). The output is the pressures in the chambers that are sent in retraction to the model block of the hydraulic circuit and as input to the block that is used to calculate the dynamic equilibrium equations in the rod and cylinder.

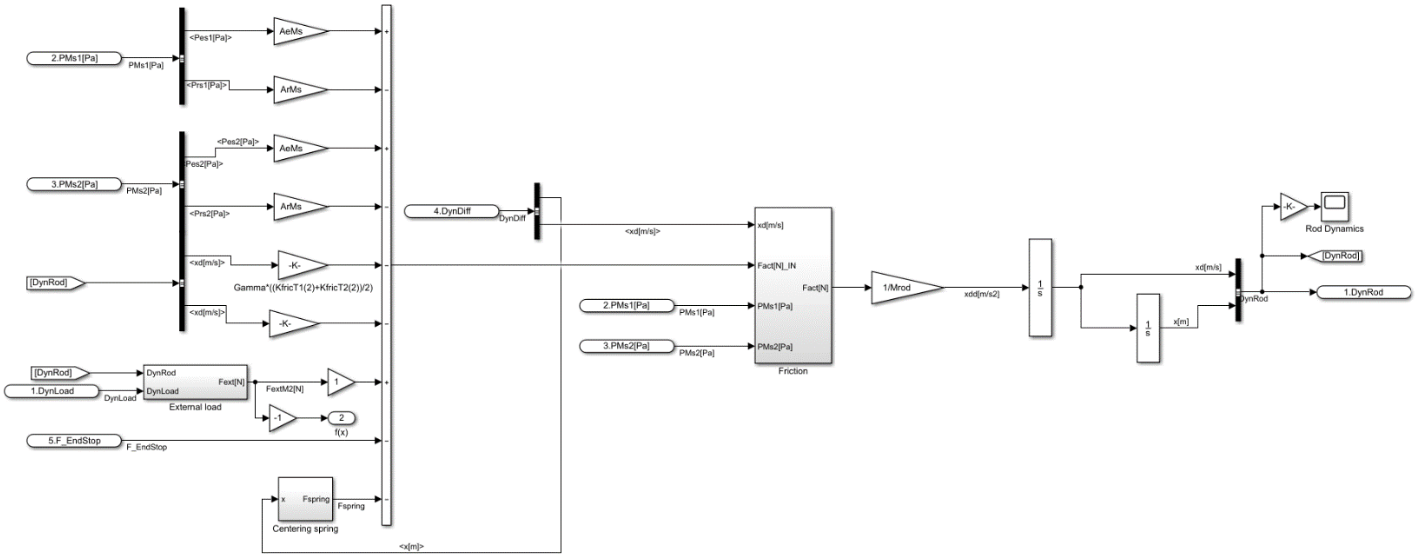

Figure 39: View inside Rod block

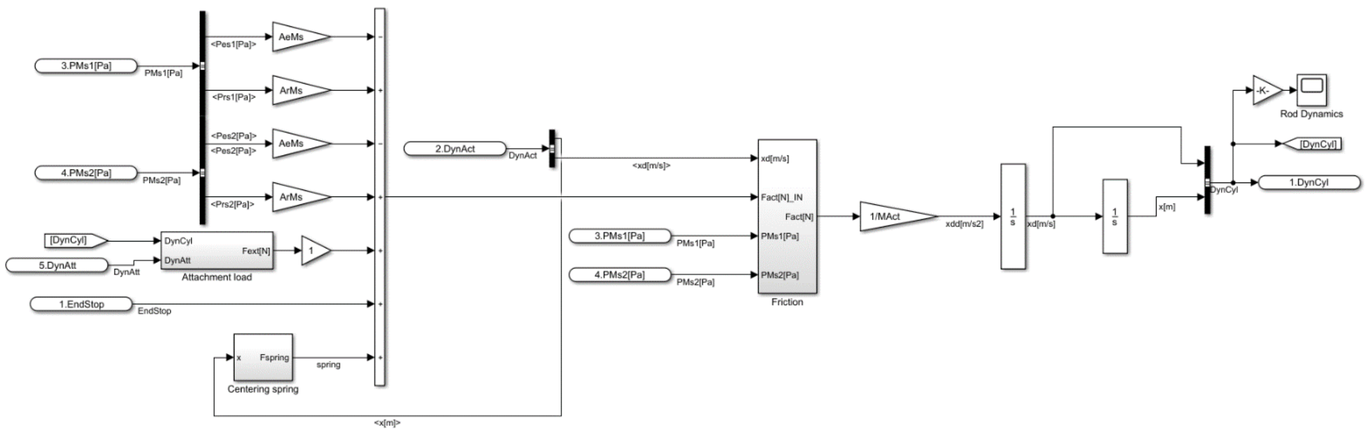

Figure 40: View inside Cylinder block

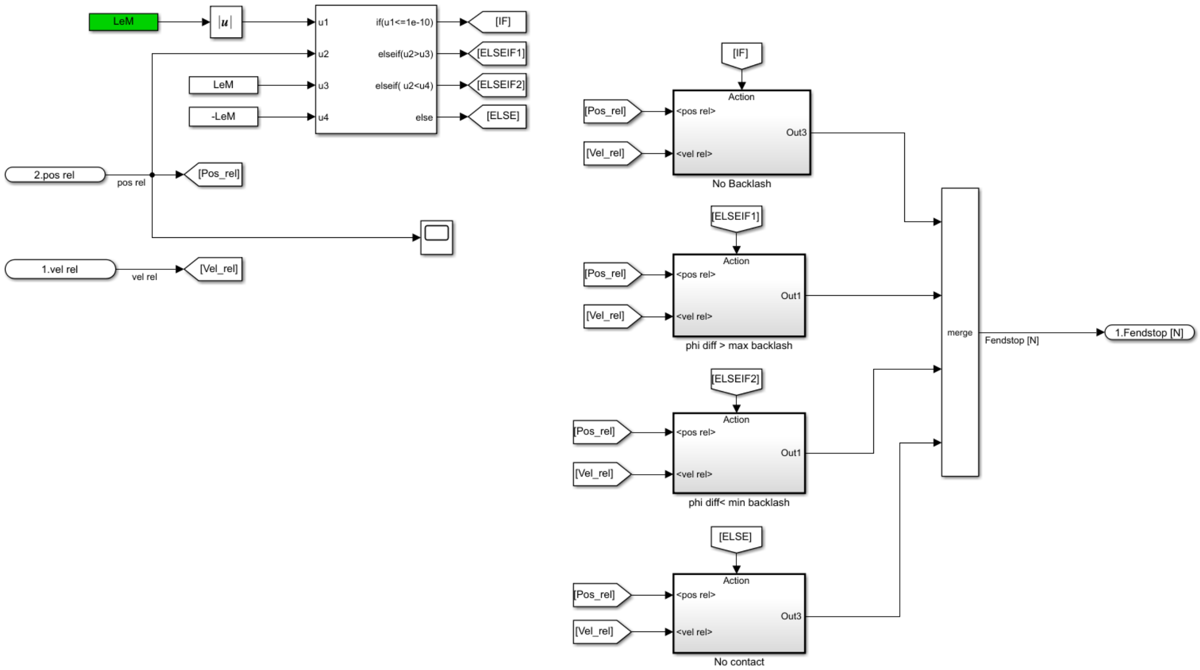

Figure 41: View inside Endstop block, in green LeM that is Endstop stroke, equal to half cylinder stroke increased by 5%

Figure 39 shows the model used to solve the equilibrium equations in the rod; these parameters needed a lot of testing and fitting during the dimensioning phase in order to reach the targets set in this thesis work. The displacement x of the SCAS system was thus determined; in the following section, an LVDT transducer to measure this displacement and a controller, will be introduced.

2.5 LVDT

The transducer used to detect the position is an LVDT type, Linear Variable Differential Transformers, that convert the mechanical movement of a reference system into an electrical output [24]. The operating principle is based on the concept of *mutual inductance.* It consists of a ferromagnetic core that can translate, as a result of this displacement LVDT changes the mutual inductance between the primary winding and the two secondary windings, producing an unbalance voltage output proportional to the translation (fig. 42).

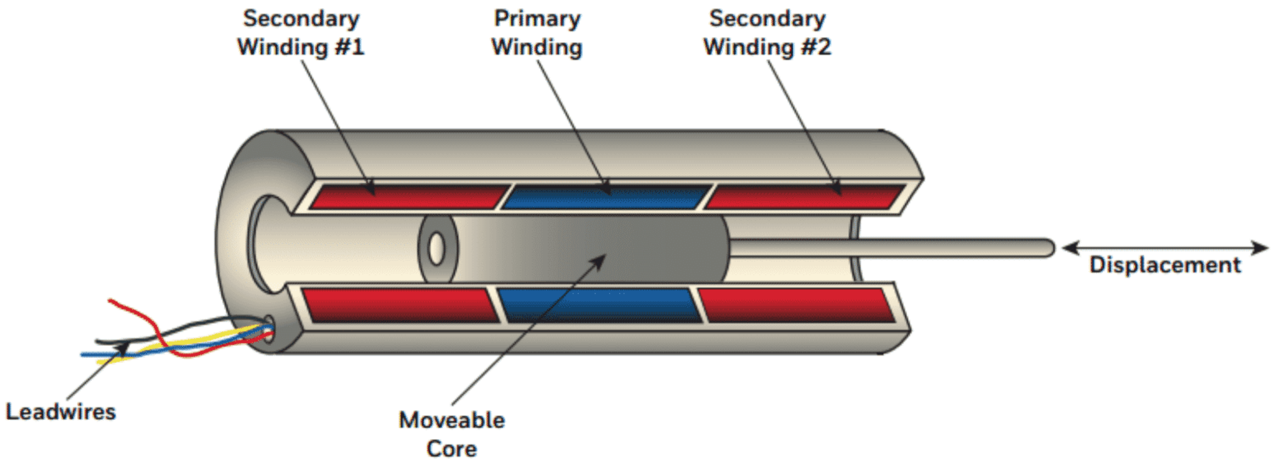

Figure 42: Cutaway view of an LVDT [25]

LVDT purpose is to generate a voltage feedback signal $V_{f/b}$ which can be directly compared with the set voltage signal V_{SET} thus generating the error signal V_e which will be compensated appropriately by the control logic. LVDT position sensor is modelled through the following second-order transfer function:

$$\frac{V_{f/b}}{G_{lv,fb}} = \frac{1}{\frac{s^2}{\sigma_{n,fb}^2} + s\frac{2\xi_{fb}}{\sigma_{n,fb}} + 1}$$

Where:

$G_{lv,fb}$ is static gain which have the same value of G_{SET} set gain.

$\sigma_{n,fb}$ is the transmitter natural frequency.

ξ_{fb} is the transmitter natural damping.

The Simulink model adopted is now reported (fig. 43).

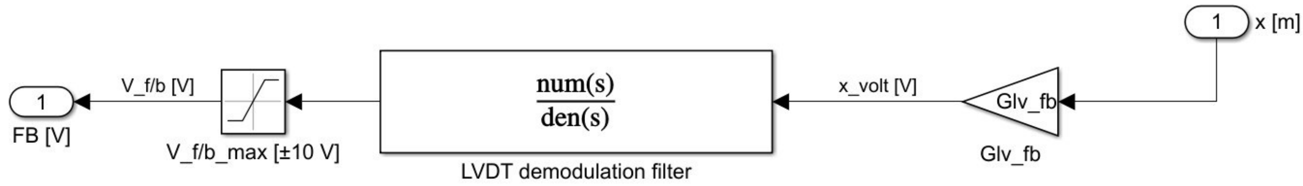

Figure 43: LVDT Simulink model

2.6 Controller

The control system adopted is of the *PID* type, where, however, only the proportional and integral *PI* part has been considered. Since, as explained before, the second stage has been removed and only the jet-pipe pilot stage is used, it does not have a mechanical feedback system, the control is fundamental. Moreover, the system without a controller, apart from having errors in response, would not be able to return to the zero position once the end stop is reached. The necessity to use the integrative component in the controller is explained by the need to avoid the presence of an excessive *steady-state error*. The need to have an integrative component in the controller derives from the fact that the transfer function of the system does not naturally have a pole in the origin. Due to the centering springs inside the SCAS actuator that does not guarantee its accuracy at steady state, so it is added via the integrative branch of PI controller. The value of the proportional *Kp* and integrative *Ki* gains were not known, so it was necessary to calibrate the PI. Furthermore, due to the complexity of the SCAS system, an explicit transfer function of the system is not known and, therefore, the use of an automatic controller calibration method was mandatory. The classical Ziegler-Nichols PID calibration method was used [26]. The transfer function that links the error tension to the tension reference voltages established at the terminals of the torque motor windings, which will then be converted into current, is thus defined:

$$G_c = K_p + \frac{K_i}{s} = \frac{K_i}{s}(\tau s + 1) \quad ; \quad \tau = \frac{K_p}{K_i}$$

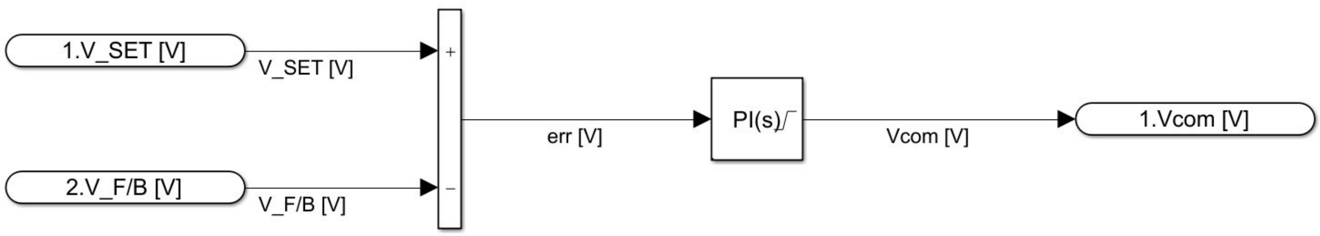

Figure 44: Simulink Controller model

In the Ziegler-Nichols closed-loop method, the following steps are performed [27]:

- The gains *Kp* and *Ki* are set to zero.
- Gradually increase the value of *Kp* until, for a small (step) perturbation of the input, there is a permanent oscillation of the output.
- Critical values K_{p0} and T_0 that bring the system into instability are recorded.
- The values of the gains according to the Ziegler-Nichols relation for PI are calculated:

$$\begin{cases} K_p = 0{,}45 K_{p0} \\ K_i = \dfrac{T_0}{1{,}2} \end{cases}$$

Diagrams were plotted to visualize what was achieved with the calibration (fig. 45). Overall, the response provided by the system can be considered satisfactory.

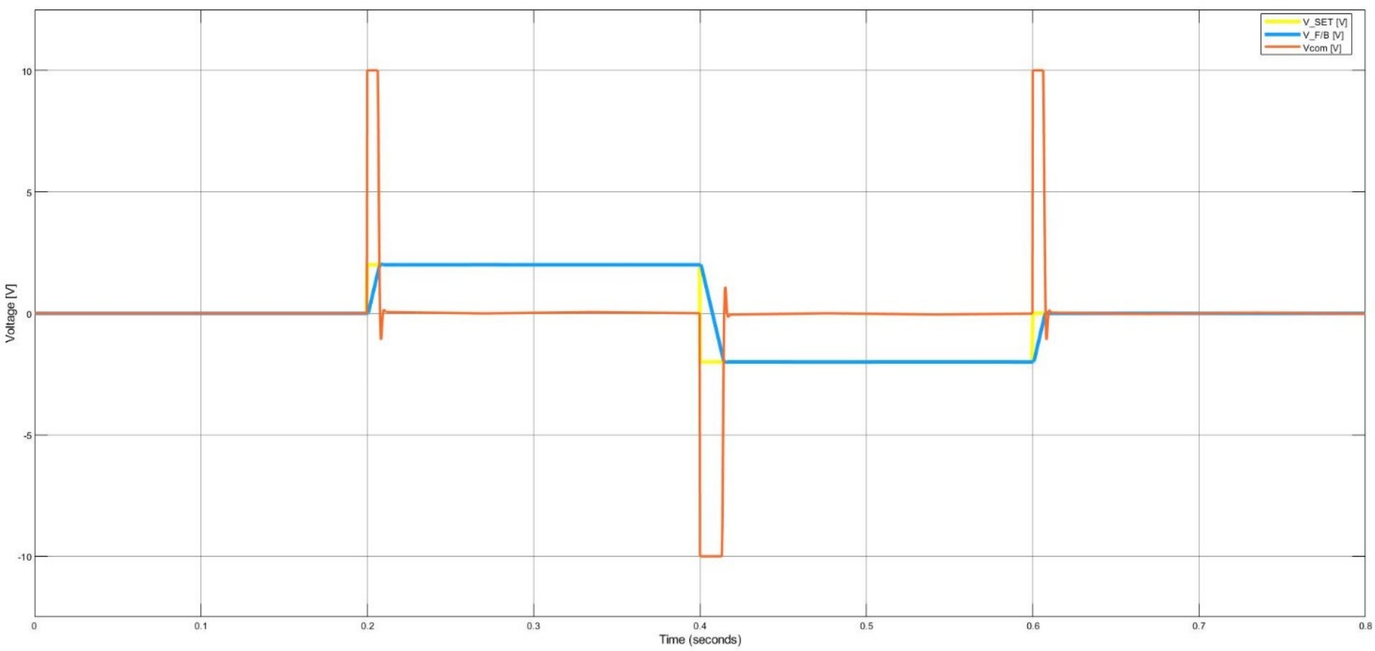

Figure 45: Example of SCAS operation with behaviour of voltages.

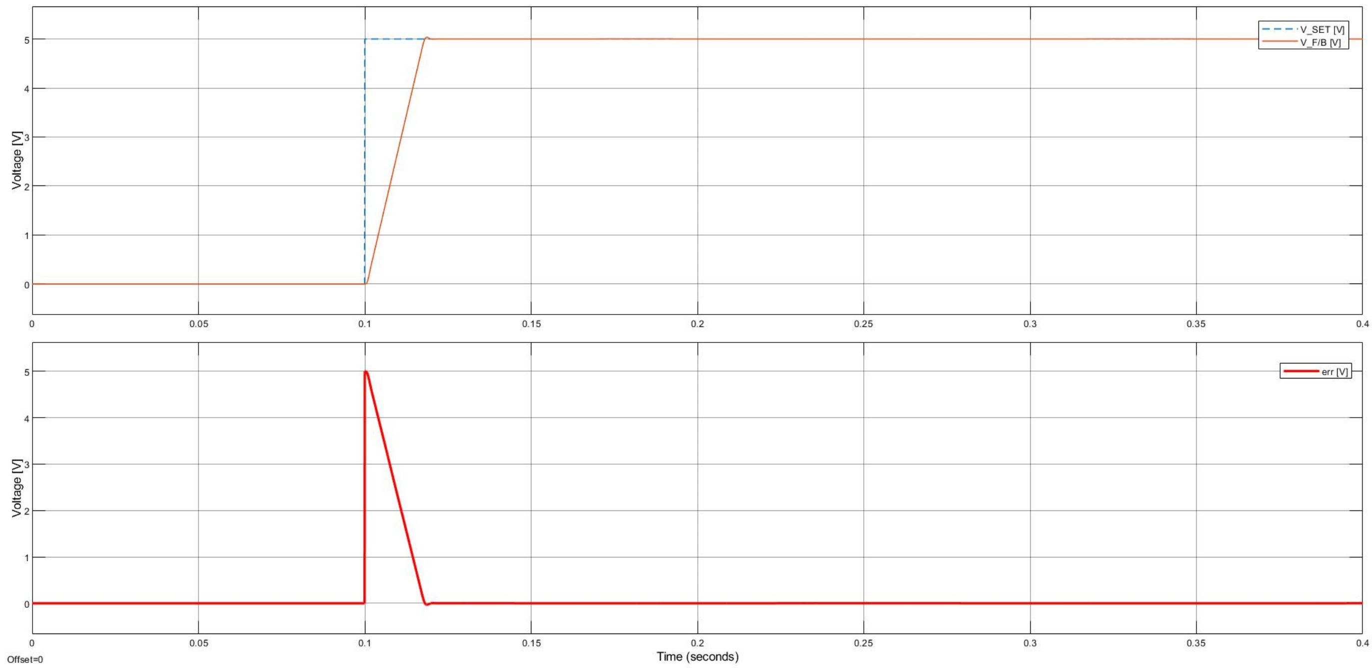

Figure 46: Voltages in SCAS step response, in red the error[V]

It should be underlined that controller calibration was only marginally covered in this thesis work, as the focus was more on modelling and dimensioning.

3. MODEL PERFORMANCE

The purpose of this chapter is to show all the tests that have been carried out in order to analyse the performance of the model. With this aim, trends, steady state responses and dynamic analyses will be illustrated subsequently. In addition, it should be again mentioned that all precise data will be shown in chapter four and that only those necessary for understanding the graphs and images presented will be displayed in this chapter. Just as a final note, it should be mentioned that in order to run the simulation, it was necessary to set fixed-step solver "*ode14x*" on Simulink with a step size of $1e^{-6}$.

3.1 Performance of the system

Results will now be presented to show how the system performs. Hence, it will show the trends of: current, jet-pipe position, flow rate and response of the complete system to various types of signals.

3.1.1 Rated current

The electrical circuit was tested at different voltage levels, starting from zero up to maximum voltage 10V (fig. 47).

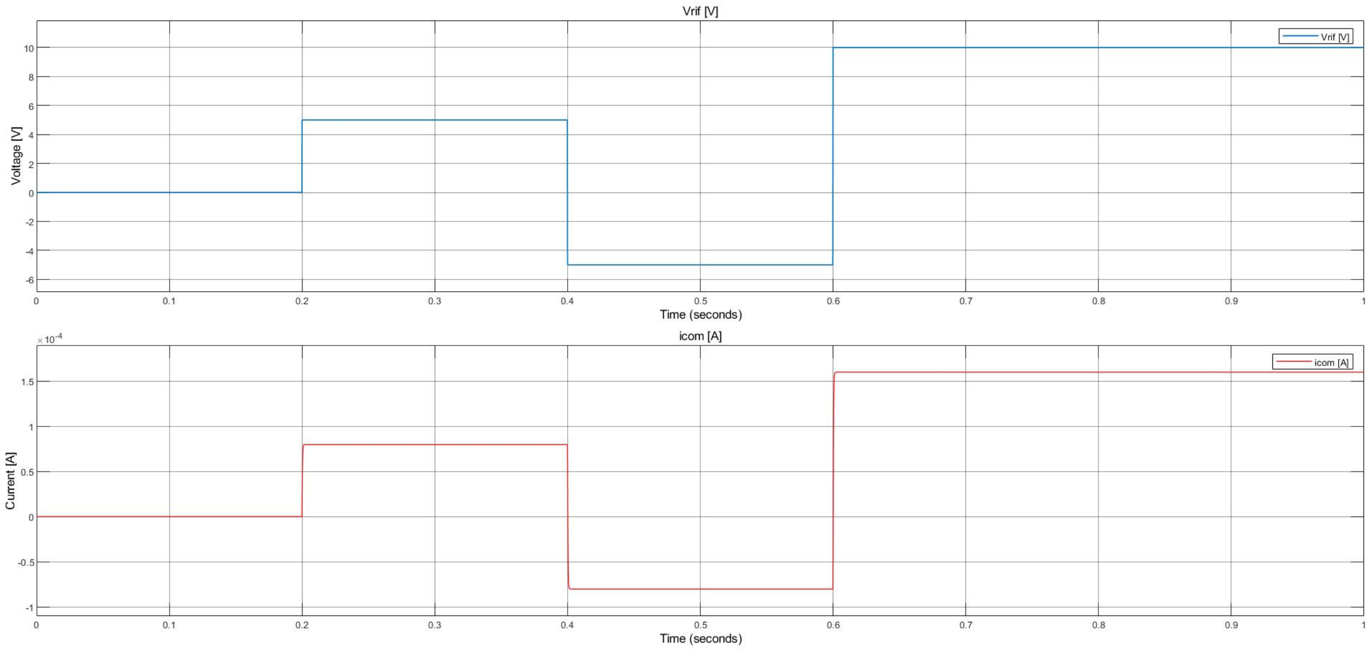

Figure 47: Trend of electric current in the windings (in red) at different voltage levels (in blue)

In the graph in figure 47, it can be seen that the rated current value of 8mA occurs at 5 V, while at the maximum voltage of 10 V, a current value of 16mA is obtained. In general, it can be stated that the model performs well and meets the expected targets.

3.1.2 Jet-pipe performance

In this section, graphs of the main parameters useful for understanding the performance of the Simulink model of the jet-pipe and its dimensioning will be plotted. The focus will be on torque delivered by the torque motor and x-displacement of the jet-pipe. Furthermore, the behavior of the flow passage areas will be investigated.

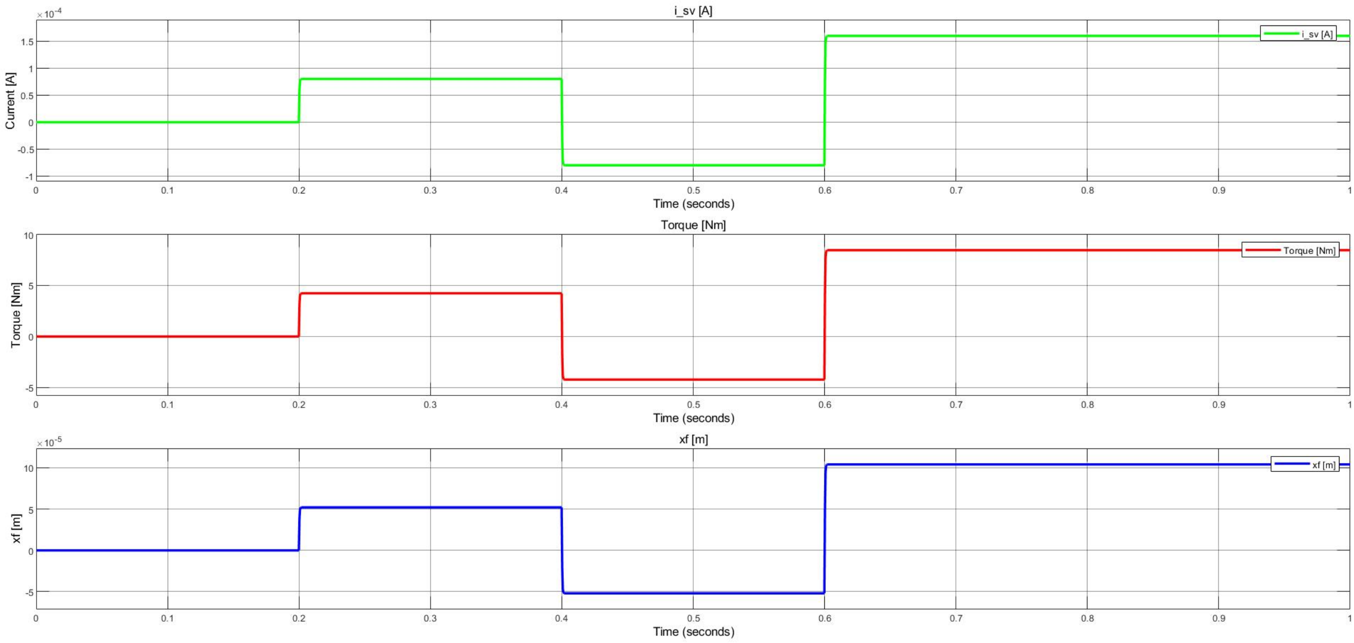

Figure 48: In green the pattern of the control current, in red the torque generated by the torque motor and in blue the trend of the displacement x of the jet-pipe

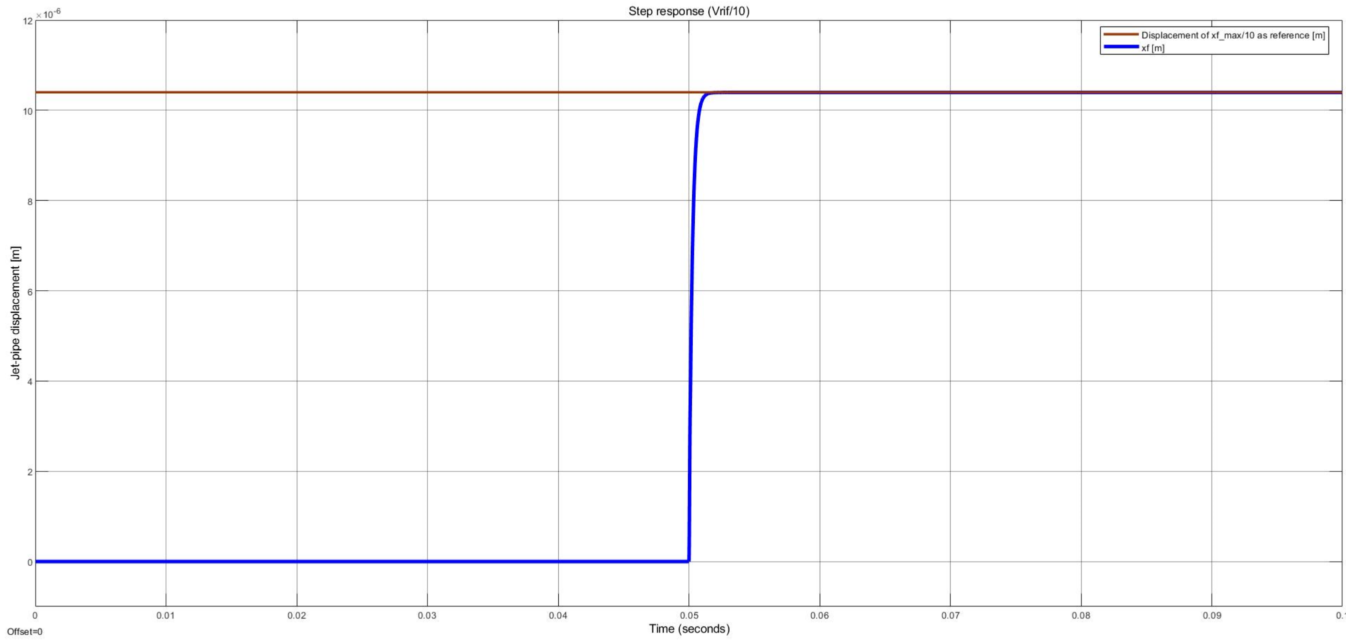

Figure 49: Displacement jet-pipe x step behaviour with a Vrif of 1V

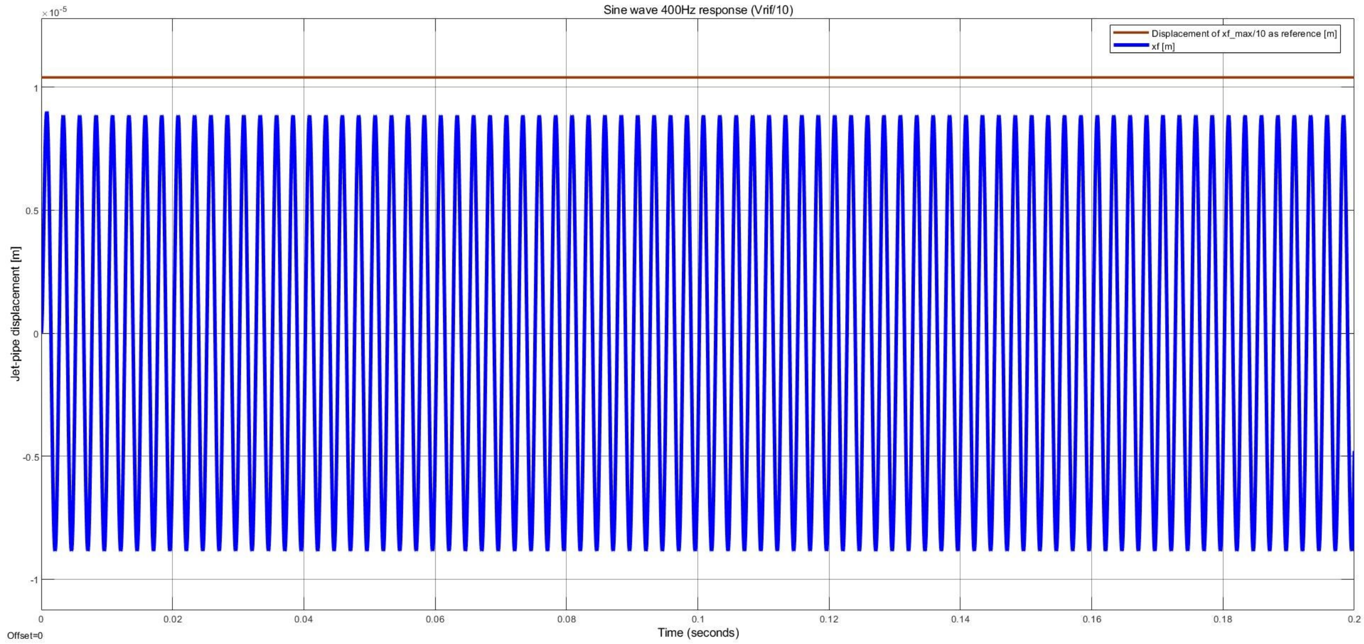

Figure 50: Displacement jet-pipe x sine wave behaviour at 400 Hz with a Vrif of 1V

With reference to figure 48, it can be seen that the torque supplied by the torque motor follows the course imposed by the current in the windings, the displacement x also follows the torque correctly. Maximum current $i_{sv\_Max} = 10\ mA$ corresponds to maximum torque $T_{max} = 8\ Nm$ which is followed by maximum displacement $x_{f\_Max} = 0{,}000104\ m$. In figure 49, the response of the jet-pipe displacement to a step signal imposed with a $V_{rif} = \frac{V_{rif\_MAX}}{10} = 1\ V$, at steady state there should therefore be a displacement equal to $x_{f\_Max} = \frac{x_{f\_Max}}{10} = 1.0400e^{-5}\ m$. Thereby, with reference to the graph (fig. 49) it can be stated that displacement x has a correct behaviour. Moreover, a sinusoidal command with a frequency of $400\ Hz$ and amplitude of $1\ V$ was set. Even in this case, performance is generally good, and attenuation is moderate, deviating only slightly from the target value. After evaluating how the jet-pipe displacement behaves at different input signals and its relationship to torque, the behaviour of the flow passage areas in relation to displacement x of jet-pipe is evaluated. Evaluating this point is very important because, as can be deduced, the flow rate to the SCAS actuator depends on the passage areas (fig. 26). The expected behaviour is for $x_f = 0$ have the jet-pipe centred on the two receiving holes, hence have equal areas. On the other hand, for a positive or negative x-displacement one of the two areas must increase while the other must decrease.

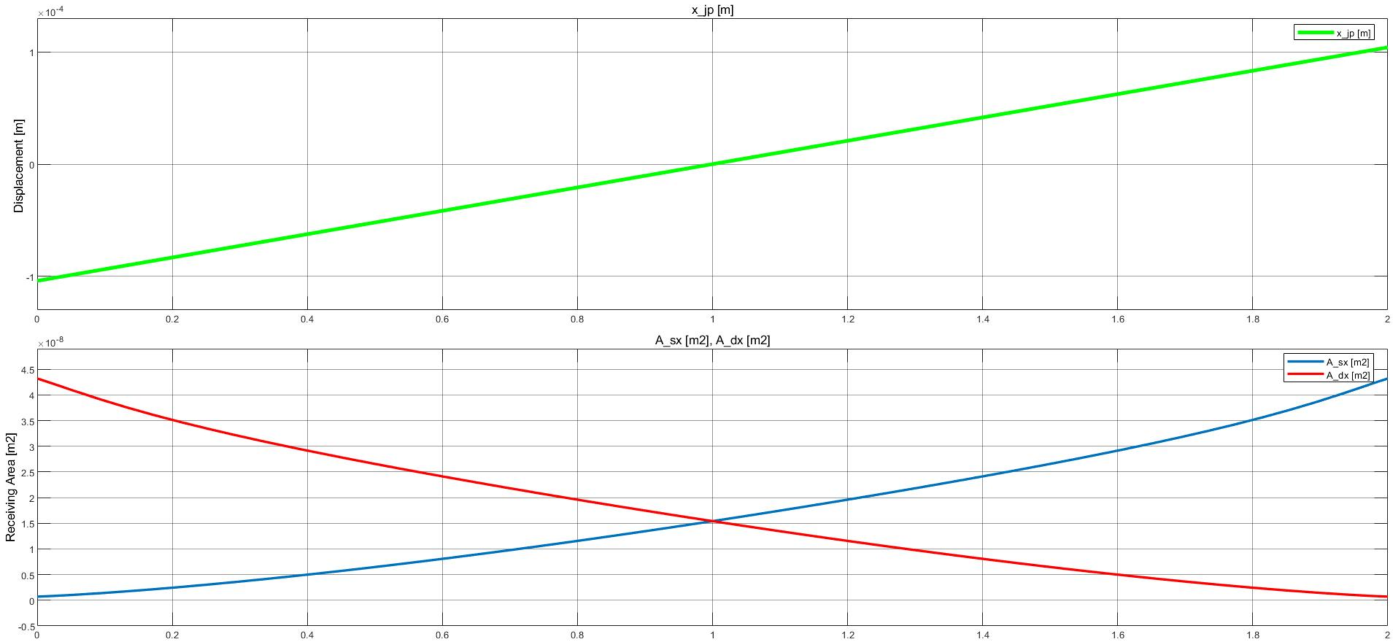

Figure 51: The curves of the receiving areas (bottom) versus the displacement of nozzle (on top)

The performance is in line with what is expected. This is also confirmed by the papers that can be found in the bibliography at references: [17][19][20]. Besides, it can be confirmed that the parameters used to dimension the model are appropriate, as the values are in line with what is found in the literature for servo valves of the type under investigation.

3.1.3 Flow rate

In this section, the flow rate trend under different conditions is presented. The graphs that will be illustrated represent the conclusion of the development of the model and its dimensioning. This section required the major effort during the thesis work. Indeed, if the system is not correctly set from a dimensional point of view, it becomes unstable and it is not possible to proceed with the simulation. Since most of the data was not known in advance, as well as the actuator present downstream of the hydraulic system that was modelled later, it was not defined, meant that numerous tests were necessary. Now, let proceed with the validation of the flow pressure characteristic described at the beginning of chapter 2.

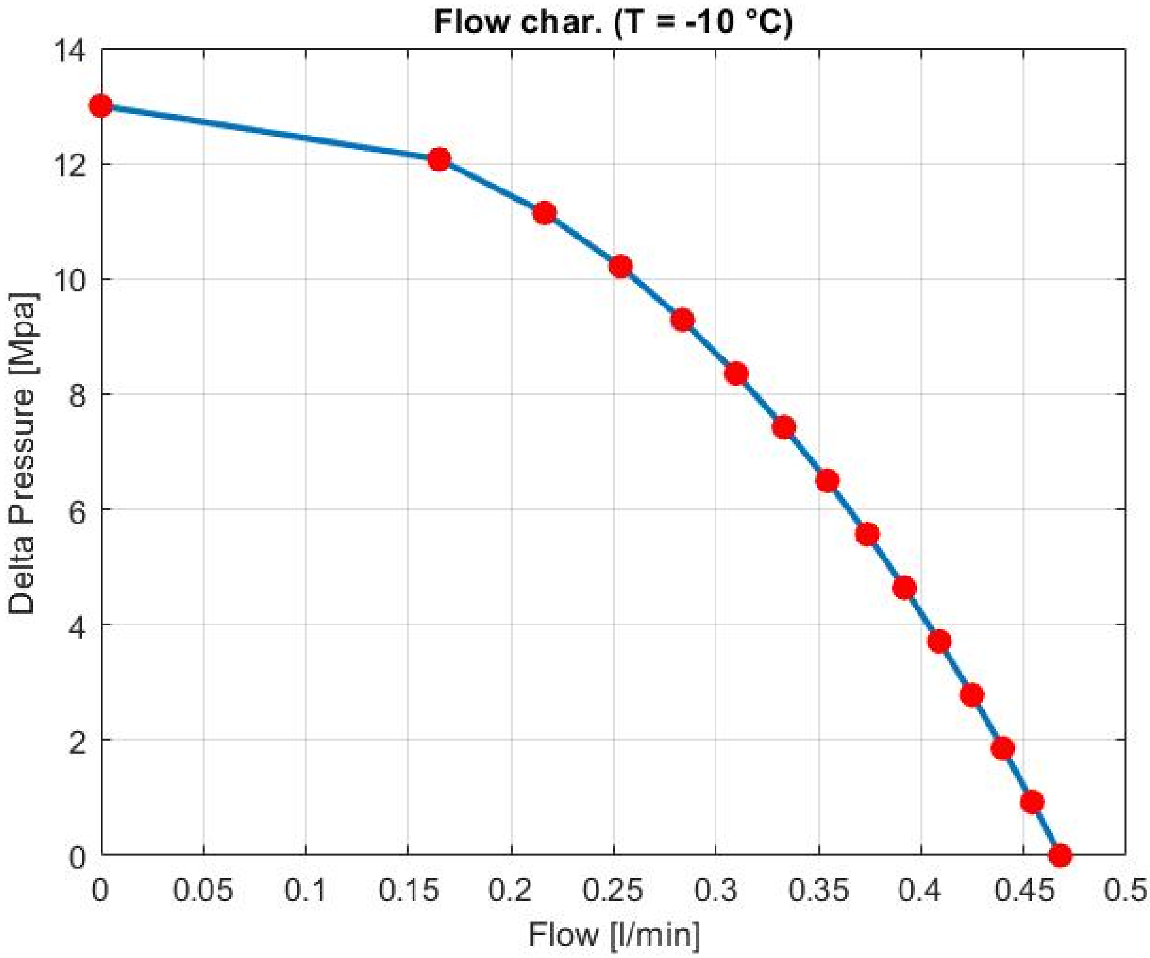

Figure 52:Model Flow-Pressure characteristic for supply pressure 17Mpa and temperature of -10°C

The plotted characteristic by checking the flow rate at different pressure deltas with a set temperature of -10 °C approximates well what is described in the input data of the thesis work. The next plot (fig. 54) shows the performance of the flow rate delivered by the jet-pipe as the temperature changes, maintaining a constant pressure delta.

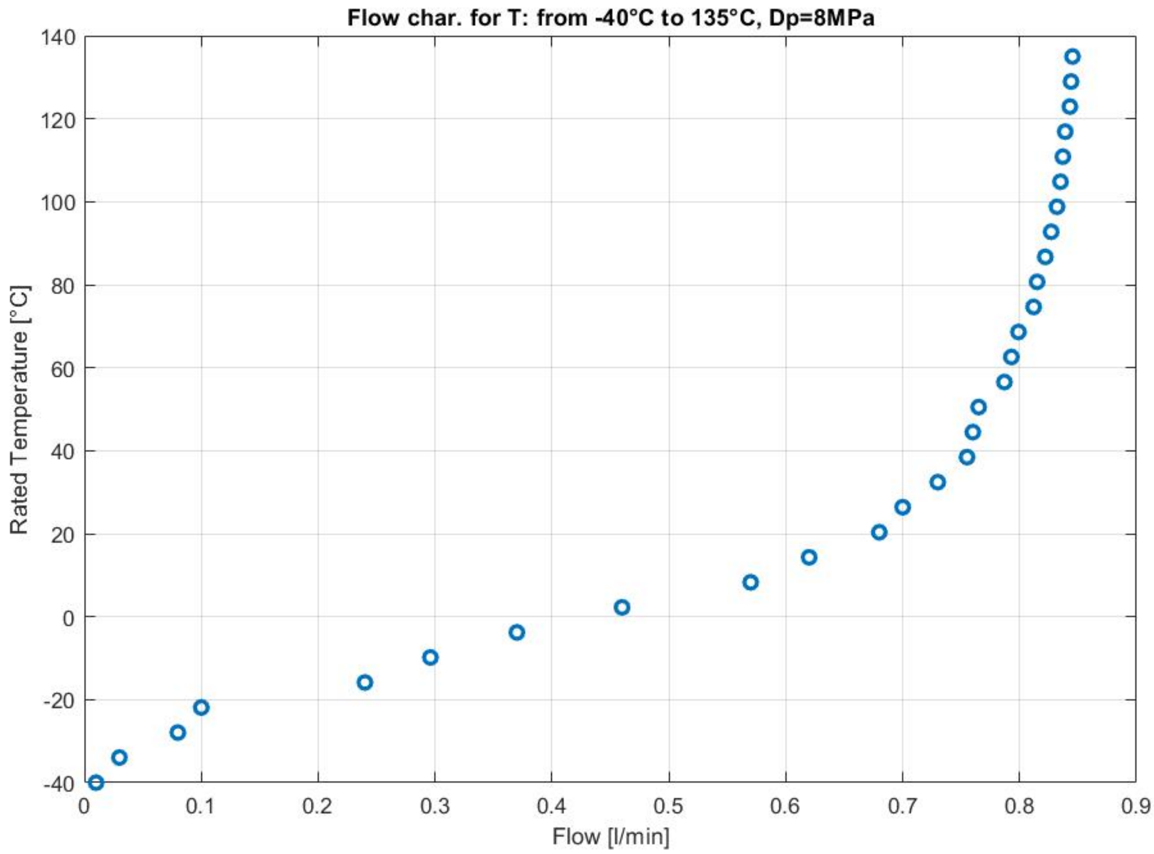

Figure 53: Change in flow rate as temperature changes

As expected, the flow rate increases with increasing temperature and the behaviour and rated value are in accordance with the scientific literature previously mentioned. However, it should not be underestimated that the flow rate delivered depends mainly on the pressure delta between the pressure supplied and the pressure downstream of the jet-pipe. At the same time, the pressure downstream of the jet-pipe depends on the pressures in the actuator chambers. Hence, the flow rate to the chambers will also depend on the condition of the SCAS actuator. After describing the flow rate and its dimensional values, it is now useful to focus on the performance of the whole system.

3.1.4 System response

In this paragraph, the performance of the system at various SET signals will be illustrated. The procedure used involves setting an x_{SET} and then monitoring how the system responds. The signals analysed will be of three types, step signal, trapezoidal signal and sinusoidal signal. For each of the three tests, two plots will be shown, one comparing the x output of the SCAS actuator with the x_{SET} and the other showing the trend of the main system parameters. Please note that the system under consideration has double jet-pipe in parallel. The key input parameters of the tests are:

- Supply Pressure: $17\ MPa$
- Return Pressure: $0{,}3\ MPa$
- Temperature: $20\ °C$
- Operating fluid: MIL-PRF-83282
- Simulation time: $1\ s$
- Step signal x_{SET}: $1{,}5\ mm$
- Trapezoidal signal x_{SET}: $-2\ mm$
- Sinusoidal signal x_{SET}: $0{,}5\ mm\ (f = 50\ Hz)$

Step Signal

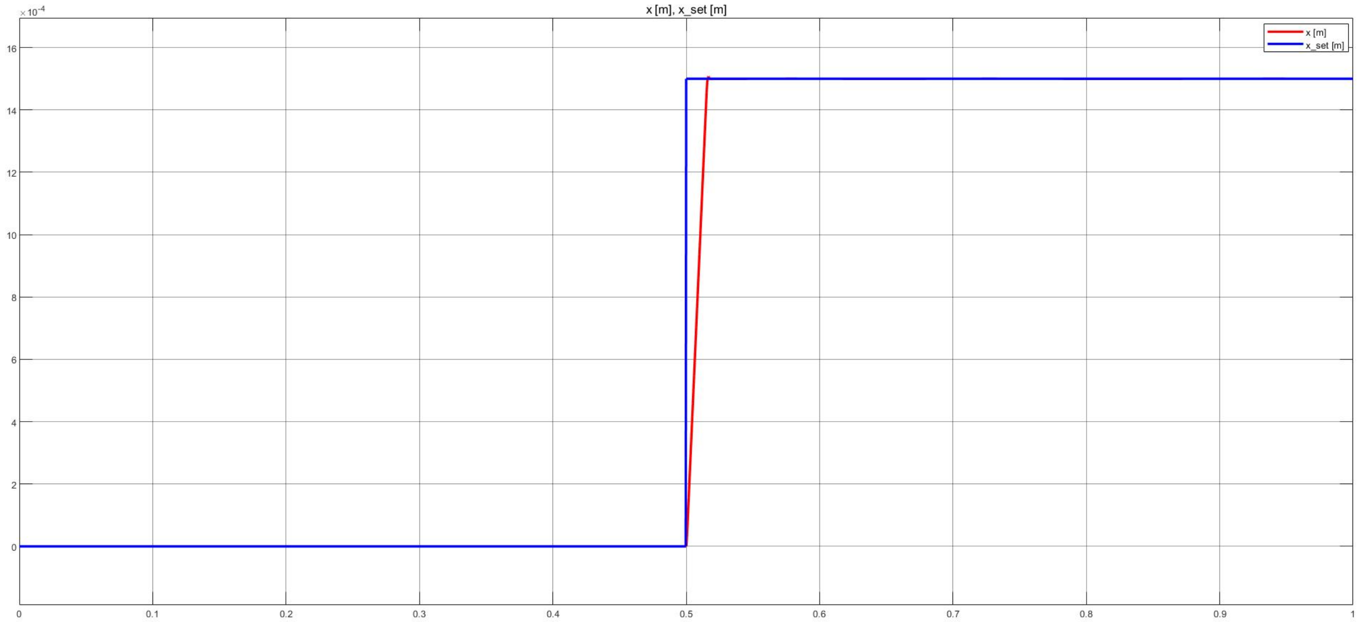

Figure 54: Displacement x [m] of SCAS Actuator with step signal

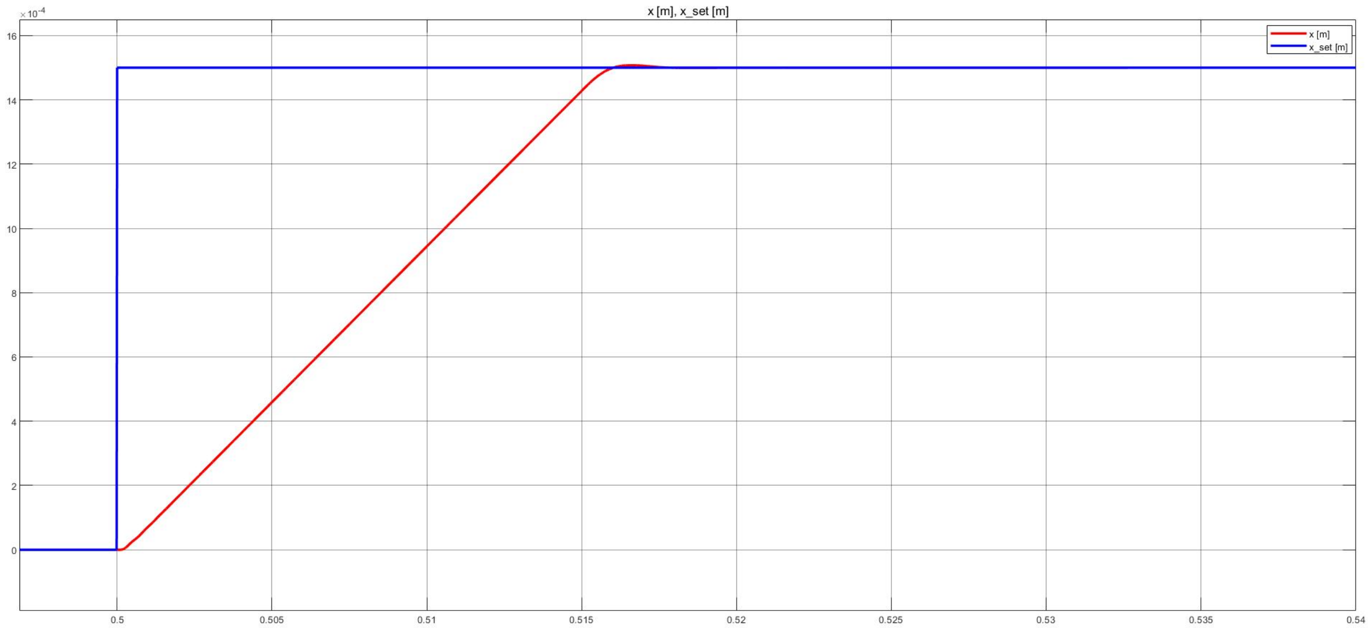

Figure 55: Settling time with step signal

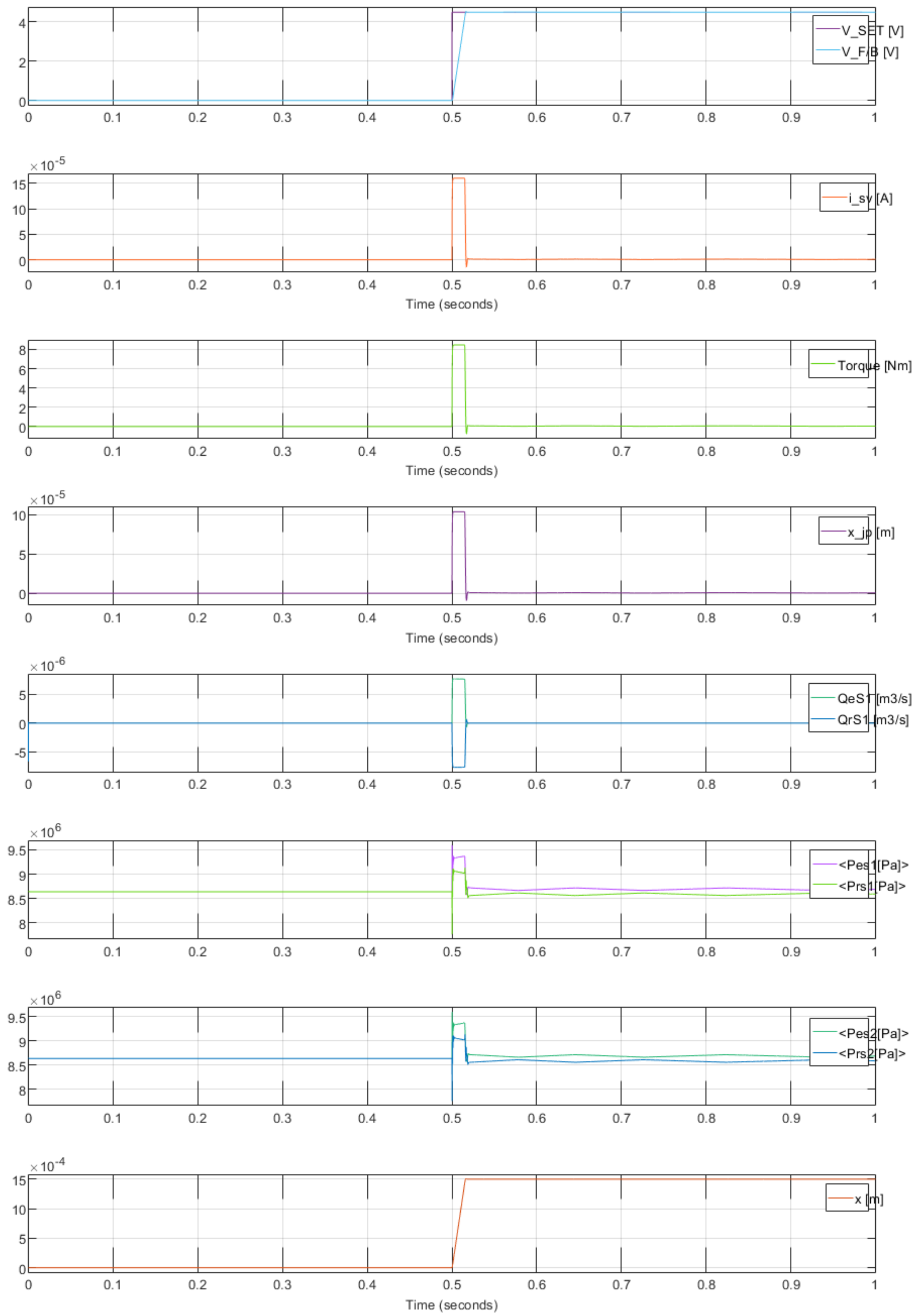

Figure 56: SCAS dashboard with step signal

As can be seen in figure 55 by applying a step signal the system results in a very slight overshoot. A good system is defined as one that is capable of responding to a step input with an overshoot of approximately 10%. From this point of view, the system does not perform particularly well. The root cause is probably to be found in a calibration of the PI controller that is not particularly effective. As explained previously, the accurate calibration of the controller is not the focus of this thesis, instead the modelling and operation of the system is the main argument. Keeping this concept in mind, it can be said that the result is acceptable. Carrying on with the analysis, as expected due to the structure of the system, the positional error at steady state is zero. Again, this is a positive performance.

Trapezoidal Signal

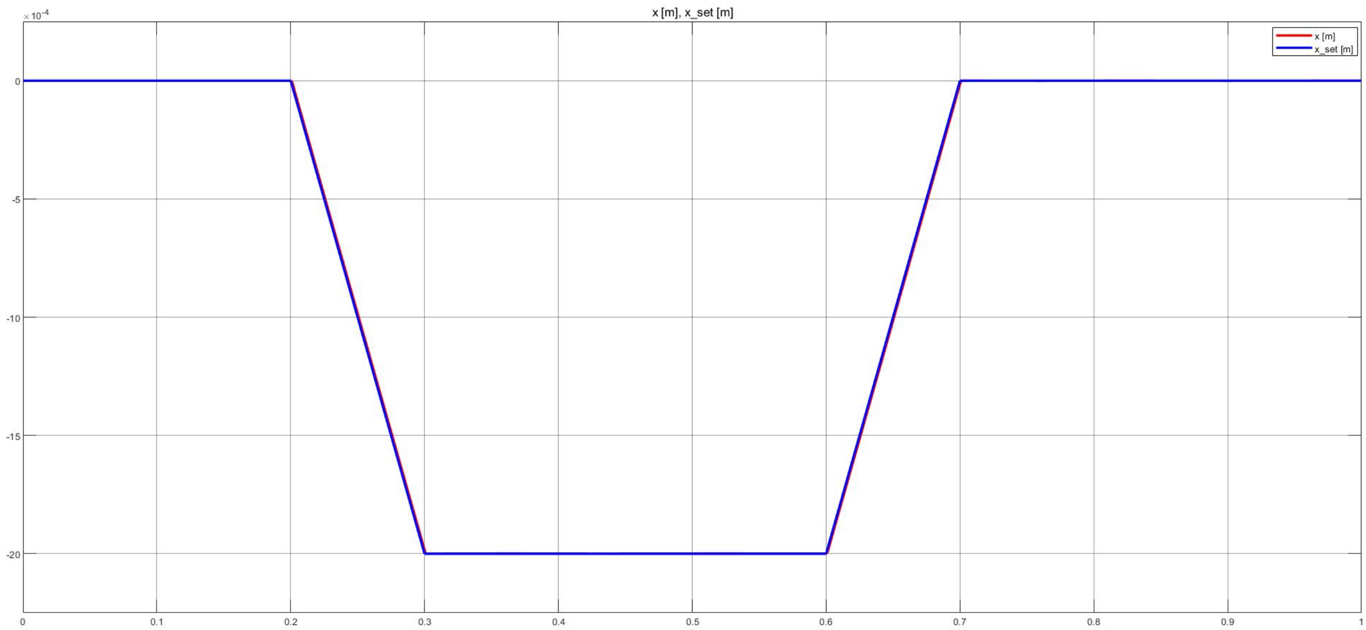

Figure 57: Displacement x [m] of SCAS Actuator with trapezoidal signal

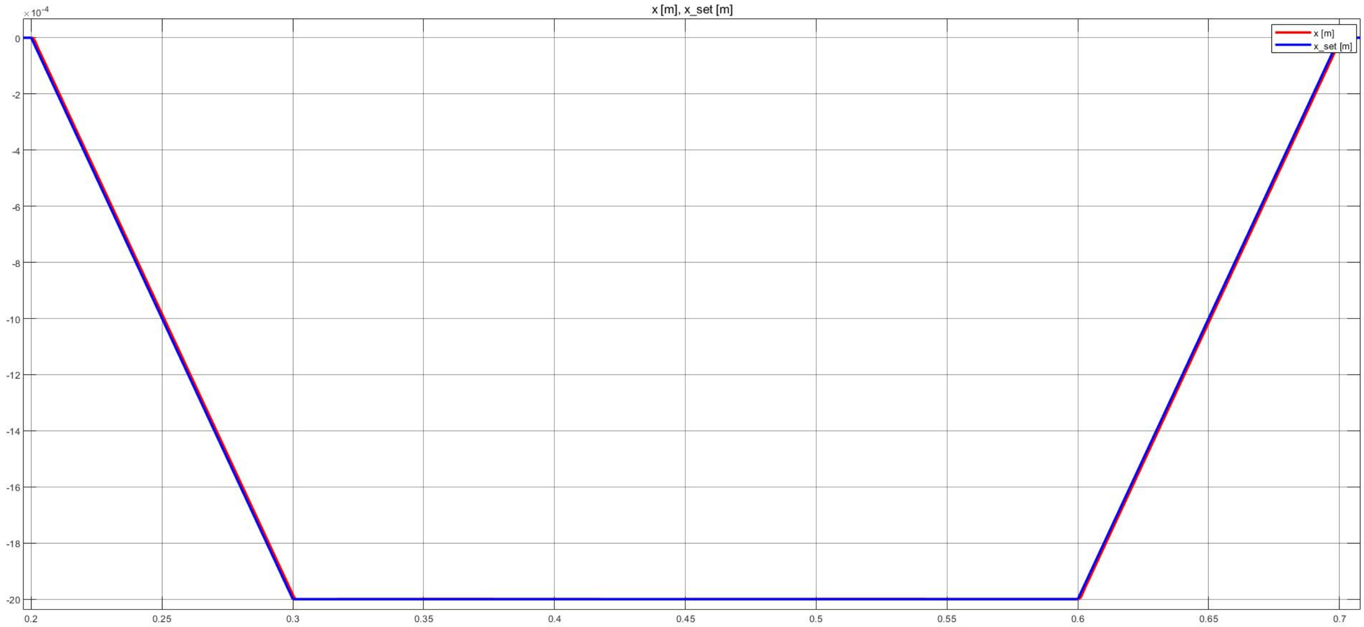

Figure 58: Zoom on two ramps

As can be seen in figure 58, there is a time lag of $0{,}8\ ms$ between the set and the position of the SCAS actuator. The steady-state error is also zero in this case. The dimensional values of all other system quantities, as shown in figure 59, are also consistent in both trend and dimensional values with what is expected. It can be stated that the performance of the system is acceptable.

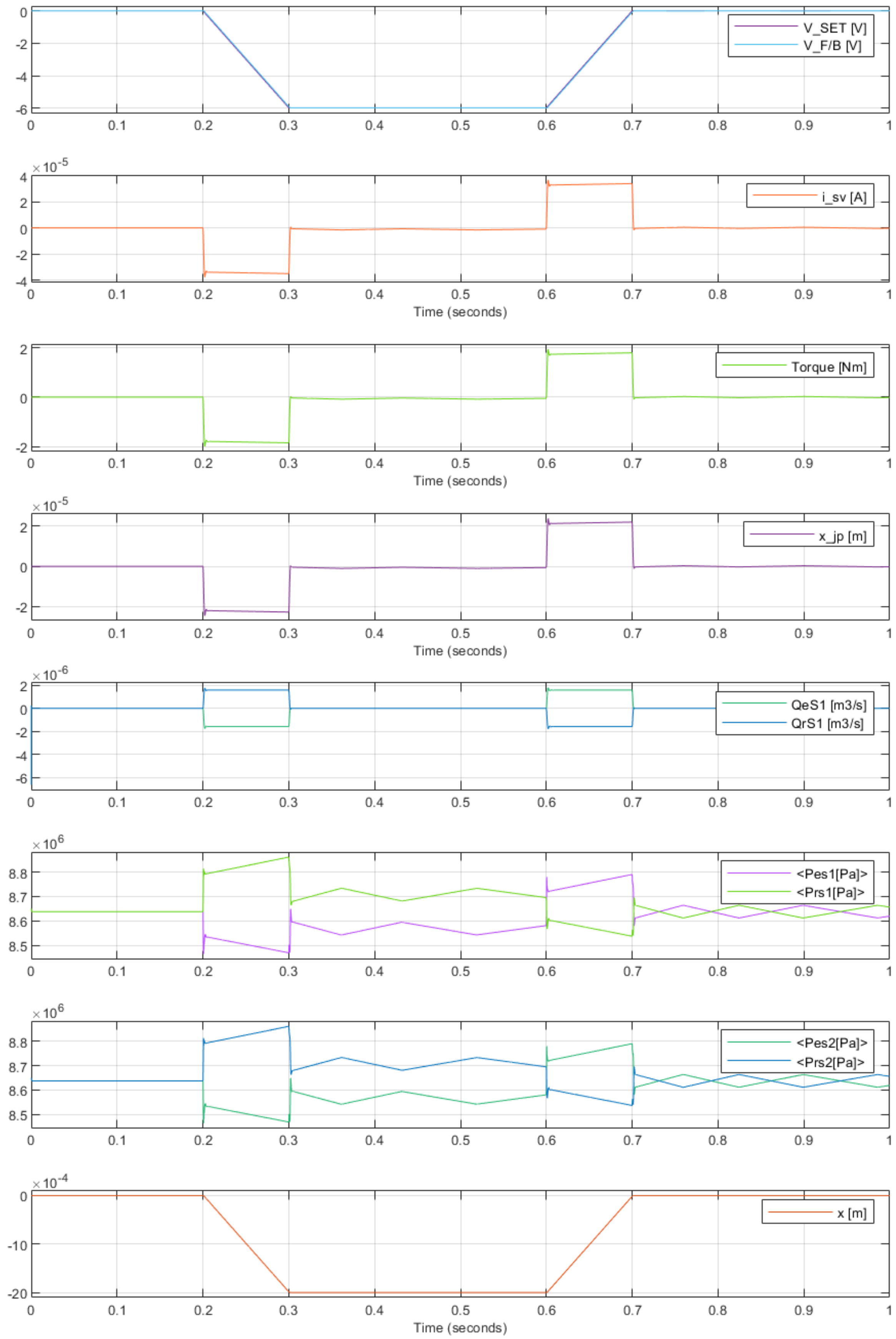

Figure 59: SCAS dashboard with trapezoidal signal

Sinusoidal Signal

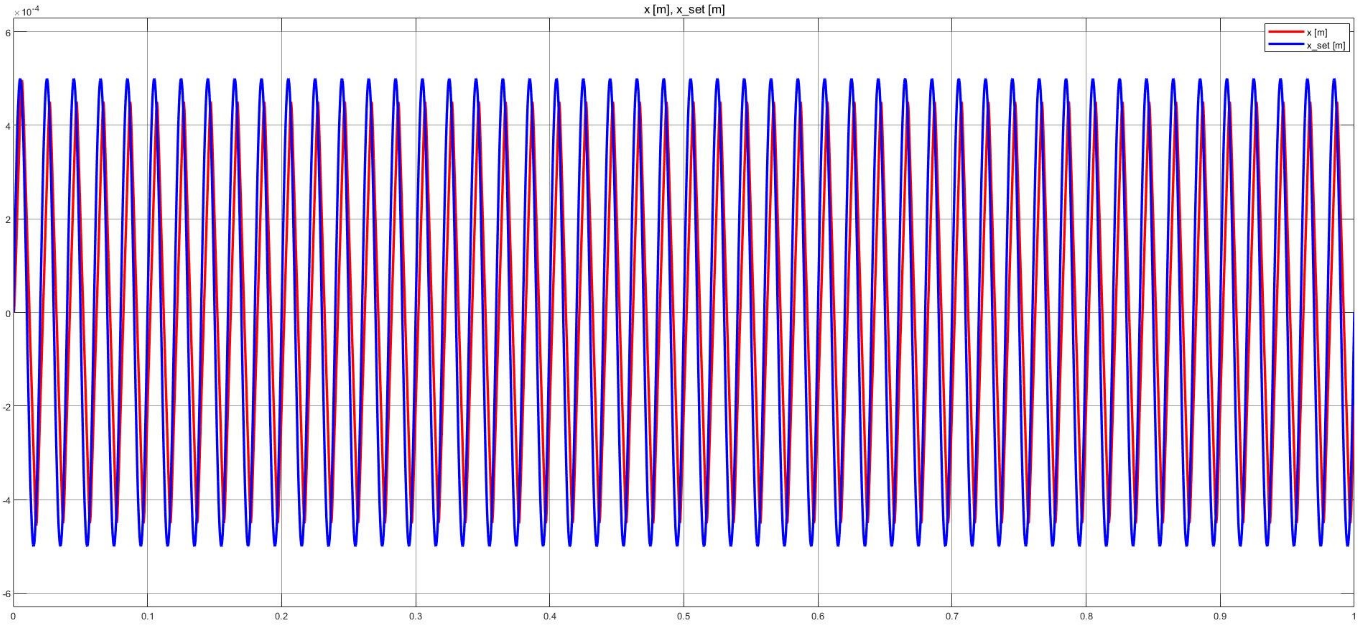

Figure 60: Displacement x [m] of SCAS Actuator with sinusoidal signal

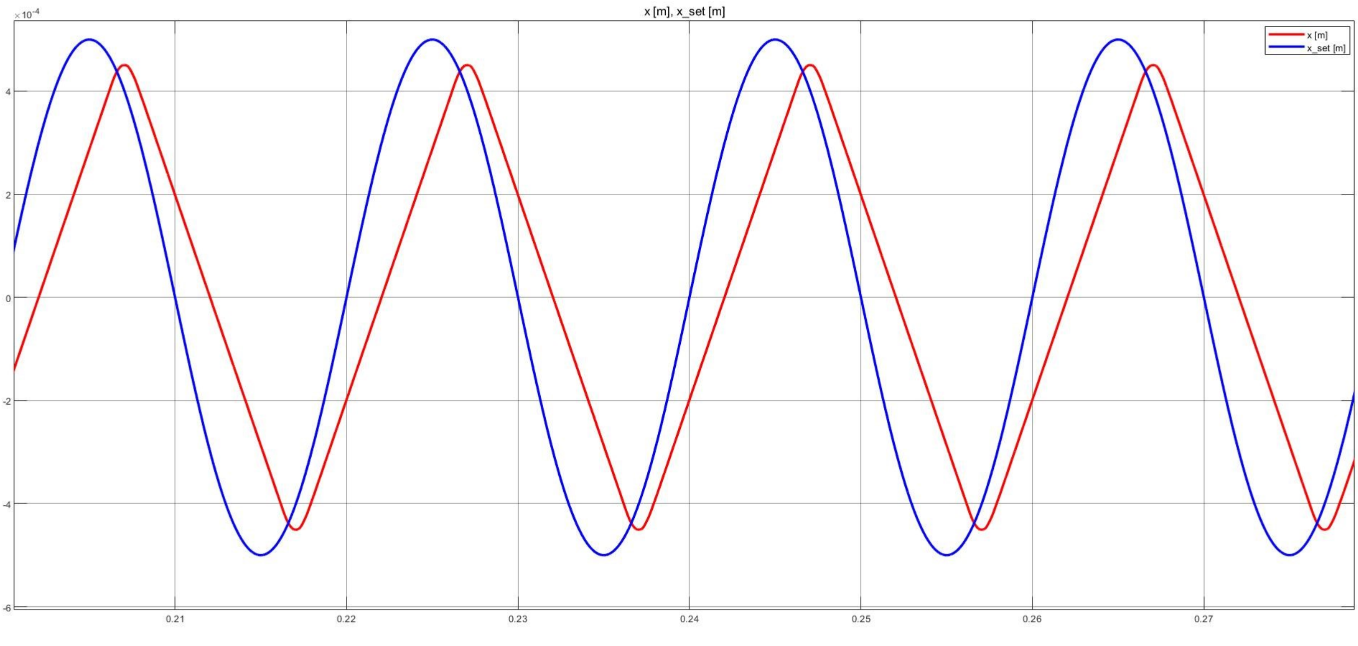

Figure 61: Zoom on displacement x [m] of SCAS Actuator with sinusoidal signal

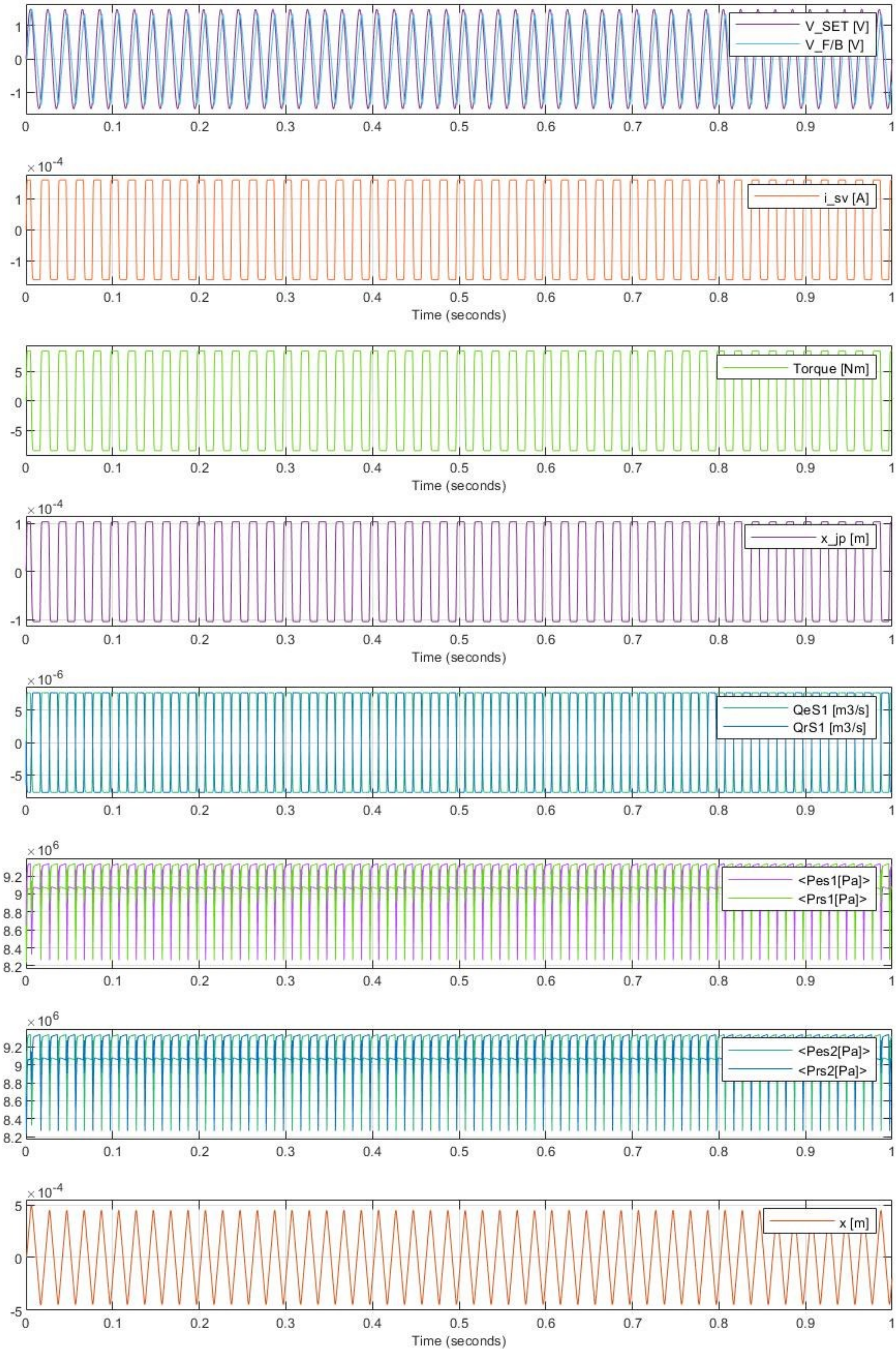

Figure 62: SCAS dashboard with sinusoidal signal

Generally, position-controlled servos are characterised by a maximum bandwidth of approximately 5 Hz. For SCAS servos, this limit is inconsistent. In fact, such systems are characterised by a very short stroke and distinct compactness. Precisely because the system under investigation has the greatest focus on compactness, it was chosen to test the system at $50\ Hz$. As shown in figure 61, As shown in figure 61, the system has an attenuation of $0,05\ mm$ compared to the set of $0,5\ mm$, so about 10%. The time delay is 2 ms. Further explanations will be provided in the next paragraph.

3.2 Frequency response

The results of the system response analysis in the frequency domain are now presented. The *Bode diagram* will be used, which, in steady state, provides the amplitude and phase of the system's response to a sinusoidal signal. It will be important so determine the system's *cut-off frequency* ω_t, defined as the frequency at which the amplitude of the system is equal to $-3\ dB$. Since for this type of servosystems under consideration in this thesis work, the system's steady-state accuracy is crucial, then the system's *bandwidth* can be considered equal to its cut-off frequency. Another key feature that will be investigated is *stability*. In general, a system is stable when a limited input corresponds to a limited output. In the case of *closed-loop* systems, such as the SCAS system, it is defined as stable if the argument of the *open-loop* transfer function calculated at the critical pulse ω_c is greater than $-180°$. The critical pulse ω_c, is defined as the pulsation where the module of open-loop transfer function is equals to one, hence: $|G_{ol}(j\omega_c)| = 1 \leftrightarrow |G_{ol}(j\omega_c)|_{dB} = 0$, usually $|G_{cl}(j\omega_c)| \cong 1$, so $\omega_t \neq \omega_c$. The concept of *critical phase* ϕ_c, defined as the argument of the open-loop transfer function at the critical pulse, must now be introduced. When $\phi_c > -180°$ the system is stable, conversely, if $\phi_c \leq -180°$ the system is unstable. Although, it is often not possible in real systems to achieve such a clear-cut distinction. Therefore, safety coefficients are introduced with respect to instability defined as *gain margin* G_m and *phase margin* ϕ_m. The first coefficient is defined as the distance between the module of the transfer function in open loop and the modulus at a phase of $-180°$, is measured in dB. The second parameter is defined as $\phi_m = 180° - |\phi_c|$. The system increases its *robustness* the more these two parameters increase. Typical values for servo systems are [8]:

$$\begin{cases} \phi_m > 60° \\ G_m > 7 \div 8\ dB \end{cases}$$

The discussion will be divided into two parts, with tested frequencies ranging from 1 to $1000\ Hz$. In the first part, the results of the test performed on the jet-pipe dynamics will be presented. In the second part, the frequency response of the system will be shown, in closed and open loop, by changing the voltage signal and operating temperature.

3.2.1 Jet-pipe frequency response

In this section, results are shown to demonstrate the input data presented at the beginning of chapter 2: the frequency response of the jet-pipe displacement respect to rated current must have amplitude ratio greater than -3 dB and phase lag lower than 90° for frequencies lower than 400 Hz (fig. 63). Subsequently, considering that the maximum x jet-pipe displacement is $0{,}1\ mm$, further tests were performed by comparing an input x with the output x as shown in the table:

Voltage SET	**Input x SET corresponding**
$2\ V$	$0{,}02\ mm$
$4\ V$	$0{,}041\ mm$
$6\ V$	$0{,}062\ mm$
$8\ V$	$0{,}083\ mm$

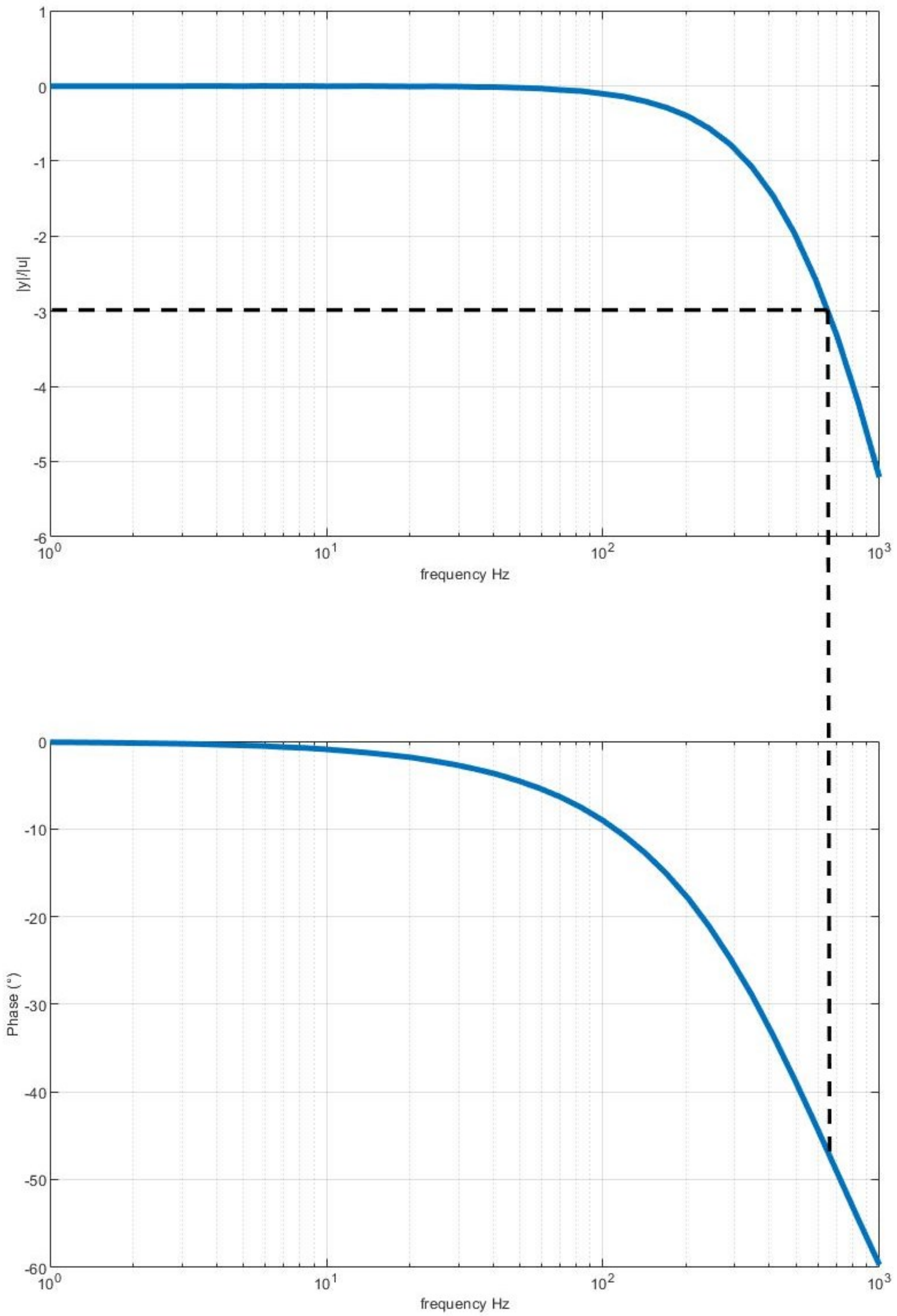

Figure 63: Bode diagram of Jet-pipe dynamics, input x is 0.12 mm, equal to that measured with a rated current of 8 mA

All the tests carried out have given very similar results and so are not reported, as they would not provide any further useful information. From observation of figure 63, it can be said that the required input condition is fulfilled. It is therefore concluded that the first-stage jet-pipe system has plausible dynamics.

3.2.2 System frequency response

Several tests were performed to evaluate the system's frequency response performance. The Bode diagrams that will be shown were obtained from tests as listed below:

- $P_s: 17MPa$, $T: 20°C$, $V_{SET}: 5V$
- $P_s: 17MPa$, $T: 20°C$, $V_{SET}: 2V/6V/8V$
- $P_s: 17MPa$, $T: -40°C/-10°C/5°C/50°C/\ 80°C/130°C$, $V_{SET}: 5V$
- $P_s: 17MPa/20MPa$, $T: 20°C$, $V_{SET}: 5V$

Let now proceed with the presentation of open-loop and closed-loop frequency Bode diagrams. As written in the chapter on the controller, in this system is used a PI type controller that as a general behavior provides a phase recovery. Perhaps, since is not a main argument of this thesis work, a fine-tuning of the adopted controller parameters is then recommended.

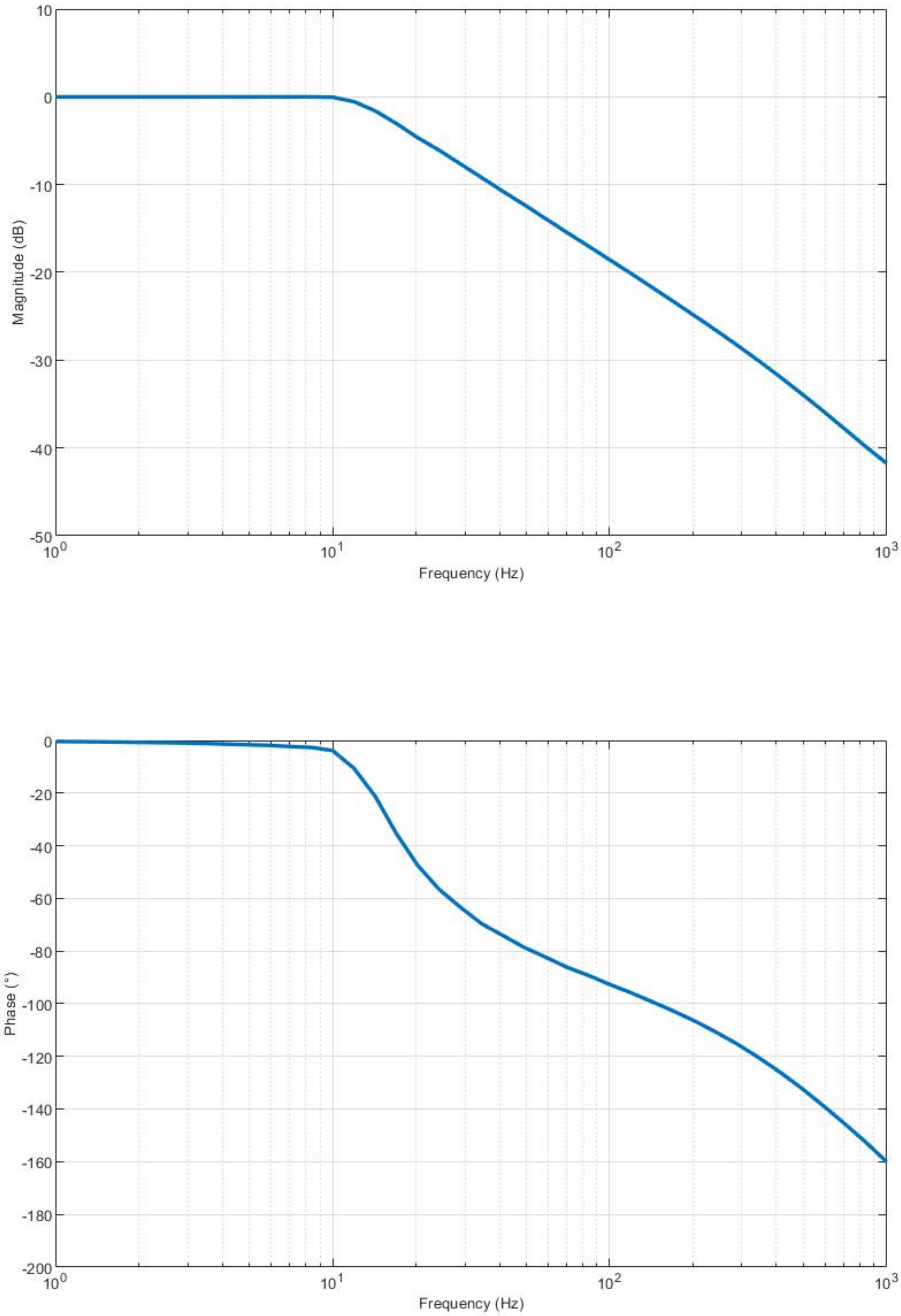

Figure 64: Frequency response closed-loop system at P_s:17MPa, T:20°C, V_SET:5V

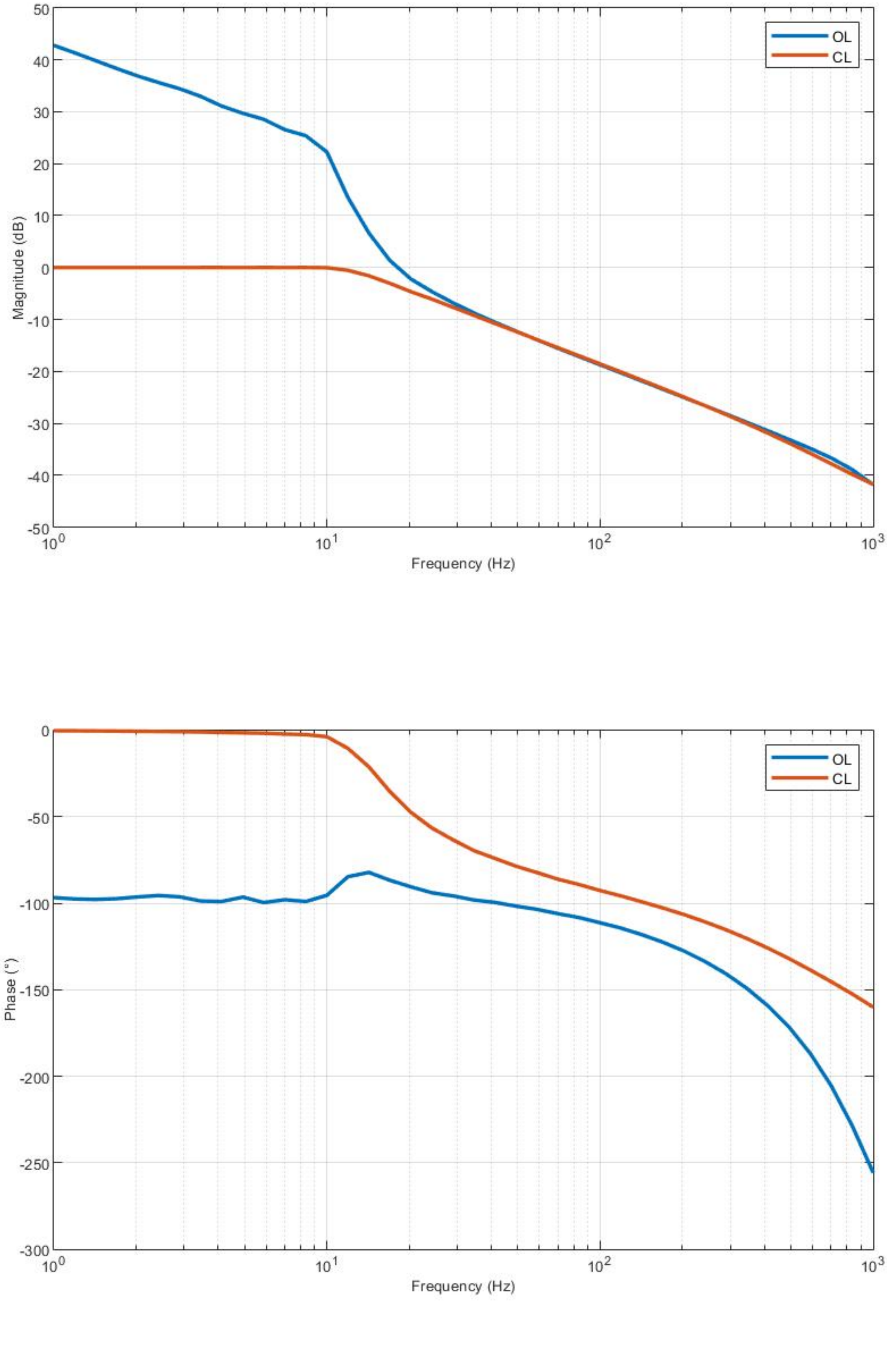

Figure 65: Frequency response closed and open loop system at P_s:17MPa, T:20°C, V_SET:5V

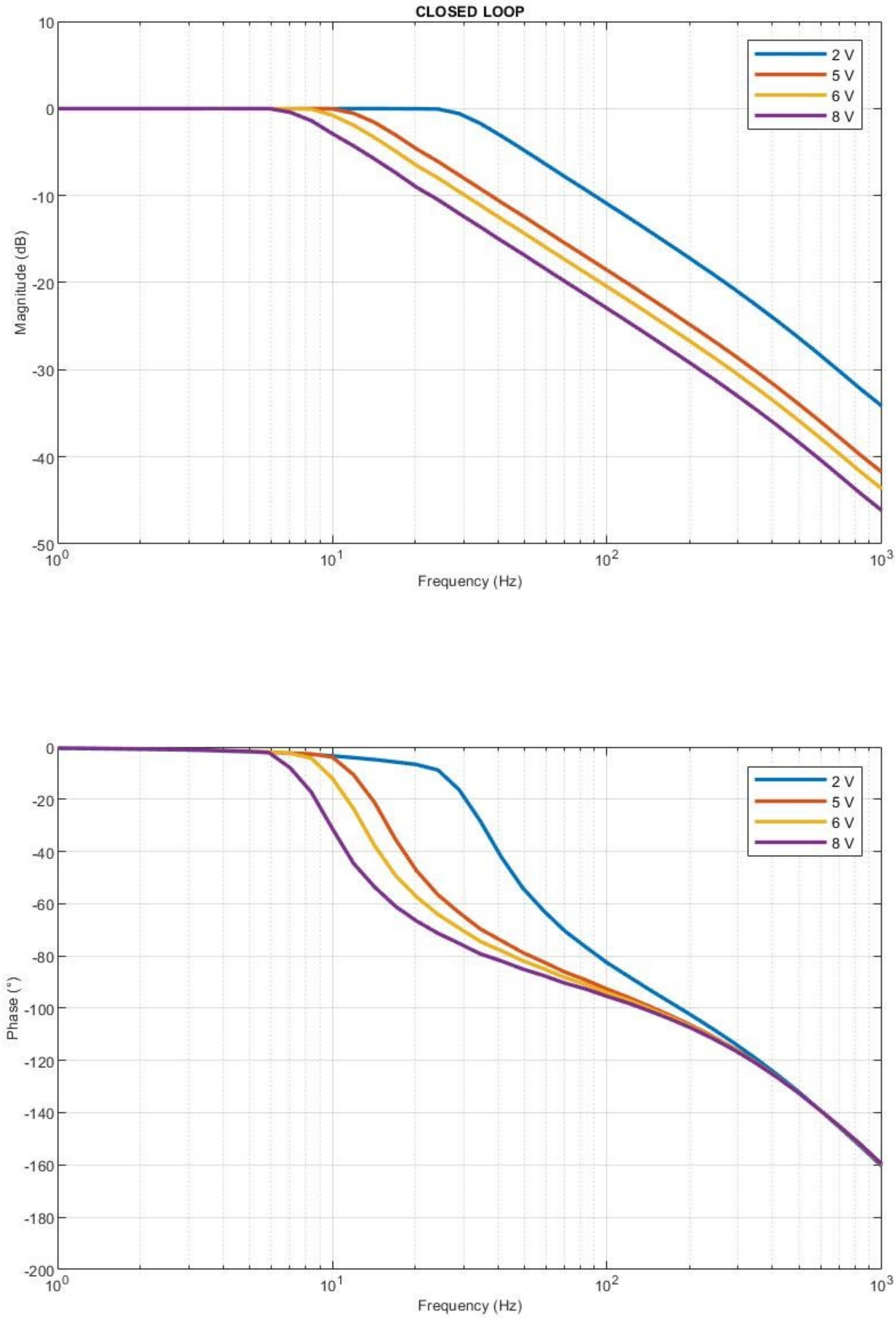

Figure 66: Frequency response closed-loop system at P_s:17MPa, T:20°C and different set voltages

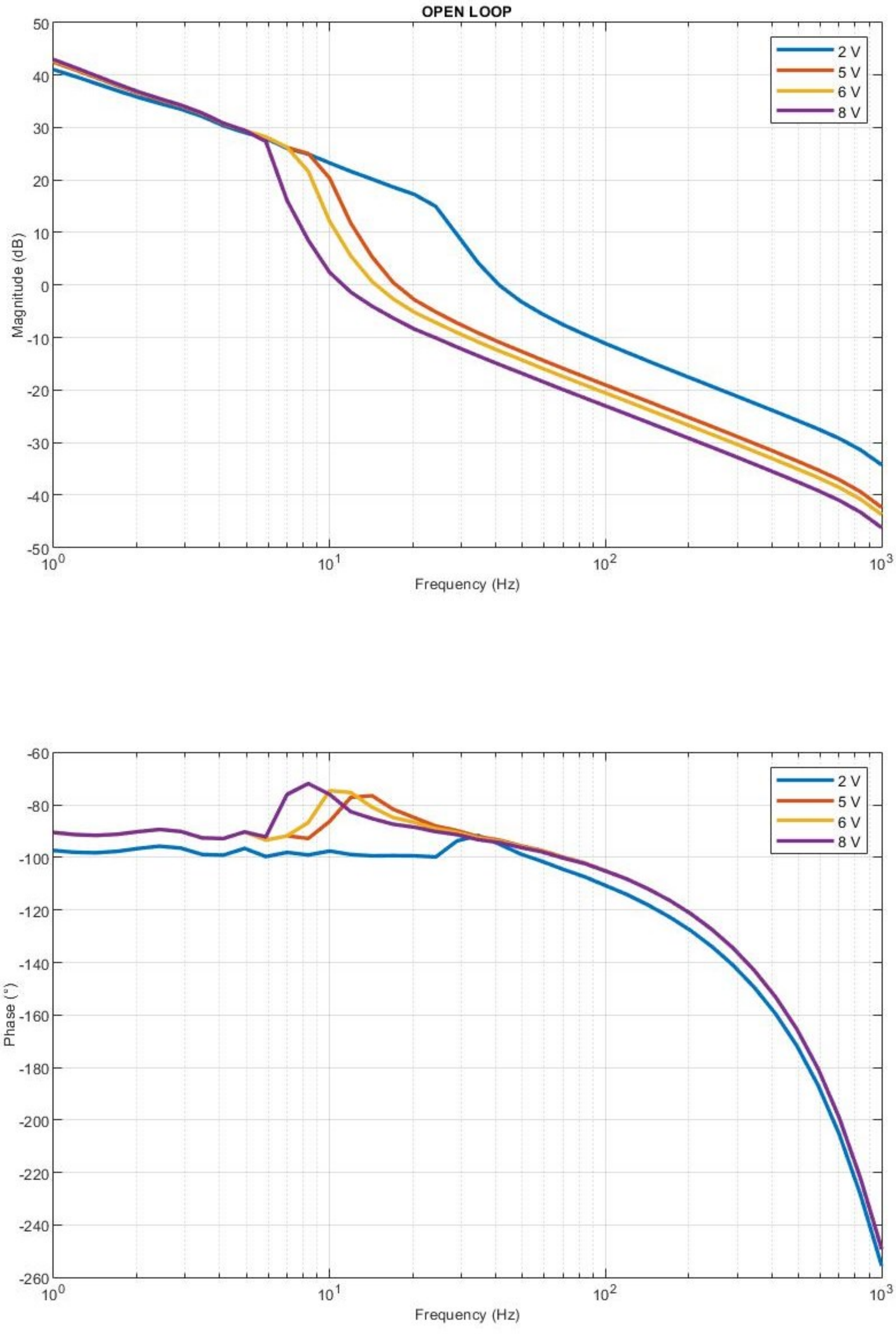

Figure 67: Frequency response open-loop system at P_s:17MPa, T:20°C and different set voltages

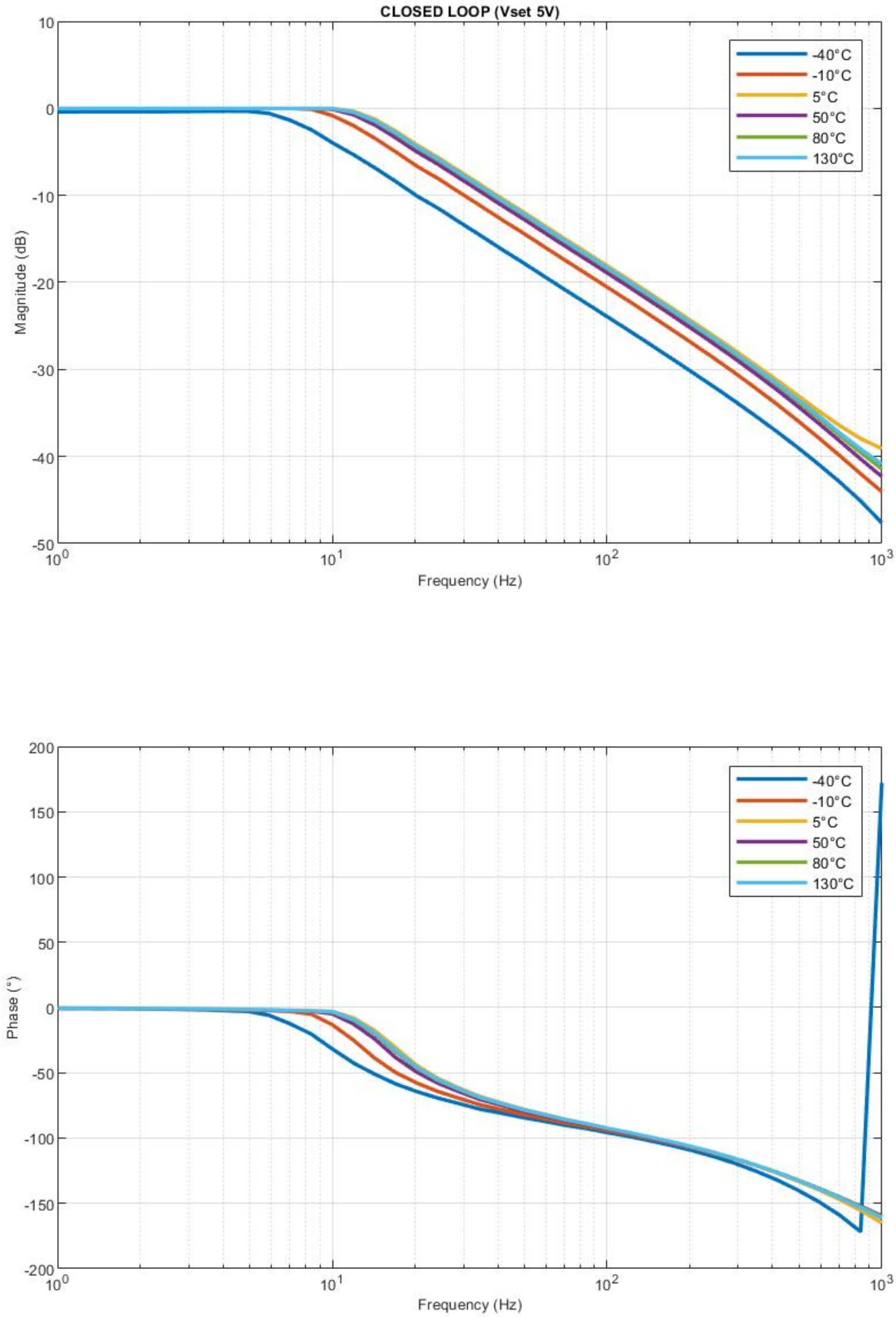

Figure 68: Frequency response closed-loop system at P_s:17MPa, V_set 5V and different Temperatures

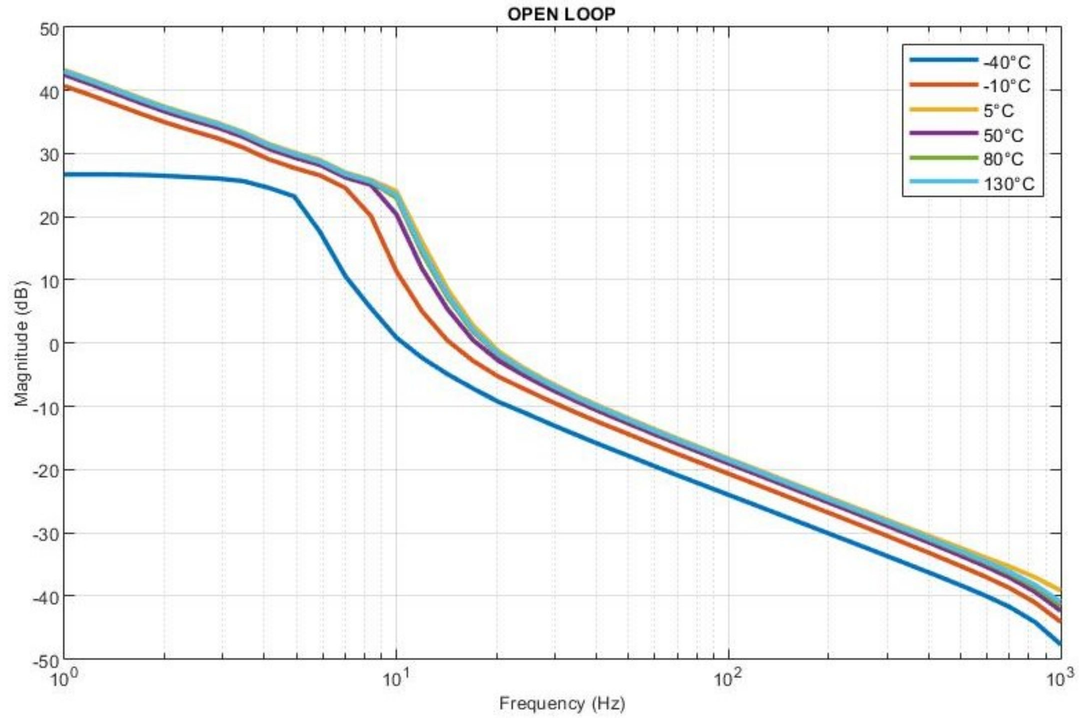

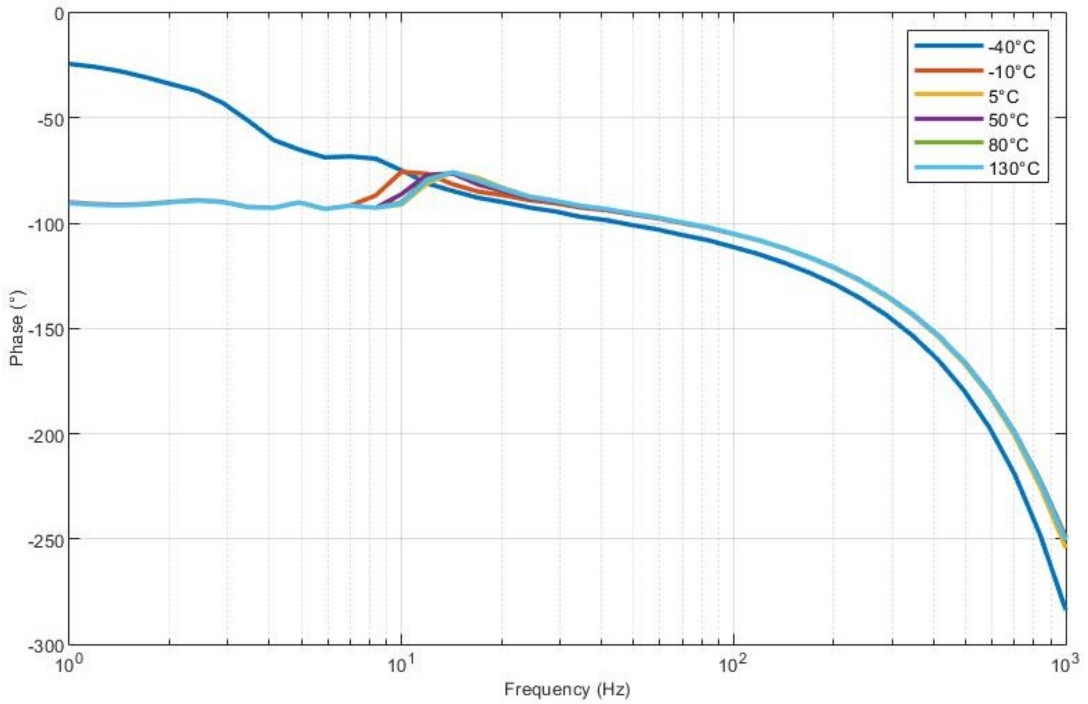

Figure 69: Frequency response open-loop system at P_s:17MPa, V_set 5V and different Temperatures

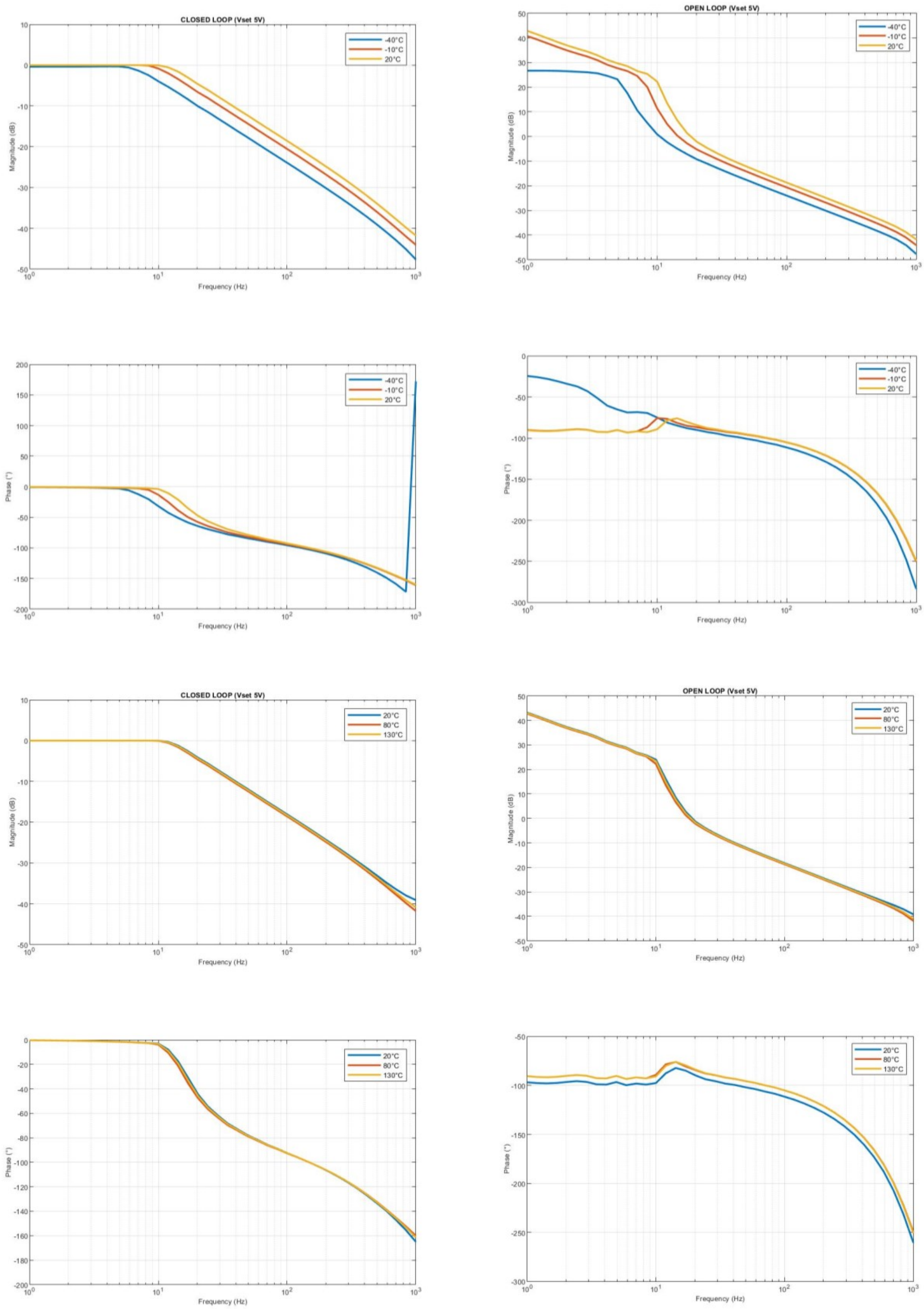

Figure 70: Bode diagrams of the system as temperatures decrease (top), and as temperatures increase (bottom). P_s:17MPa, V_set 5V

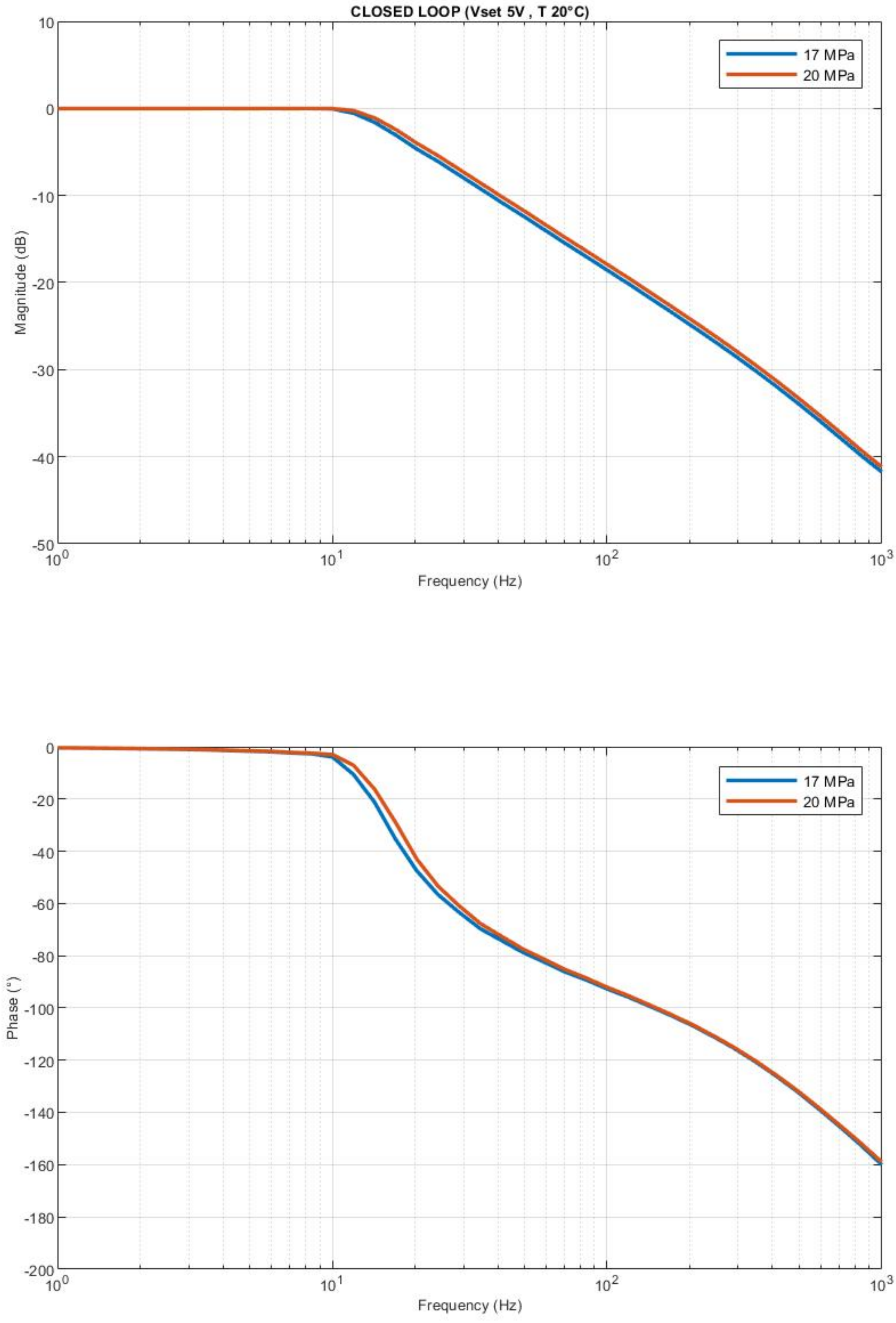

Figure 71: Bode diagram closed loop at T 20°C, V_set 5V and different Supply Pressure

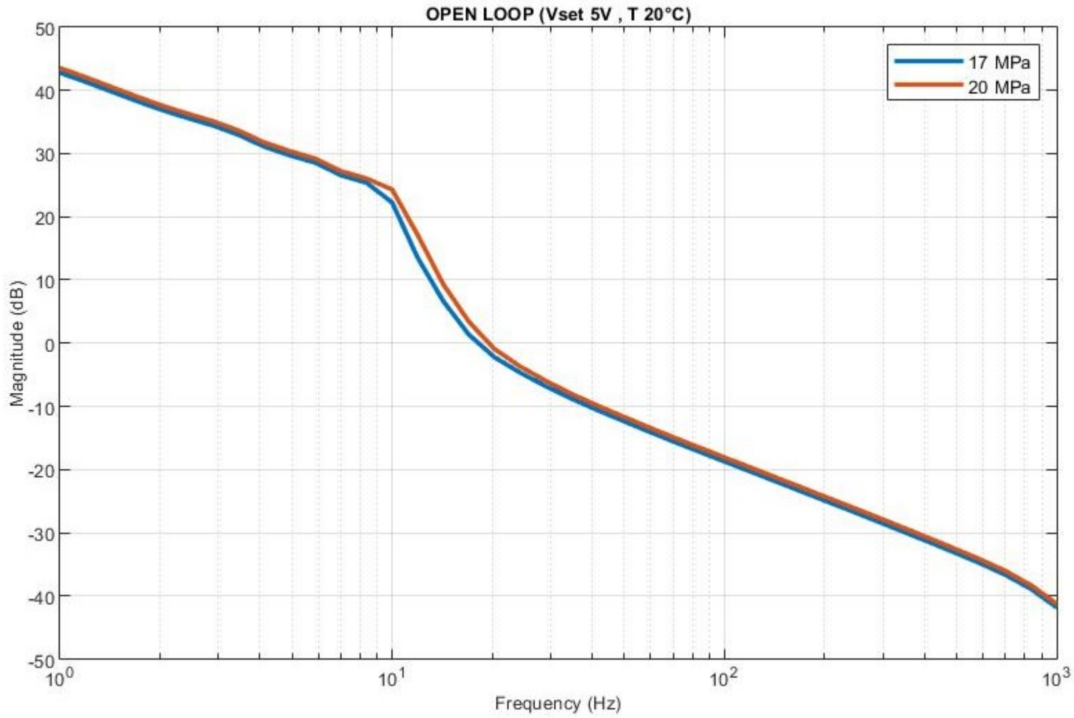

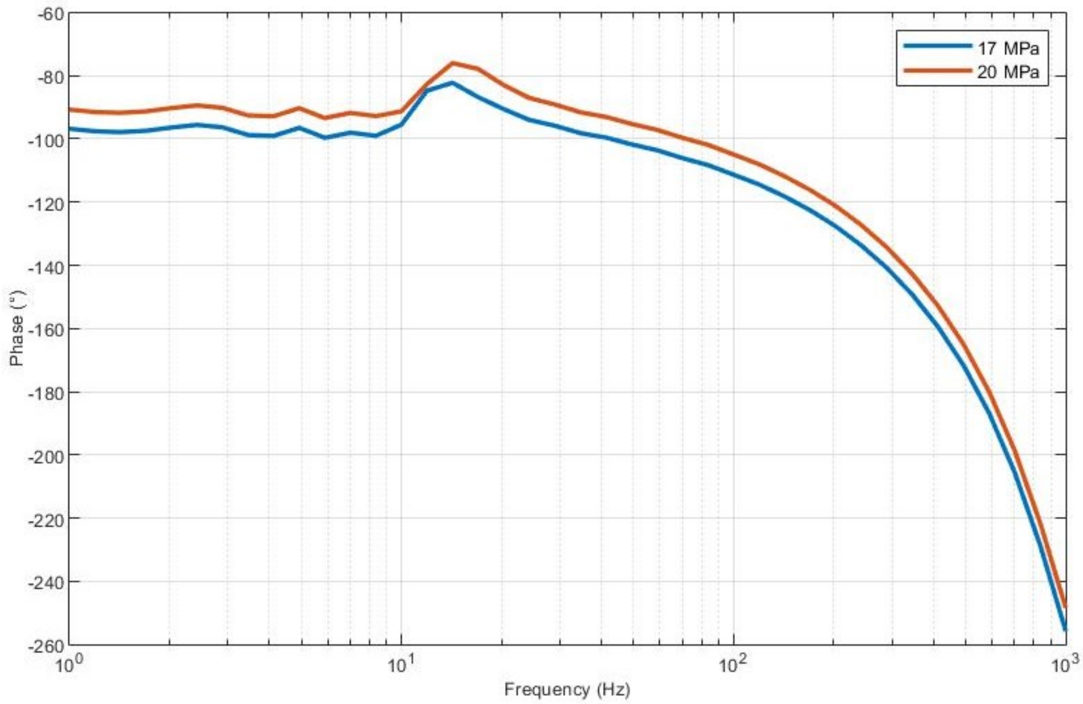

Figure 72: Bode diagram open loop at T 20°C, V_set 5V and different Supply Pressure

In general, it can be stated that the performance of the servo system is in line with what could be expected. The system is stable and robust. In figure 66 and 67, it can be seen that as the amplitude of the SET signal decreases, the bandwidth increases accordingly. Conversely, it can be seen that increasing the amplitude reduces the bandwidth and increases the stability margin. This is due to the fact that a model with non-linearities has been considered, in fact, in an ideal model would always obtain the same curve as the amplitude varies. In addition, the bandwidth increases with increasing temperature, as the properties of the hydraulic fluid change, thus affecting the performance of the system (fig. 68-69). This relationship described is particularly evident at low temperatures; at higher temperatures, the difference in system performance is not very significant (fig. 70). Finally, in Figures 71 and 72, the effect of supply pressure can be seen. As the supply pressure increase, the speed of movement of the SCAS actuator and its readiness increase. In accordance with this, it can be noted that the bandwidth increases as the pressure raise.

4. MODEL DATA AND MATLAB SCRIPT

In this chapter, the Matlab data script and some model data considerations will be presented. All numerical values used in the Simulink model can be found in the script.

4.1 Hydraulic Fluid Properties

As stated in chapter two, the input data required a choice between three different types of hydraulic fluid. For this thesis work, operational hydraulic fluid *MIL-PRF-83282* was chosen. This synthetic hydrocarbon base fluid is popular in military applications where it is very appreciated as a versatile fire-resistant hydraulic fluid, can also operate at low temperatures down to $-40°C$ [28][29]. The properties of the hydraulic fluid were calculated using a specific Matlab *function* "*MIL_PRF_83282*". This function has as input the temperature and operating pressure of the fluid, and give as output the density, viscosity, and bulk modulus. For the sake of exhaustiveness, the expressions used to determine the output quantities are shown:

- **Hydraulic Fluid Density**

  The density of a fluid is considered as a function of pressure and temperature

  $\rho = \rho(p, T) \Rightarrow \rho = \rho_0 + \left(\frac{\partial \rho}{\partial p}\right)_T (p - p_0) + \left(\frac{\partial \rho}{\partial T}\right)_p (T - T_0)$

  Where:

  ρ is the density.

  p is the pressure.

  T is the temperature.

  p_0 and T_0 are Standard Temperature and Pressure conditions (p_0: $10^6 Pa$ T: $0°C$)

  However, it can be shown that the contribution of pressure in determining density can be considered negligible. The density trend can be simplified as shown in the figure 73.

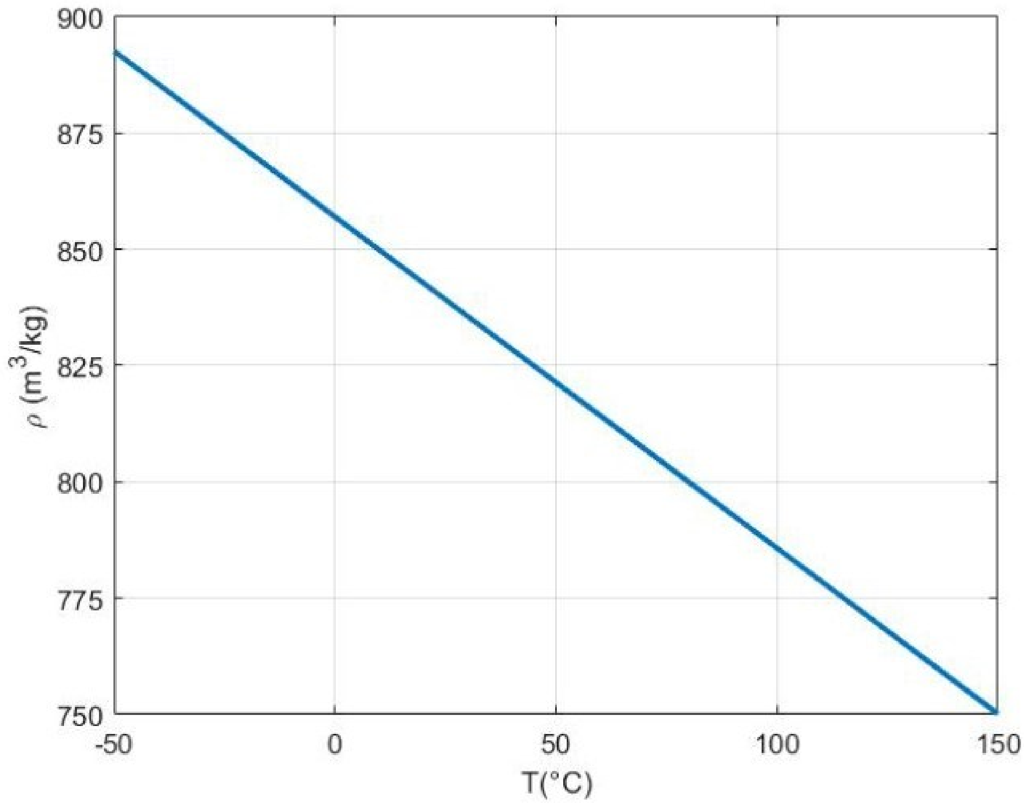

Figure 73: Density as a function of temperature

- **Hydraulic Fluid Viscosity**

Considering a fluid in unidirectional motion, dynamic viscosity is expressed by the following generic case formula:

$$\mu = \tau \frac{\partial y}{\partial u}$$

Where:

μ is the dynamic viscosity.

$u(y)$ is the fluid velocity.

τ is the shear stress.

Even in this case, it can be shown that viscosity is largely influenced by temperature. Figure 74 shows the relationship that exists between kinematic viscosity $\nu = \frac{\mu}{\rho}$ expressed on a logarithmic scale and the temperature.

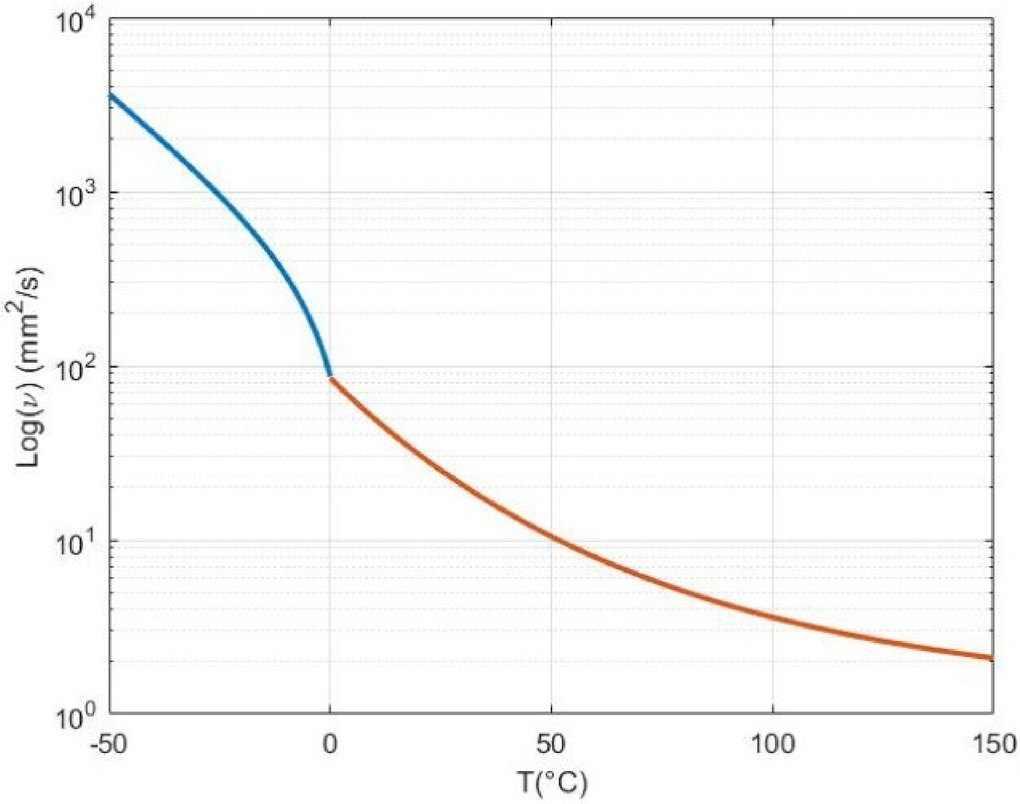

Figure 74: Kinematic viscosity as a function of temperature

- **Hydraulic Fluid Bulk Modulus**

  In addition to the formulation expressed for the Bulk module in chapter 2.4, another formulation is:

$$\beta_e = \frac{1}{\frac{1-f}{\beta_l} + \frac{f}{\beta_g}}$$

Where:

β_e is the effective Bulk modulus.

β_l is the Bulk modulus of a pure liquid.

β_g is the Bulk modulus of the gas.

$f = \frac{V_g}{V_l}$ is the volume fraction of gas in the liquid.

Finally, it can be stated that Bulk modulus is function of $\beta_e = \beta_e(f, p, T)$.

4.2 Matlab Data File

The following Matlab file contains the data values and all the necessary relations to complete the model, derived from the dimensioning operations.

```
% Data_modello_SCAS
% Thesis: Dynamic modelling of a compact EHSA for the
Stabilization and Command Augmentation System of rotary wing
aircraft
% Luciano Alberto Lo Presti s267978

clear all, close all
%% Main data
Ps_max = 20*1e6;     % [Pa] max supply pressure
Ps_min = 17*1e6;     % [Pa] min supply pressure
Pr_min = 0.3*1e6;    % [Pa] min return pressure
Pr_max = 0.7*1e6;    % [Pa] max return pressure

Ps=Ps_min;
Pr=Pr_min;
Pm=(Ps+Pr)/2;

T=20;                % Temperature in °C
[ro,mu,beta,beta_r,coeffd]=MIL_PRF_83282(T,(Ps_max+Ps_min)/2);

%% SCAS DATA
%% SolenoidValve Data
    A_va_max=2e-6;   % Passage area [m^2]
    V_va_max=10;     % Max Voltage SV [V]
    tau_va=35e-3;    % Electrical valve energisation delay
%% Servovalve Data
%Electrical circuit
    imax_sv=10e-3;       % Max current [A]
    k_amp=0.8;           % Electrical circuit gain

% Torque motor
    Rc_sv=5e4;           % Rated Coil resistance [Ohm]
    Rc2_sv=Rc_sv;        % Coil 1 resistance [Ohm]
    Rc1_sv=Rc_sv;        % Coil 2 resistance [Ohm]
    la_sv=54.5e-3;       % Distance between left and right pole [m]

    lp_sv=25e-3;         % Length of permanent magnet [m]
    Ap_sv=660e-6;        % Cross_sectional area of permanent magnet
[m2]
    Vp_sv=10.67e3;       % Magnetomotive force of permanent magnet
[A]
    Br_sv=0.28;          % Residual flux density of permanent
magnet [T]
```

```
    B0_sv=0.860;          % Normalizing flux density [T]
    mup_sv=1.1*4*pi/1e7;% Permeability of magnet [N/A2]
    mua_sv=4*pi/1e7;      % Permeability of air [N/A2]

    Ag_sv=0.01;           % Cross_sectional area of on air-gap [m2]
    l0_sv=2e-4;           % Normal value of the four air_gaps [m]

    H_sv=0;               % Air_gap height error [m]
    h_sv=H_sv/l0_sv;
    W_sv=0;               % Air_gap right and left imbalance [m]
    w_sv=W_sv/l0_sv;
    G_sv=0;               % Air_gap imbalance incline of armature
[m]
    g_sv=G_sv/l0_sv;
    gap_ms=0;             % gap between spring and spool

    n1_sv=3020;           % Number of coil turns
    n2_sv=3020;           % Number of coil turns


R_f=2*(lp_sv/(mup_sv*Ap_sv))+2*(la_sv/(mup_sv*Ap_sv));%Magnetic
reluctance ferromagnetic material [H-1]
    R_a=4*l0_sv/(mua_sv*Ag_sv);
%Magnetic air gap material reluctance [H-1]
    R_m=R_f+R_a;
%Equivalent magnetic reluctance [H-1]

    k_sv=mup_sv*Vp_sv/(2*B0_sv*l0_sv)-1;

T0_sv=la_sv*Ag_sv*Vp_sv^(2)*mua_sv/(4*(k_sv+1)^(2)*l0_sv^(2));%Out
put torque [Nm]

%Jet-pipe Armature
    Ja_sv=1.9575e-5;                 % Rotational mass of armature
[Nm/(m/s2)]
    bf_sv=0.56;                      % Damping on armature
[Nm/(m/s)]
    Kf_sv=7.073e4;                   % Stiffness of armature [Nm/m]
    xf_sv_max=0.000104;              % Max armature displacement
[m]
    xf_sv_max_sat=xf_sv_max*1.15;    % Max armature displacement
saturation [m]
%Hydraulic Circuit
    %Geometrical data
    Lt_pipe=(45+136+pi*20+163)/(5*1000);    %Hydraulic circuit
equivalent length [m]
    Dt_pipe=(6e-3)/5;                       %Hydraulic pipe
diameter [m]
    Area_idr=(Dt_pipe^(2)*pi)/4;            %Hydraulic pipe
section area [m^2]
```

```
    V_idr=Area_idr*Lt_pipe;          %Hydraulic pipe volume [m^3]
    %Hydraulic capacity
    C_idr_nocorrection=V_idr/(Ps-Pr);       %[m^4*s^2/kg]
    %Data for calculating hydraulic resistance
    n0_idr=0.04;
    alfa_idr=25;                    %pipe curve radius[deg]
    eps_pipe=0.1;                   %Roughness Ra:0.1
    delta_idr=pi;                   %Curvature angle [rad]
    r0_idr=0.02;                    %Curvature radius [m]
    gamma_idr=Dt_pipe/(2*r0_idr);
    d_jet_nozzle=1e-3;              %jet nozzle diameter [m]
    Area_jet_nozzle=(d_jet_nozzle^(2)*pi)/4;%jet nozzle area [m^2]

    d_return=2.4/1000;                      %Return pipe diameter
[m]
    Area_jet_ruturn=(d_return^(2)*pi)/4;    %Return pipe area
[m^2]

%Receiver and Hydraulic amplifer
    Gd_jet=1.25;                %Gain Projector Jet Nozzle
Diameter
    d_jet=2e-4*Gd_jet;          %Projector Jet Nozzle Diameter [m]
    d_r=0.279e-3;               %Receiver Holes Diameter [m]
    w_bv=d_r;                   %Pipe entrance windth [m]
    w=0.028e-3;                 %Receiver Bridge Length [m]
    o_bv=0;                     %Jet pipe inlet pipe length [m]
    e_jp=0.0001e-3;
    NSD_min=0.1524e-3;          %Jet-to Receiver Clearance min [m]
    NSD_max=0.2032e-3;          %Jet-to Receiver Clearance max [m]
    x_jet=(NSD_max+NSD_min)/2;  %Medium distance between jet and
orifice [m]
    h_bv=x_jet;                 %Pipe radial clearance [m]
    j_angle=22.5;               %Jet hole angle [deg]

    A_jet=(d_jet^(2)*pi)/4;     %Area Projector Jet Nozzle [m^2]
    A_r=(d_r^(2)*pi)/4;         %Area Receiver Holes [m^2]
    delta_r=0.95;               %Loss factor, hp:0.95

    r_r=d_r/2*1.5;              %Radius of receiver hole [m]
    r_jp=d_jet/2*1.3069*1.5;    %Radius of jet-pipe flow [m]

%Miscellaneous
    Cd_orifice=0.7;     % Discharge coefficient receiver holes
    C_dr=Cd_orifice;
    Cdj=0.91;           % Discharge coefficient jet nozzle
    C_eff=Cdj;
    Remax_sv=5000;      % Reynold max
%% Data SCAS actuator
%Geometrical data
    d_la=0.0045;                     % Rod diameter [m]
```

```
    d_lai=0.005;                    % Rod diameter internal[m]
    D_la=0.011;                     % Piston diameter [m]
    D_lai=0.015;                    % Housing internal diameter
[m]
    s_sc=(d_la-d_lai)/2;            % Rod wall thickness [m]
    s_sci=pi*(D_la-D_lai)/2;        % Cylinder wall thickness [m]
    AeMs=(D_la^2-d_la^2)*pi/4;      % Active area 1 [m^2]
    ArMs=(D_la^2-d_la^2)*pi/4;      % Active area 2 [m^2]
    L_la=0.00335;                   % Half cylinder stroke [m]
    LeM=L_la+0.05*L_la;             % Endstop stroke [m]
    L_rod=0.1;                      % Rod Length [m]
    L_bp=0.007;                     % Piston Length [m]
    A_rod=pi*(d_la^2-d_lai^2)/4;    % Rod cross section Area
[m^2]
    VeMs=AeMs*L_la*1.01;            % Volume chamber 1 [m^3]
    VrMs=VeMs;                      % Volume chamber 1 [m^3]
    Mrod_i=7850*(A_rod*L_rod);               % Mass rod [kg]
    MAct_i=7850*(((pi*D_la^(2))/4)*L_bp);    % Mass cyl [kg]
    Mrod=7850*(A_rod*L_rod)+0.5;             % Total Mass
rod,considering the attached loads [kg]
    MAct=7850*(((pi*D_la^(2))/4)*L_bp)+0.22; % Total Mass
cyl,considering the attached loads [kg]


%Endstop
   K_endstop=3e6;       % edstop stiffness [N/m]
   C_endstop=1e2;       % endstop damping [Ns/m]

%Centering spring
    delta0_la=1e-3;     % Precompression [m]
    Fc0_la=100;         % Cantering spring Preload [N], value that
cancels each other out in the balance of the actuator forces
    Kc_laS=1e4;         % Left spring stiffness [N/m]
    Kc_laD=Kc_laS;      % Right spring stiffness [N/m]

%Equilibrium condition
    x0_la=0;                             % Initial position piston
[m]
    Pmean=Pm;                            % Initial condition Medium
pressure [Pa]
    DP_eq=Pmean*(AeMs-ArMs)/(AeMs+ArMs);% Pressure difference
between the two chambers [Pa]
    P01=Pmean-DP_eq;                     % Chamber 1 pressure [Pa]
    P02=Pmean+DP_eq;                     % Chamber 2 pressure [pa]

% Friction
    run ('Data_seal_SCAS')
    KfricT1=ones(3,3);
    KfricT2=ones(3,3);
```

```
    FfricStExt=FH_sc;        %FH = Total friction due to hydraulic
pressure
    FfricStRet=FfricStExt;
    FricdB=1e-5;             %[N]
    kstdi=0.2;               % Ratio of static to dynamic
    kFrRod=0.8;
    Gamma=1e-4;              % Coefficient of viscous friction
[Ns/m]
    thpress=100000;          % Pressurized system threshold [Pa]
% Leakage coefficient
    KlMs=zeros(3,3);
    Kli1_SC=7.9*1e-14;   % Internal [m3/(sPa^0.5)]
    Kli2_SC=7.9*1e-14;   % Internal [m3/(sPa^0.5)]

%% External Load Dyn
    m_ld=0.5;        % translating mass of external load [kg]
    c_ld=1e-5;       % approximate dumping factor [Ns/m]
    E_ld=2.1e11;     % Young modulus [N/m^2]
    D_ld=0.02;       % External load lever diameter [m]
    r_ld=D_ld/2;     % External load radius [m]
    I_ld=(m_ld*(r_ld^2))/2; % External load inertia [Kg m^2]
    l_ld=0.5;                % External load lever length [m]
    k_ld=1e3;                % approximate lever stiffness [N/m]

%% Rod and Cylinder parameters

    krod=1e3;    %rod stiffness [Nm]
    crod=1e-4;   %damping of the rod [Ns/m]
    ksa=krod;
    csa=crod;

    FfricStExt_ld=FfricStExt-10;
    FfricStRet_ld=FfricStRet-10;

%% LVDT
%LVDT Demodulation filter
    Vfb_max=10;          % V_fb=+-10V
    f_fb=500;            % Filter natural frequency [Hz]
    w_fb=2*pi*f_fb;      % Filter natural frequency [rad/s]
    z_fb=0.5;            % Filter damping
    Glv_fb=Vfb_max/L_la;% DC Gain LVDT [(V/V)/m]

%% PI Controller
    Vrif_max=10;     % Maximum controller voltage [V]
    Ka=32.474;       % Proportional gain
    Ki=1.27;         % Integrative gain

%% Miscellaneous
 NullBias=0;
 Dsv_on=1;
```

```
 seed_svST1=mod(3*ceil(prod(clock)),2^31);
 seed_svST2=mod(4*ceil(prod(clock)),2^31);

%% Input
 tend=1;            % Simulation time [s]
 SCAS2_SWITCH=1;    % 1=SCAS ON 0=SCAS OFF
```

4.2.1 Frequency Response Script

The script used to perform the frequency response is now presented. The main purpose of this appendix is to provide via Matlab data sheet all those simulation data that have been omitted previously. For example, it might be useful to note the range of frequencies tested and the sampling number.

```
%% Frequency_response
% Thesis: Dynamic modelling of a compact EHSA for the
Stabilization and Command Augmentation System of rotary wing
aircraft
% Luciano Alberto Lo Presti s267978

run('Data_modello_SCAS.m');

pin_loop=Ps;            %Tested supply pressure [Pa]
Tup_loop = [-40 20 80];     %Tested Temperature [°C]


%% set FR parameters
ampl_vec=[2 6 8];    %Voltage amplitude to be tested [V]
bias=0;              %Mean value amplitude sinusoidal command
itime=1;             %Minimum simulation time [s]
frmin=1;             %Minimum frequency [Hz]
frmax=1000;          %Maximum frequency [Hz]
npunti=40;           %number of samples frequency response
grat=0;
graf=1;
skip_time = 0.2;     %Skip time [s]

%% Start analysis

nomemod='Modello_SCAS.slx';      %Simulink model name
nomesig.OL_in = "err [V]";       %IN OL signal name
nomesig.OL_out = "V_F/B [V]";    %OUT OL signal name
nomesig.CL_in = "Vset [V]";      %IN CL signal name
nomesig.CL_out = "x_volt [V]";   %OUT CL signal name
```

```
for g = 1:max(size(ampl_vec))
    ampl = ampl_vec(g);
    for i = 1:max(size(pin_loop))
        for j = 1:max(size(Tup_loop))
            SELECT_set = 2;
            pin(:,1)=linspace(0,20,20);
            pin(:,2)=pin_loop(i);
            T=Tup_loop(j);

[ro,mu,beta,beta_r,coeffd]=MIL_PRF_83282(T,(Ps_max+Ps_min)/2); %To
be commented on the data sheet

[OL,CL,w]=rf_ana([ampl bias itime frmin frmax npunti grat graf],
nomesig,nomemod,skip_time);

save(['Pin',num2str(pin_loop(i)./1E5),'V',num2str(ampl),'T',num2st
r(Tup_loop),'.mat'],'OL','CL','w')


        end
    end
end
```

5. CONCLUSIONS

In this thesis work, a Dynamic modelling of a compact EHSA for the Stabilization and Command Augmentation System of rotary wing aircraft was performed. The main objective was therefore to investigate the functionality and performance of a compact SCAS system, or in other words without the second stage of a servo-valve. A model was made, using the necessary illustrated mathematical relations and Simulink software, of the first stage of a jet-pipe servo-valve. In particular, were investigated and modelled: the electrical and magnetic circuit, the torque motor behaviour, the dynamic response of the jet-pipe and the hydraulic circuit. In the same way, a SCAS actuator was modelled and dimensioned, through several tests. Finally, a LVDT position transducer and a PI controller were incorporated into the system. Subsequently, many tests were performed to evaluate the time response and frequency response of the system. As further investigation and to assess the goodness of the model, tests were carried out on the operating current, the dynamics and thus the jet-pipe stroke, and the flow rate using a characteristic curve given as input data. These tests were successful, and the results are compliant with the given targets. In response to the time domain, the system appears to be consistent in both the values and the trends of the main quantities, also considering what is found in the literature. When analysing the frequency response, it was observed that the bandwidth increases as the set amplitude decreases, the system temperature increases, with the raise of the supply pressure. In general, it can be stated that the performances achieved by this model are acceptable. Further work can be suggested to take the analysis forward. The approximation of the cylinder supports, that are considered with an infinite stiffness, made in modelling the SCAS actuator and could be eliminated through a dimensioning work. For a better representation of real working conditions, the system should be embedded within a larger model simulating MRA, thus eliminating the approximation used to simulate the external load. Finally, a fine tuning of PI controller parameter will improve the system behaviour.

BIBLIOGRAPHY

[1] FAA-H-8083-21B *Helicopter Flying Handbook*. U.S. Department Of Transportation, Federal Aviation Administration, Washington, D.C., U.S.A, 2019.

[2] W. Johnson, *Rotorcraft Aeromechanics*. New York: Cambridge University Press, 2013.

[3] Andrea De Martin, Giovanni Jacazio, Massimo Sorli, and Giuseppe Vitrani. *A simulation survey on the effects of progressing faults within the scas of a light control actuator for helicopters.* Proceedings of the ASME /BATH 2021-Symposium on Fluid Power and Motion Control-FPMC 2021, ASME (accepted for publication), October 19-21, 2021.

[4] Giuseppe Vitrani, *Preliminary study towards the definition of a PHM framework for the SCAS system of primary flight control systems for helicopters*, Rel. Massimo Sorli, Andrea De Martin. Politecnico di Torino, Corso di laurea magistrale in Ingegneria Meccanica, 2021

[5] Donald McLean, *Automatic flight control systems*, Prentice Hall international series in systems and control engineering, Prentice Hall, New York, 1990.

[6] R. E Kalman. *A new approach to linear filtering and prediction problems*, Journal of fluids engineering, 82:35-45, 1960.

[7] Andrea Nesci, Andrea De Martin, Giovanni Jacazio, and Massimo Sorli. *Detection and prognosis of propagating faults in flight control actuators for helicopters.* Aerospace,7(3):20, 2020.

[8] Antonio Carlo Bertolino, Andrea Nesci, Andrea De Martin, Massimo Sorli, *Meccatronica – Analisi, progettazione a modellazione di servosistemi.* Edizioni C.L.U.T., Torino, 2021.

[9] Rydberg, K. E. *Hydraulic servo systems*. TMHP51 Fluid and Mechanical Engineering Systems, Linköping University, 2008.

[10] https://boschrexroth-ind.com/product/bosch-rexorth-directional-servo-valve-4ws2em6-2x-5b11xnet315k17ev-102-r901009654/ [accessed February 22, 2023]

[11] S H Somashekhar, M Singaperumal, and R Krishna Kumar. *Modelling the steady-state analysis of a jet pipe electrohydraulic servo valve.* Department of Mechanical Engineering, Indian Institute of Technology Madras, Chennai, India, 2005.

[12] Andrea Nesci. *Modello completo di sistema di comandi di volo per elicotteri e relativa analisi su fault detection.* Rel. Massimo Sorli. Politecnico di Torino, Corso di laurea magistrale in Ingegneria Meccanica, 2019.

[13] E Urata. *On the torque generated in a servo valve torque motor using permanent magnets*. Proceedings of the Institution of Mechanical Engineers, Part C: Journal of Mechanical Engineering Science, 221(5):519-525, 2007.

[14] E Urata. *On the torque generated in a servo valve torque motor using permanent magnets*. Proceedings of the Institution of Mechanical Engineers, Part C: Journal of Mechanical Engineering Science, 221(11):1287-1297, 2007.

[15] E Urata and K Suzuki. *Stiffness of the elastic system in a servo-valve torque motor.* Proceedings of the Institution of Mechanical Engineers, Part C: Journal of Mechanical Engineering Science, 225(8):1963{1972, 2011.

[16] I. E. IDELCHIK. *HANDBOOK OF HYDRAULIC RESISTANCE.* Central Aero-Hydrodynamics Institute (TsAGI), 4TH REVISED AND AUGMENTED EDITION, Moskow, 2007.

[17] Li Yuesong. *Mathematical modelling and characteristics of the pilot valve applied to a jet-pipe/deflector-jet servovalve.* Sensors and Actuators A: Physical, Volume 245, Pages 150-159, ISSN 0924-4247, 2016.

[18] Ying Zhang, Yunxia Xia. *Analysis and optimization of the pilot stage of jet pipe servo valve.* Alexandria Engineering Journal, Volume 61, Issue 1, Pages 41-50, ISSN 1110-0168, 2022.

[19] Somashekhar SH, Singaperumal M, Kumar RK. *Modelling the steady-state analysis of a jet pipe electrohydraulic servo valve.* Proceedings of the Institution of Mechanical Engineers, Part I: Journal of Systems and Control Engineering. 220(2):109-129. 2006; doi:10.1243/095965106X78211.

[20] Li Yuesong. *Mathematical modeling and linearized analysis of the jet-pipe hydraulic amplifier applied to a servovalve*. Proceedings of the Institution of Mechanical Engineers, Part G: Journal of Aerospace Engineering. 233(2):657-666. 2019; doi:10.1177/0954410017740386

[21] Lu, Xiaobin, M. M. Khonsari, and E. R. M. Gelinck. "*The Stribeck Curve: Experimental Results and Theoretical Prediction*." Journal of tribology 128.4 (2006): 789–794. Web.

[22] https://www.parker.com/literature/O-Ring%20Division%20Literature/Static%20Files/frictionestimation.pdf [accessed March 07, 2023]

[23] Li, J W et al. "*Friction Models Incorporating Thermal Effects in Highly Precision Actuators*." Review of scientific instruments 80.4 (2009): 045104–045104–6. Web.

[24] Davis, Kurt L, Austin D Fleming, Malwina A Wilding, Zhangxian Deng, Alex Draper, and Joshua Poorbaugh. *Status of Research Activities on LVDTs: Modeling and Simulation Development and Performance Characterization of Commercial LVDTs*. United States, 2022.

[25] https://passive-components.eu/linear-variable-differential-transformers-lvdts-explained/ [accessed March 08, 2023]

[26] Ziegler John G., Nichols Nathaniel B. *Optimum Settings for Automatic Controllers*. Committee on Industrial Instruments and Regulators of the Process Industries Division, The American Society Of Mechanical Engineers, New York, N. Y., U.S.A, 1941.

[27] Viktorov, Vladimir, and Federico Colombo. *Automazione dei sistemi meccanici: corso di base*. 3a ed. Torino: CLUT, 2013.

[28] Rapson, R L, C E Snyder, L J Gschwender, S K Sharma, and A Fletcher. *Military Aerospace Hydraulic Fluids Workshop Proceedings,* 2006.

[29] Military and Government Specs & Standards. *HYDRAULIC FLUID, FIRE RESISTANT, SYNTHETIC HYDROCARBON BASE, METRIC, NATO CODE NUMBER H-537*, *MIL-PRF-83282*, Revision D, September 30, 1997. Published: July 2019